Calhoun: The NPS Institutional Archive

DSpace Repository

Theses and Dissertations | 1. Thesis and Dissertation Collection, all items

2021-06

VERIFICATION OF ADDITIVE MANUFACTURED PRESSURE DROP COMPONENTS

Manjai, Thanakrit

Monterey, CA; Naval Postgraduate School

https://hdl.handle.net/10945/67769

This publication is a work of the U.S. Government as defined in Title 17, United States Code, Section 101. Copyright protection is not available for this work in the United States.

Downloaded from NPS Archive: Calhoun

http://www.nps.edu/library

Calhoun is the Naval Postgraduate School's public access digital repository for research materials and institutional publications created by the NPS community. Calhoun is named for Professor of Mathematics Guy K. Calhoun, NPS's first appointed -- and published -- scholarly author.

Dudley Knox Library / Naval Postgraduate School
411 Dyer Road / 1 University Circle
Monterey, California USA 93943

NAVAL POSTGRADUATE SCHOOL

MONTEREY, CALIFORNIA

THESIS

VERIFICATION OF ADDITIVE MANUFACTURED PRESSURE DROP COMPONENTS

by

Thanakrit Manjai

June 2021

Thesis Advisor:	Walter Smith
Co-Advisor:	Garth V. Hobson
Second Reader:	Anthony J. Gannon

Approved for public release. Distribution is unlimited.

THIS PAGE INTENTIONALLY LEFT BLANK

REPORT DOCUMENTATION PAGE			Form Approved OMB No. 0704-0188

Public reporting burden for this collection of information is estimated to average 1 hour per response, including the time for reviewing instruction, searching existing data sources, gathering and maintaining the data needed, and completing and reviewing the collection of information. Send comments regarding this burden estimate or any other aspect of this collection of information, including suggestions for reducing this burden, to Washington headquarters Services, Directorate for Information Operations and Reports, 1215 Jefferson Davis Highway, Suite 1204, Arlington, VA 22202-4302, and to the Office of Management and Budget, Paperwork Reduction Project (0704-0188) Washington, DC 20503.

1. AGENCY USE ONLY *(Leave blank)*	2. REPORT DATE June 2021	3. REPORT TYPE AND DATES COVERED Master's thesis

4. TITLE AND SUBTITLE VERIFICATION OF ADDITIVE MANUFACTURED PRESSURE DROP COMPONENTS	5. FUNDING NUMBERS
6. AUTHOR(S) Thanakrit Manjai	
7. PERFORMING ORGANIZATION NAME(S) AND ADDRESS(ES) Naval Postgraduate School Monterey, CA 93943-5000	8. PERFORMING ORGANIZATION REPORT NUMBER
9. SPONSORING / MONITORING AGENCY NAME(S) AND ADDRESS(ES) N/A	10. SPONSORING / MONITORING AGENCY REPORT NUMBER

11. SUPPLEMENTARY NOTES The views expressed in this thesis are those of the author and do not reflect the official policy or position of the Department of Defense or the U.S. Government.

12a. DISTRIBUTION / AVAILABILITY STATEMENT Approved for public release. Distribution is unlimited.	12b. DISTRIBUTION CODE A

13. ABSTRACT (maximum 200 words)

This research was conducted to verify the use of additive manufacturing in producing pressure drop components inside fluid loops. A design was studied through Computation Fluid Dynamics modeling and produced using different additive manufacturing methods. A scaled loop was also designed to measure the performance and viability of the components. One component, the Packed Bed, proved to be a viable replacement using computational methods. The other component, the Helical, requires design modifications to mitigate pulsing behavior to be a viable replacement.

14. SUBJECT TERMS pressure drop components, additive manufacturing, velocity profile	15. NUMBER OF PAGES 141
	16. PRICE CODE

17. SECURITY CLASSIFICATION OF REPORT	18. SECURITY CLASSIFICATION OF THIS PAGE	19. SECURITY CLASSIFICATION OF ABSTRACT	20. LIMITATION OF ABSTRACT
Unclassified	Unclassified	Unclassified	UU

NSN 7540-01-280-5500

Standard Form 298 (Rev. 2-89)
Prescribed by ANSI Std. 239-18

THIS PAGE INTENTIONALLY LEFT BLANK

Approved for public release. Distribution is unlimited.

VERIFICATION OF ADDITIVE MANUFACTURED PRESSURE DROP COMPONENTS

Thanakrit Manjai
Ensign, United States Navy
BS, United States Naval Academy, 2020

Submitted in partial fulfillment of the
requirements for the degree of

MASTER OF SCIENCE IN MECHANICAL ENGINEERING

from the

NAVAL POSTGRADUATE SCHOOL
June 2021

Approved by: Walter Smith
Advisor

Garth V. Hobson
Co-Advisor

Anthony J. Gannon
Second Reader

Garth V. Hobson
Chair, Department of Mechanical and Aerospace Engineering

THIS PAGE INTENTIONALLY LEFT BLANK

ABSTRACT

This research was conducted to verify the use of additive manufacturing in producing pressure drop components inside fluid loops. A design was studied through Computation Fluid Dynamics modeling and produced using different additive manufacturing methods. A scaled loop was also designed to measure the performance and viability of the components. One component, the Packed Bed, proved to be a viable replacement using computational methods. The other component, the Helical, requires design modifications to mitigate pulsing behavior to be a viable replacement.

THIS PAGE INTENTIONALLY LEFT BLANK

TABLE OF CONTENTS

I. INTRODUCTION....1
A. BACKGROUND....1
B. MOTIVATION....4
C. OUTLINE....5

II. DESIGNS....7
A. BACKGROUND....7
B. PEBBLE BED....7
1. Model Details....7
2. Analytical....8
3. Production....10
C. HELICAL CHANNELS....21
1. Model Details....22
2. Analytical....22
3. Production....23

III. EQUIPMENT....27
A. A-M PRODUCTION MACHINES....27
1. Xerox Elem-X Aluminum 3-D Printer....27
2. Ultimaker 3 3-D Printer....27
B. TEST LOOP FACILITY AND COMPONENTS....28
1. Loop Design....28
2. Pump....30
3. Variable Frequency Drive....31
4. Flow Monitoring Devices....31
5. Equipment Scaling....34

IV. RESULTS....37
A. COMPUTATIONAL....37
1. Packed Bed....37
2. Helical....44

V. CONCLUSION AND FUTURE WORK....49
A. CONCLUSION....49
B. FUTURE WORK....49
1. Complete Test Loop....49
2. Model Refinement....49

3. PIV....50

APPENDIX A. PACKED BED MODEL CALCULATIONS....51

APPENDIX B. PACKED BED INITIAL CFD CALCULATIONS....53

APPENDIX C. CFX PROCESS....55

APPENDIX D. PACKED BED MODEL CFX RESULTS....63

APPENDIX E. HELICAL MODEL CALCULATIONS....69

APPENDIX F. HELICAL MODEL CFX DATA....71

APPENDIX G. ELEM-X PRINT SCANS....75

APPENDIX H. MATLAB SCRIPT FOR IMAGE COMPILATION....107

APPENDIX I. VENTURI CALCULATIONS....109

APPENDIX J. LOOP PRESSURE RATINGS....111

APPENDIX K. CFD NUMERIC RESULTS....113

APPENDIX L. PRODUCTION DIMENSIONS AND BUILD TIMES....115

LIST OF REFERENCES....117

INITIAL DISTRIBUTION LIST....119

LIST OF FIGURES

Figure 1. Example of Pressure Loss Device....2

Figure 2. Cross Section of a Pressure Loss Device. 3

Figure 3. 2-D Packed Bed Flow. Source: Casey [9] 8

Figure 4. Packed Bed Model 9

Figure 5. Packed Bed Cross Section 10

Figure 6. SolidWorks .STL Creation....11

Figure 7. Meshmixer Make Solid Function....12

Figure 8. Make Solid Function Refinement. 13

Figure 9. Post Mesh Mixer Packed Bed Model....14

Figure 10. Packed Bed Model Printed....14

Figure 11. Narrower Exit Channels for Packed Bed Model....15

Figure 12. Second Packed Bed Print 16

Figure 13. Outlet Openings 17

Figure 14. Packed Bed Base Scan – Layer 5....18

Figure 15. Packed Bed Junction Growth – Layer 225 18

Figure 16. Packed Bed Junction– Layer 230....19

Figure 17. 3-D Packed Bed Scan Top View 20

Figure 18. 3-D Packed Bed Scan Side View....21

Figure 19. Helical Model Cross Section 22

Figure 20. Failed Print Cross Section with Support. 24

Figure 21. Helical Model....24

Figure 22. Helical Model Top View. 25

Figure 23. Xerox Elem-X Printer 27

Figure 24. Ultimaker 3 Printer. 28
Figure 25. Test Loop Schematic Diagram....29
Figure 26. Initial Testing Loop Construction. 30
Figure 27. McMASTER-Carr Part 8249K82. 31
Figure 28. Fuji Electric – FRN0010C2S-2U. 31
Figure 29. Elem-X Printed Venturi 33
Figure 30. CDAW 9181. 33
Figure 31. Omega PX273. 34
Figure 32. UNIMOUNT 125 ID B530 Pump. 35
Figure 33. Ac Tech M32250B VFD. 35
Figure 34. Whole Body Packed Bed. 37
Figure 35. Unit Cell Packed Bed. 38
Figure 36. Generating Initial Mesh. 39
Figure 37. Resolved Mesh. 42
Figure 38. Resolved Mesh Y+ 42
Figure 39. Pressure Gradient 43
Figure 40. Overall Packed Bed Pressure Loss 44
Figure 41. Overall Packed Bed Turbulence Kinetic Energy 44
Figure 42. Helical Model Pressure Gradient 45
Figure 43. Helical Model Turbulence Kinetic Energy 46
Figure 44. Pulsing Flow Residuals. 47
Figure 45. PIV Operation 50
Figure C1. ANSYS CFX Main Menu with Geometry Selection. 55
Figure C2. Initial Inflation Layer Selection. 56
Figure C3. Named Selection – Inlet. 56

Figure C4. Named Selection - Wall. 57
Figure C5. Named Selection - Symmetry. 57
Figure C6. Default Domain Selection. 58
Figure C7. Fluid Models Selection. 58
Figure C8. Inlet Conditions 59
Figure C9. Outlet Conditions. 59
Figure C10. Wall Conditions. 60
Figure C11. Solver Control Parameters. 60
Figure C12. Monitor Point Designation. 61
Figure C13. Solver Initialization Conditions. 61
Figure C14. Resolved Inflation Layer Settings 62
Figure D1. Unit-Cell Mass and Momentum Convergence. 63
Figure D2. Unit-Cell Turbulence Convergence. 64
Figure D3. Unit-Cell Monitor Points. Red indicates ΔP in psi and green indicates Cv. 65
Figure D4. Whole Body Mass and Momentum Convergence. 66
Figure D5. Whole Body Turbulence Convergence. 67
Figure D6. Whole Body Monitor Points of ΔP in kPa. 68
Figure F1. Mass and Momentum Convergence 71
Figure F2. Turbulence Convergence. 72
Figure F3. Monitor Points. 73
Figure G1. Initial Layer. 75
Figure G2. Layer 5. 76
Figure G3. Layer 10. 76
Figure G4. Layer 15. 77

Figure G5. Layer 20. 77
Figure G6. Layer 25. 78
Figure G7. Layer 30. 78
Figure G8. Layer 35. 79
Figure G9. Layer 40. 79
Figure G10. Layer 45. 80
Figure G11. Layer 50. 80
Figure G12. Layer 55. 81
Figure G13. Layer 60. 81
Figure G14. Layer 65. 82
Figure G15. Layer 70. 82
Figure G16. Layer 75. 83
Figure G17. Layer 80. 83
Figure G18. Layer 85. 84
Figure G19. Layer 90. 84
Figure G20. Layer 95. 85
Figure G21. Layer 100. 85
Figure G22. Layer 105. 86
Figure G23. Layer 110. 86
Figure G24. Layer 115. 87
Figure G25. Layer 120. 87
Figure G26. Layer 125 88
Figure G27. Layer 130. 88
Figure G28. Layer 135 89
Figure G29. Layer 140. 89

Figure G30. Layer 145. 90
Figure G31. Layer 150. 90
Figure G32. Layer 155. 91
Figure G33. Layer 160 91
Figure G34. Layer 165. 92
Figure G35. Layer 170. 92
Figure G36. Layer 175. 93
Figure G37. Layer 180. 93
Figure G38. Layer 185. 94
Figure G39. Layer 190. 94
Figure G40. Layer 195. 95
Figure G41. Layer 200. 95
Figure G42. Layer 205. 96
Figure G43. Layer 210. 96
Figure G44. Layer 215. 97
Figure G45. Layer 220. 97
Figure G46. Layer 225. 98
Figure G47. Layer 230. 98
Figure G48. Layer 235. 99
Figure G49. Layer 240. 99
Figure G50. Layer 245. 100
Figure G51. Layer 250. 100
Figure G52. Layer 255. 101
Figure G53. Layer 260. 101
Figure G54. Layer 265. 102

Figure G55. Layer 270. 102
Figure G56. Layer 275. 103
Figure G57. Layer 280. 103
Figure G58. Layer 285. 104
Figure G59. Layer 290. 104
Figure G60. Layer 295. 105
Figure G61. Layer 300. 105
Figure G62. Layer 305. 106
Figure G63. Layer 310. 106

LIST OF ACRONYMS AND ABBREVIATIONS

AC	Alternating Current
A-M	Additive Manufacturing
CFD	Computational Fluid Dynamics
CFX	ANSYS Workbench's CFD Software
FFF	Fused Filament Fabrication
HCP	Hexagonal Close Packed
PBR	Pebble Bed Reactor
PIV	Particle Image Velocimetry
PLA	Polylactic Acid
PVA	Polyvinyl Alcohol
PVC	Polyvinyl Carbonate
VFD	Variable Frequency Drive

THIS PAGE INTENTIONALLY LEFT BLANK

NOMENCLATURE

ΔP	Differential Pressure (kPa)
V	Velocity ($\frac{m}{s}$)
d	Diameter (m)
ϵ	Porosity
Re_d	Reynolds Number – Hydraulic Diameter
ζ	Loss Coefficient – Packed Bed
ρ	Density ($\frac{kg}{m^3}$)
θ	Maximum Angle Between Spheres (°)
v	Kinematic Viscosity ($\frac{m^2}{s}$)
Q	Volumetric Flow Rate ($\frac{kg}{s}$)
C_v	Valve Loss Coefficient
Re	Reynolds Number – Channel
r_{pipe}	Radius of Channel (m)
r_{coil}	Radius of Helical Spiral (m)
λ	Loss Coefficient – Helical
$y+$	Non-Dimensional CFD Value – Proportional to Distance of Wall vs. First Node

THIS PAGE INTENTIONALLY LEFT BLANK

ACKNOWLEDGMENTS

I would like to thank my advisor, Dr. Walter Smith, for all his mentoring and assistance in making sure I had everything I needed to succeed in this endeavor. Dr. Smith, the staff, and fellow officers were essential in me being able to acquire the knowledge to complete this project. MIDN Kamita was also a great help in preparation and construction. Most importantly, I would not have been able to finish this project without my wife, Madison, and her support, especially during the stressful times with this project.

THIS PAGE INTENTIONALLY LEFT BLANK

I. INTRODUCTION

A. BACKGROUND

Inside a closed loop system, optimizing the operating point of a pump is necessary to conserve energy and dictate the pressure at various components throughout the system. The Navy operates closed loop systems for power production in varying operations. These operations are often deployed and without readily available replacement parts. Being equipped with designs for components that can be readily produced on site will allow the operating points, and the efficiency, of certain loops and cycles to be maintained.

A method of producing components that is portable is additive manufacturing (A-M). A-M has progressed to where metallic A-M is feasible, especially in Navy applications according to Frazier [1]. Aircraft maintenance and parts were outlined in his study where it can be readily made on site to remove delays or minimize imperfections. Additionally, Frazier details how A-M can be used to make parts lighter and less energy intensive. The result of integrating A-M would "enhance operational readiness, reduce energy consumption, and reduce total ownership cost" for the Navy's aircraft, a result that can be directly reflected in other applications such as replaceable loop components [1].

Manufacturing new components on site comes with additional challenges. Both Frazier and Schmelzle et. al. [1,2] note that the type of A-M used, the redesigned procedures for manufacturing and maintenance, and most importantly, redesigned parts will need to be addressed. Re-designed parts need to account for the material used and its inherent strength. Frazier's study shows that certain alloys such as Inconel 625, IN718, and Ti-6Al-4V have lower strength when fabricated by traditional methods. Not only will some materials be weaker, A-M parts will also need to be produced in a way that considers design constraints. Schmelzle et. al. notes in their redesign of Hydraulic Manifolds, the parts were redesigned to eliminate supports on internal features, and to allow for clearances for installation and maintenance, while maintaining original design constraints.

The U.S. Navy is constantly trying to ensure that all their equipment works at their respective maximum efficiency. This is also true of the pumps the Navy uses in their

systems to provide propulsion, generate power, and other vital processes. Pumps are designed to operate within a range of flows and head but also achieve an optimal design point. Pumps operating away from their design points also suffer from excess wear which reduces their life cycle while increasing maintenance costs [3]. At worst, pumps without the correct head present may suffer from cavitation, causing unnecessary vibrations and damage. The maximum efficiency of a pump can be achieved by having the load in the respective loop match the pump's design point [3,4]. When initializing the flow inside a loop, a sufficient load may not be present, leading to mismatches and reduced pump performance. A method to mitigate this effect would be to insert an artificial load that causes head loss to simulate the final load inside the design loop.

Currently, the Navy utilizes components to cause further head loss in addition to the loads found in normal steam power generation or other heat rejection applications. Some pressure drop component designs utilize flow being directed through channels that are cut through a series of plates. The channels are offset and alternate, which cause the resulting streamlines to impact the next plate, dissipating energy, before redirecting into the next series of channels. A schematic is seen in Figures 1 and 2.

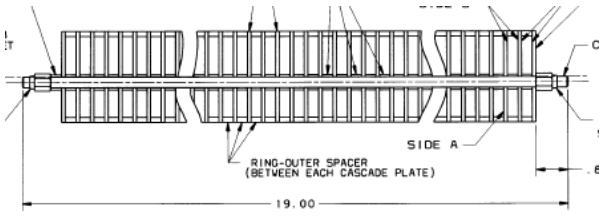

Figure 1. Example of Pressure Loss Device.

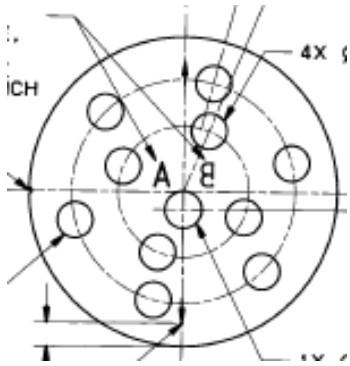

Figure 2. Cross Section of a Pressure Loss Device.

Production of these devices and many other components are generally machined. This leads to potential maintenance delays, availability issues, and limits adaptation to different systems [1]. The growing adaptation of Additive Manufacturing and its capabilities allows for readily produced components that can be designed and made on site. For smaller parts, metal A-M can be used for replacements. A-M can be used to produce an entirely different model or adjust current models to vary operating points. The methods in which the component is produced also allow for a wider range of different designs and geometries. Designs that cannot be made in subtractive manufacturing, including ones where unfeasible amounts of post processing are required, can now be made as one printed part. Similarly, whole assemblies can be printed together, or in a way where single parts are easily combined.

A-M production for metal printing range from Fused Filament Fabrication (FFF), Energy Deposition, and Powder Bed Based methods. The methods have their own advantages and disadvantages but allow for "part consolidation" instead of machining several individual parts [2]. Part consolidation removes the subtractive manufacturing of machining a component in different parts and then assembling them afterwards. Complex solutions to replace current components can then be utilized to produce a single part. Certain methods, such as FFF A-M, can produce parts containing overhangs or sharp corners without the need for secondary machining. This is done through the printing of easily dissolvable support material in conjunction with the metal print. Some methods are unable to accomplish this, but since FFF works by extruding material filament through a

nozzle, the alternating of different material in the same print is possible. Schmelzle [2] notes that while this may provide a greater range of designs, further considerations must be taken into consideration. Schmelzle [2,5] and others have also noted that A-M processes will result in a plane that is weaker than the other two in an X-Y-Z coordinate system, dependent on direction manufactured. Smith [6] shows how a prototype part made from polycarbonate exhibits drastic variance in tensile strength depending on which orientation the part was printed. Evaluation of the material and component should be done with different print directions with special attention paid to areas of stress concentration [2,5,6].

For an austere environment in which a new design is not required, A-M allows current production to be streamlined. Parts can also be printed to have pre-designed assembly points, minimizing the number of failure points [5]. This, combined with the lower man hours to produce may allow for greater operational capability for an operating ship. For example, some components are generally machined into plates, placed onto supports, and then bolted in. The same plates can be printed using existing technologies that would be able to mate directly into the next plate. Rupal [7] has noted the success of this approach by utilizing finite element thermo-mechanical simulations and the combination of known geometric tolerances of each tested machine to predict the viability of junctions. The study notes that having both male and female junctions printed result in higher deviations, which will vary the strength of the corresponding mate. Mitigation of this can be achieved by further refining the tolerance of the machine reducing final deviation, automated and precise post-processing to increase mating performance, and performing continued tests on printed samples to improve the model. Rupal [7] notes that by taking these approaches and implementing an adequate procedure, A-M production of current designs also prove viable.

B. MOTIVATION

The purpose of this study is to produce and evaluate alternative components designed for inducing a pressure loss in a fluid flow that can be additively manufactured. Utilizing different models and methods to produce head loss may also alleviate negative characteristics such as vibration. The data collected from various designs will allow for

optimization of operating points to match design points of a given pump. The pressure drops observed through various components and compared with analytical results to determine viability. In addition, the designs produced will be easily modifiable for interchangeability with different systems.

C. OUTLINE

Design will begin with a literature survey exploring previous examples of unconventional pressure loss components. Evaluation for possible design replacements will be conducted using Computational Fluid Dynamics (CFD) with a similar approach to the study by Karode [8] on flow through rectangular channels. Determining the pressure drop concurrent with the drag and flow visualization will allow the design goals to be met. Experimental results will be gathered using a scaled test loop constructed using conventional parts. This project is designed to reproduce a given head loss which can be characterized by the Valve Loss Coefficient (C_v). The target C_v was 7.0 which translates to 343.36 kPa (49.8 psi) through a 2.84 kg/s (45-gpm) flow.

THIS PAGE INTENTIONALLY LEFT BLANK

II. DESIGNS

A. BACKGROUND

Numerous possible types of geometries to build devices to produce a pressure drop were examined. The factors considered for these devices were the use of previous experiments confirming pressure drop potential, initial sizing, and feasibility to be produced using an A-M approach. Though designs such as Tesla Valves, Microgrids, and variations of the current pressure drop component, seen again in Figures 1 and 2, were considered, two models were decided on; A pebble bed model with previous experimental data from reactor usage was the ideal candidate to illustrate how complex geometries can be produced using A-M is the first model. The second model uses a basic tube that is elongated into helical spirals to maximize loss from the length of flow and the head loss felt in flow redirection.

B. PEBBLE BED

A pebble bed model was derived from idea of a Pebble Bed Reactor (PBR). The PBR was a nuclear power generation plant most recently constructed in South Africa. Instead of fuel cells or channel designs, the PBR utilized a conglomerate of fissile material pellets contained within a sphere for heat transfer, moderation, and structural integrity purposes [9].

1. Model Details

Initial designs and testing of this concept were completed to evaluate a PBR design that was compact and able to produce power in austere environments. In an examination of such designs, numerous models were developed for hydraulic calculations [8]. The pebble bed design utilizes numerous changes in flow direction due to the spacing of spheres to incur a pressure drop in the part [9]. Spheres are aligned in a manner that represents a hexagonal close packed unit cell that fluid flow is forced through. This can be seen in Figure 3.

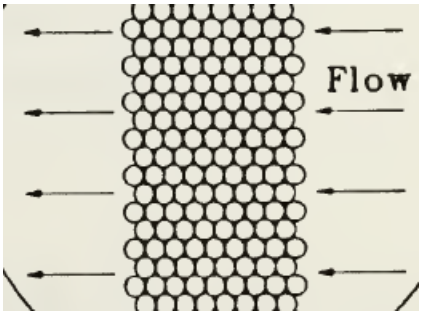

Figure 3. 2-D Packed Bed Flow. Source: Casey [9]

A consideration moving forward was the variation that will occur due to the faces being faceted together. Junctions are required to fix the spheres to maximize volume inside the component. Previous studies had the spheres free of junctions. Previous designs also relied partly on vibration to help dissipate any flow misdirection, lowering pressure drop. The Pebble Bed's junctions will mitigate those vibrations which is advantageous for pressure drop and wear of the component.

2. Analytical

Comparing Herbert's [10] and Susskind, et. al.'s [11] studies on similar shaped design, and Idelchik's [12] analysis of flow through aggregate spheres, the simplified, thermally independent pressure drop (ΔP) can be modeled. Equation 1 shows the pressure drop with respect to the void factor or porosity (ϵ), seen in Equation 2, Reynolds number (Re_d) in Equation 3, and loss coefficient (ζ) in Equation 4.

$$\Delta P = \rho \frac{V^2}{2} \zeta \tag{1}$$

$$\varepsilon = 1 - \frac{\pi}{6\left(1-\cos\theta\right)\sqrt{1+2\cos\theta}} \tag{2}$$

$$\mathrm{Re}_d = \frac{\dfrac{0.45Vd}{\left(1-\varepsilon\right)\sqrt{\varepsilon}}}{v} \tag{3}$$

$$\zeta = \frac{L}{d}\left(\frac{30}{\mathrm{Re}_d} + \frac{3}{\mathrm{Re}_d^{0.7}} + 0.3\right)\left(\frac{1.54}{\varepsilon^{4.2}}\right) \tag{4}$$

In the previous equations, ρ is the density of water, V is the inlet velocity, d is the diameter of the balls, θ is the angle of the spheres respective of each other, v is the kinematic viscosity of the liquid, and L is the length of the overall component. The ΔP can be inserted into Equation 5 to calculate the unitless C_v, a flow coefficient relative to the pressure loss efficiency of a component. C_v, based on calculations using imperial units [12], is lower for a component that reduces more pressure at given mass flow rate.

$$C_v = \frac{Q}{\frac{gal}{\min}}\left(\frac{1}{\frac{\Delta P}{psi}}\right)^{0.5} \tag{5}$$

Utilizing the analytical models as a sizing guide, a series of interconnected Hexagonal Close Packed (HCP) spheres was designed. The calculations are shown in Appendix A. Using spheres that are 0.0222 m (0.875”) spaced at 0.0216 m (0.85”), a model is developed which is 0.0635 m (2.5”) long consisting of 4.5 sphere layers, with a diameter of 0.0844 m (3.325”) using SOLIDWORKS modeling software. The first layer is the unmolested sphere faces shown in Figure 4. The cross section is presented in Figure 5.

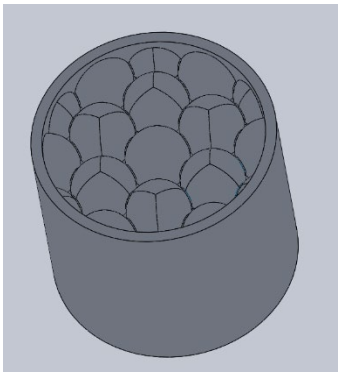

Figure 4. Packed Bed Model

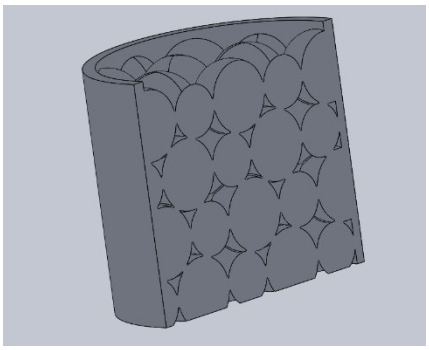

Figure 5. Packed Bed Cross Section

The resulting designs have values of a ΔP of 268.30 kPa (38.91 psi) and a C_v of 14.91 by using the Equations 1–5. All results are seen in Appendix K. The packed spheres will utilize the same contraction and expansion through channels as other components, but the velocity streamlines will have a smoother transition upon exit. This should reduce pressure through the dissipation of the turbulence energy at the sloping surfaces. There will also be friction losses as well through the numerous surfaces within the model.

3. Production

Production of the Packed Bed was completed using Xerox's Elem-X 3-D Metal Printer [13]. Construction of the model first began with saving the SolidWorks model as a .STL file. SolidWorks prompts the user to designate how coarse or fine the mesh will be. In this situation, the default Fine selection is recommended as seen in Figure 6. The Fine setting sets the tolerances up to 10° before a new mesh cell is created and a tolerance of 64.77 um (0.0255 in). These are adequate as the design guide for the printer has a coarser requirement.

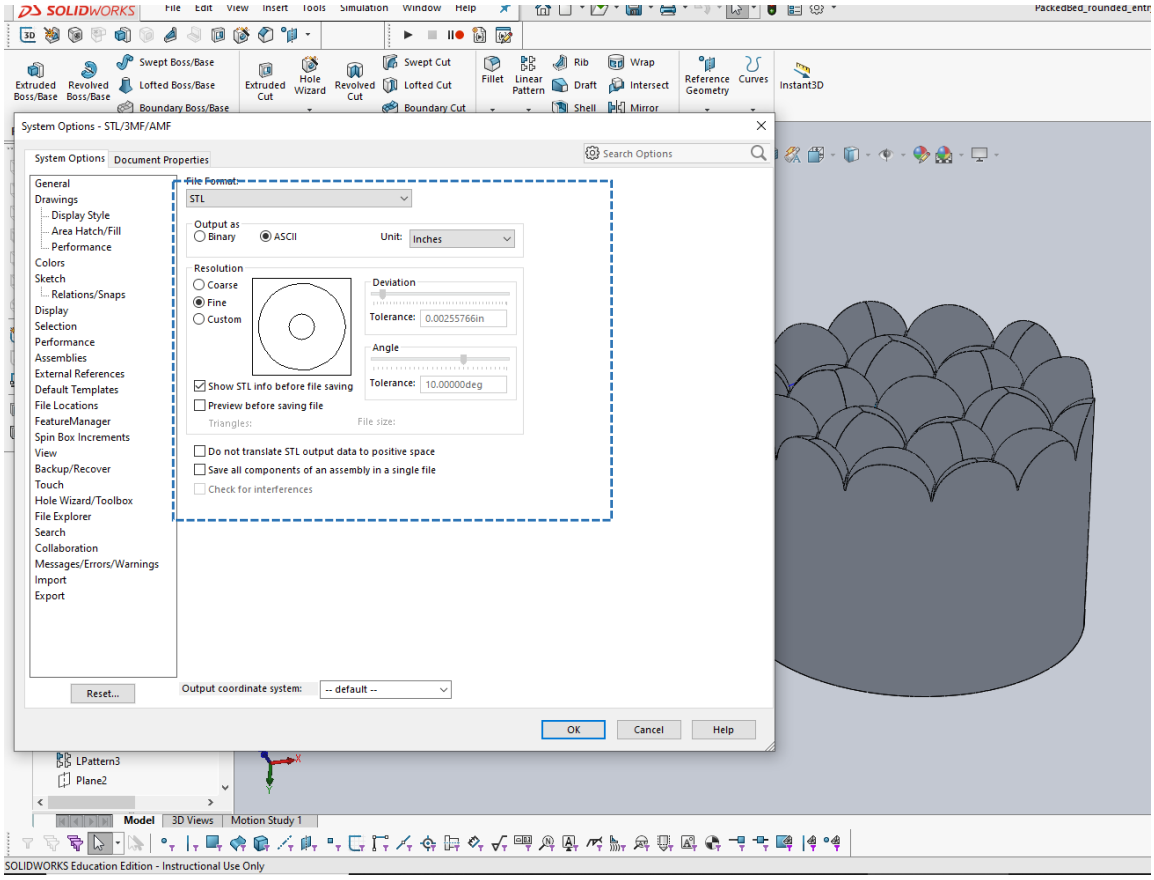

Figure 6. SolidWorks .STL Creation

After a creation of a .STL file, the model is then refined using the open software Meshmixer. The software's "Make Solid" option is shown in Figure 7.

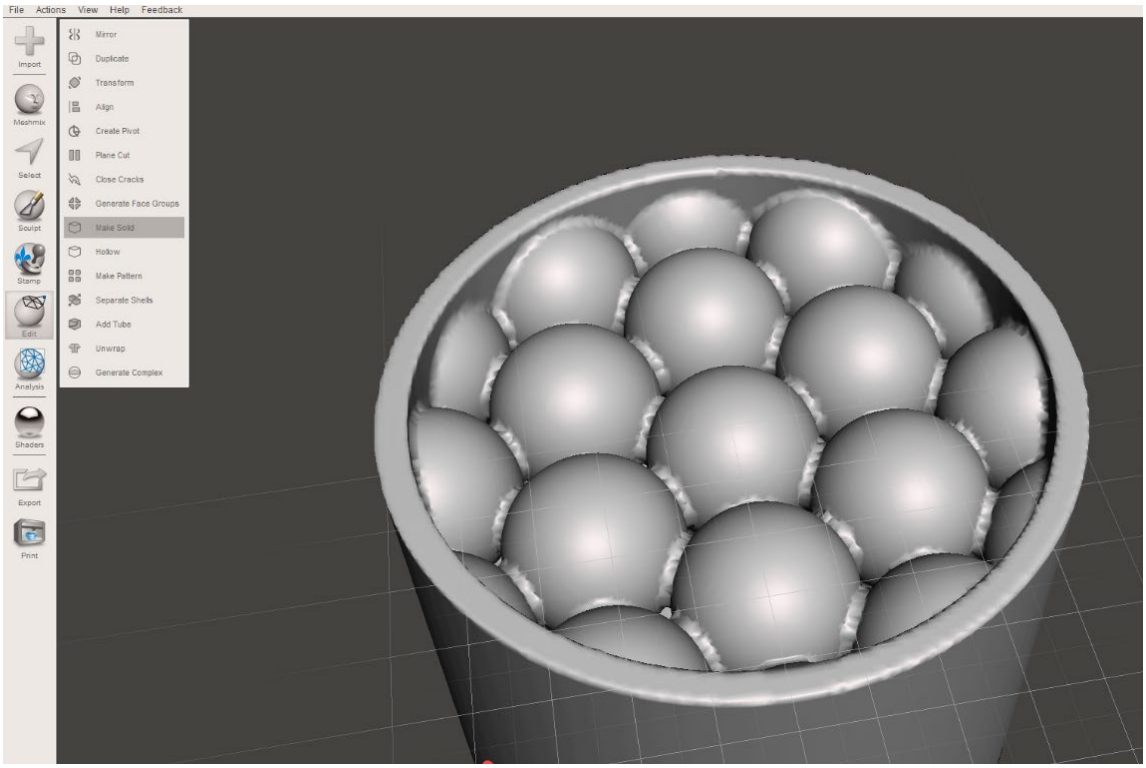

Figure 7. Meshmixer Make Solid Function.

"Make Solid," refines the minimum thickness of the walls and junctions while closing any openings that may have occurred through meshing. This is crucial to A-M any part. As seen above, the part is very rough and bulky. "Make Solid," allows the user to also designate the specifications as well, shown in Figure 8.

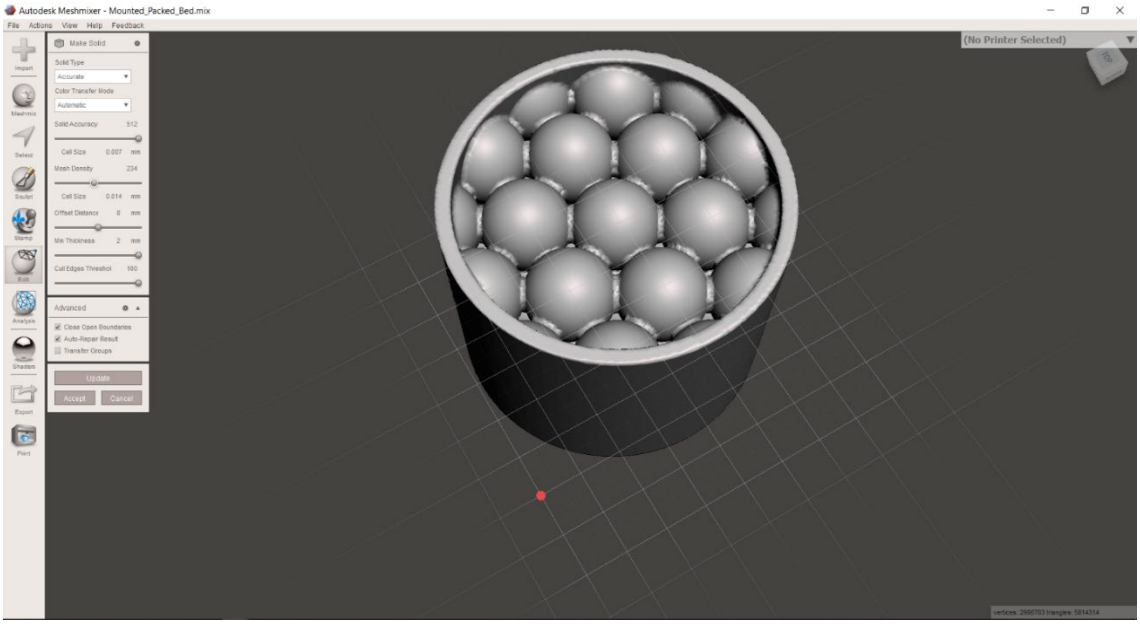

Figure 8. Make Solid Function Refinement.

The printer settings of the specific model can be uploaded on the screen to the top right. Specific Xerox Elem-X settings are outside the scope of this thesis. As the Packed Bed will use Xerox's proprietary printer, settings must be manually inputted. The finished .STL is seen in Figure 9 and will is ready to be sliced. The edges are sharper and the junctions between spheres are more precise.

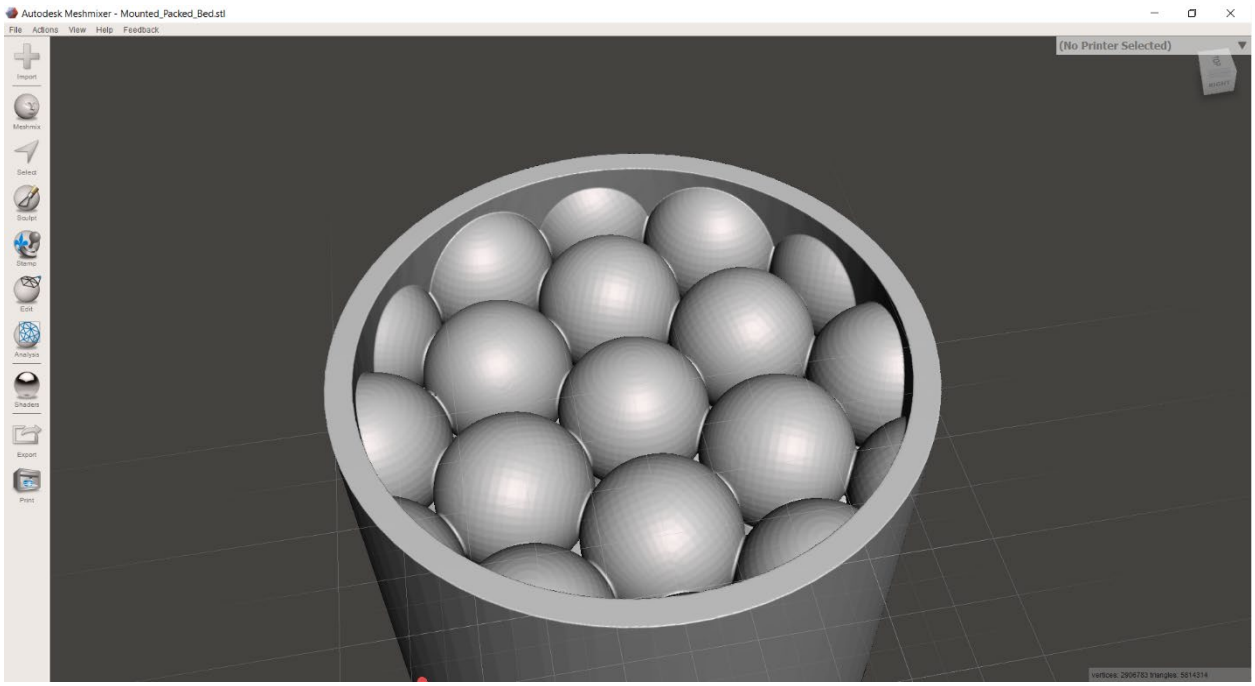

Figure 9. Post Mesh Mixer Packed Bed Model.

The slicing software used is Xerox's own proprietary Elem-X Slicer, developed specifically for use with the Elem-X Printer [13]. The initial print, without the mounting guard on top of the model, required 12 hours to finish and cool and is seen in Figure 10.

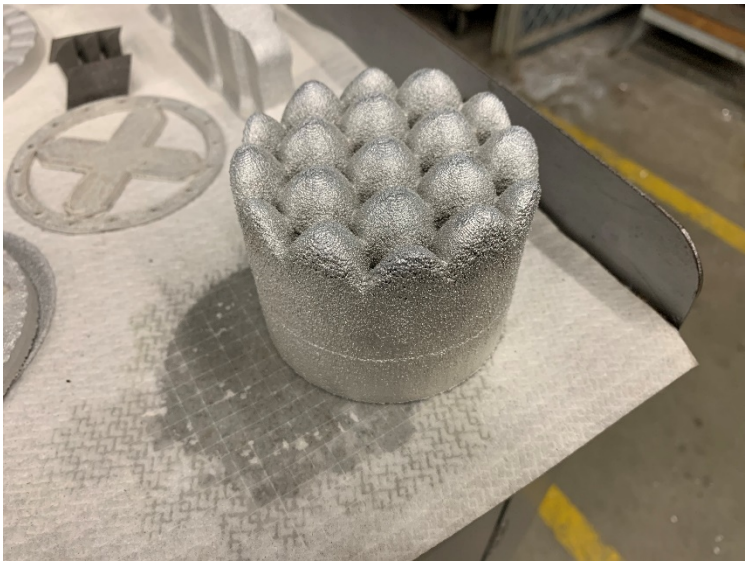

Figure 10. Packed Bed Model Printed.

The product was printed with a few flaws. The overall clearances between each sphere are much tighter than expected, due to possible excess spray within the printer. This was predicted to result in a higher pressure drop than expected within the physical test. In addition, the possible spray spread caused the flow channels to also be narrower, possibly further causing increased pressure reduction. An example of these exit channels can be seen in Figure 11. Machining was not deemed time effective as the only the first layer is exposed, and the interconnecting filets would be too time intensive to thin and clean out without damaging any further layers or the integrity.

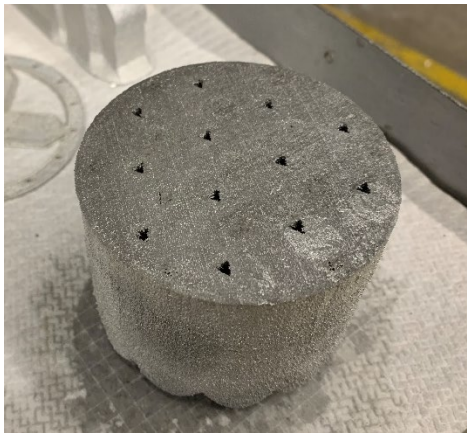

Figure 11. Narrower Exit Channels for Packed Bed Model

A second print was then ordered using an updated version of the printer software in addition to some design changes to the packed bed. The new print had a mounting ring seen in Figure 9, placed on the inlet to allow mounting in the test section without contacting the spheres. The second design change is to remove a quarter layer of the bottom sphere so the outlet will have wider channels. The new print can be seen below in Figures 12 and 13. With the improved software, the spatter from the nozzle was reduced. Though there is some roughness present, the inlet channels are less clogged which will result in better agreement between the predicted and measured pressure drops.

Figure 12. Second Packed Bed Print

Figure 13. Outlet Openings

The newer software allowed for real time scanning to observe the print as it's being built. Figure 14 shows the initial base, in which the wider outlets are shown. Figure 15 illustrates the print at the halfway point and Figure 16 is the print at its conclusion. Both X and Y axes in these Figures are distance on build plate. The colored bar on the right of the Figures annotates the distance away from the nozzle at time of deposition. The Elem-X is designed to either vary deposition droplet size relative to the nominal difference, set at 12 mm.

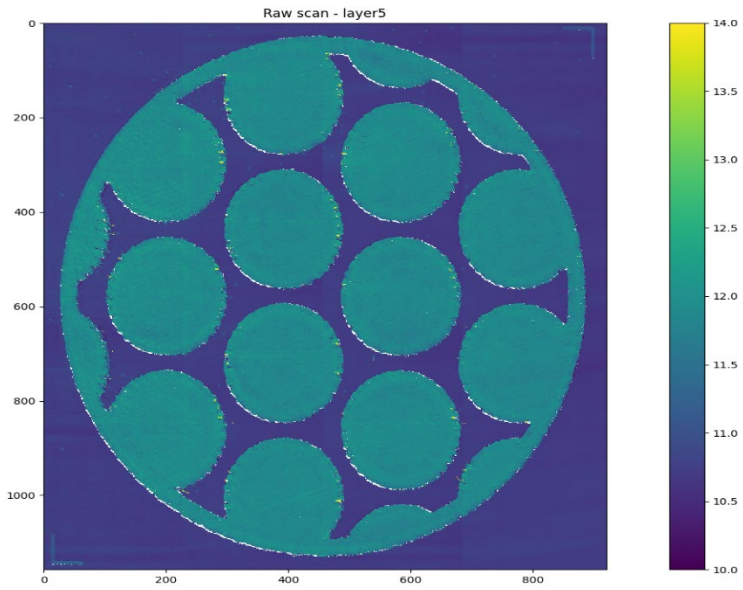

Figure 14. Packed Bed Base Scan – Layer 5

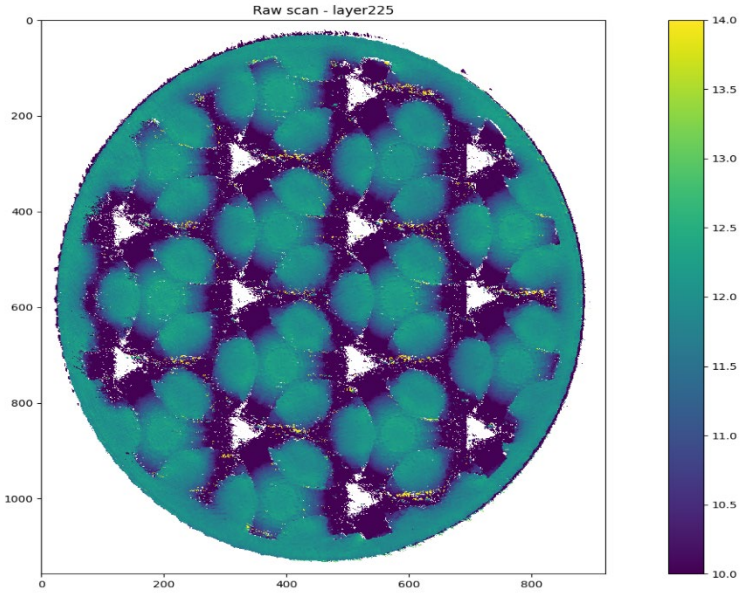

Figure 15. Packed Bed Junction Growth – Layer 225

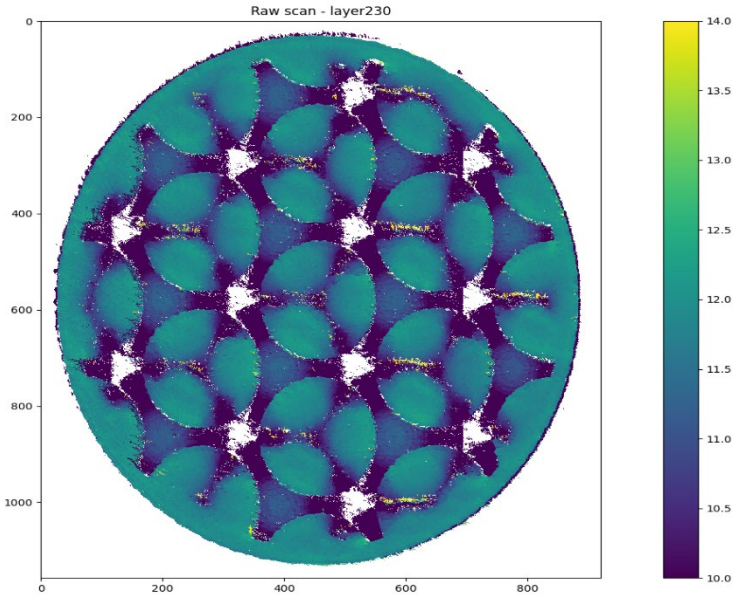

Figure 16. Packed Bed Junction– Layer 230

A-M allows the outlet seen in Figure 14 and the junctions seen in Figure 15 and 16 to be produced seamlessly. The growth of the junctions is seen in the difference from Figures 15 and 16 which proves the A-M process is viable and effective. Machining the spheres separately would require an operator to individually sinter each sphere together in that precise pattern. This would be time and labor intensive while printing the part like this allows manufacturing to be done autonomously with similar results.

An additional benefit of this type of real time scanning is the ability to project the scans into a 3-D representation. Using the MATLAB script seen in Appendix H, each layer is read, and a 3-D graph is propagated, seen in Figures 17 and 18.

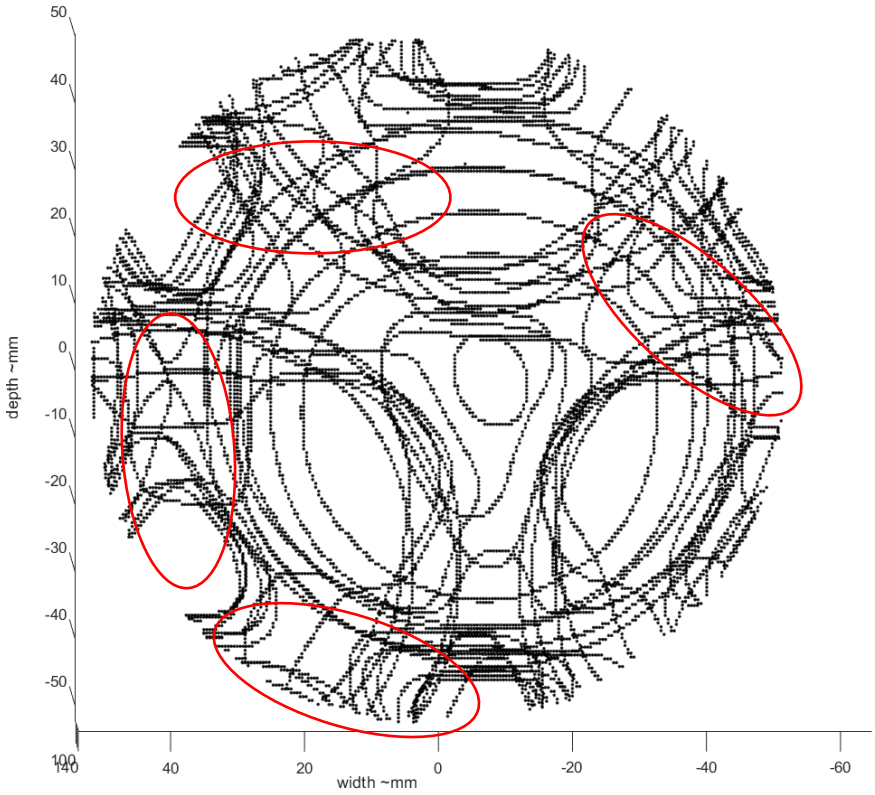

Figure 17. 3-D Packed Bed Scan Top View

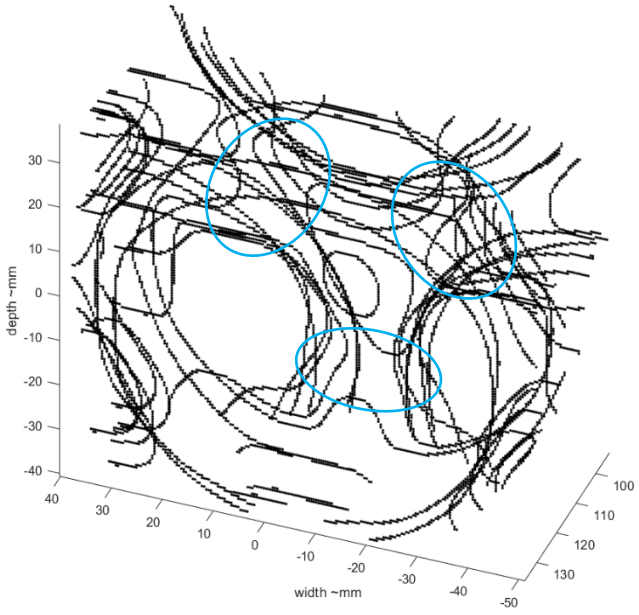

Figure 18. 3-D Packed Bed Scan Side View

Figure 17 shows the top view, with the in-plane sphere junctions highlighted in red. Figure 18 shows a side view where the 3 junctions to the next layer of spheres is highlighted in blue. The real time scanning coupled with a topographical view further improves A-M's viability by allowing the user to ascertain possible flaws or defects in a nondestructive fashion. As the scans are integrated into the Elem-X printer, each print can be inspected immediately after completion to increase overall reliability. This also allows an 'As built,' solid model of the part to be generated which is extremely useful in simulations before using the part in operation.

C. HELICAL CHANNELS

Another model investigated was the Helical Channel Model. The head loss affected by fluid flow through a pipe from friction have been studied and modeled extensively. Bends within flow loops also yield minor head losses through flow redirection, as well. Utilizing the loss from flow redirection would theoretically lower unnecessary vibration as less turbulence is generated [13].

1. Model Details

Current studies are limited as most helical pressure reducing components studied utilized a greater length and wider pitch than what is feasible in this system [14, 15]. The theoretical principles and assumptions use for the analysis are still the same once the initial turbulent entry dissipates. Initial studies assumed that complete laminar flow was achieved which is not capable in this set up as the Reynolds numbers were high enough that turbulent flow would be expected. This analysis will instead use the transitional flow models and loss coefficient for bends to develop pressure predictions. The model is shown in Figure 19.

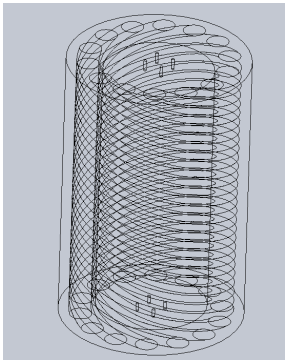

Figure 19. Helical Model Cross Section

2. Analytical

Idel'chik presents the most applicable results when examining the short and sharp helixes of the current design [12]. The new model was designed utilizing 14, 0.0101m (0.4") diameter channels at a pitch diameter of 0.0648 m (2.55") and a pitch of 1. The ΔP for the model is developed in Equation 6.

$$\Delta P_T = \Delta P_i n \tag{6}$$

The overall ΔP_t is the combined pressure drop of each channel ΔP_i, by the number of channels seen in Equation 7 where f is the friction factor, V_i is the velocity through each channel, and the density, ρ.

$$\Delta P_i = 2fV_i^2\rho \tag{7}$$

The f used is dependent on the Reynolds Number, Re, of each pipe seen in Equation 8 where μ is the dynamic viscosity. The corresponding equations for friction factor and loss coefficient, λ, are seen in Equations 9 and 10 where r_{coil} is the radius of the overall helix, $r_{pipe}$is the radius of each pipe, and θ is the total angle that the flow is directed, in degrees.

$$\mathrm{Re} = \frac{\rho V_i 2r_{pipe}}{\mu} \tag{8}$$

$$f = 0.0175\lambda\left(\theta\frac{r_{coil}}{2r_{pipe}}\right) \tag{9}$$

$$\lambda = \frac{5}{\mathrm{Re}^{0.45}}\left[\frac{r_{pipe}}{r_{coil}}\right]^{0.275} \tag{10}$$

The calculations for this model can be seen in Appendix E. The resulting C_v is 8.66 for this model with a ΔP of 180.60 kPa (26.19 psi).

3. Production

Production of the Helical Model was completed in PLA using an 'Ultimaker 3' 3-D Printer [16]. The model is designed in SolidWorks and exported using the same method as the Packed Bed model. The model was also put into Meshmixer to solve any possible solid errors. The slicing software used was Ultimaker's Cura software. The final print time was 3 Days and 15 hours.

The decision to utilize PLA plastic instead of metal in this scenario was that the Helical Channel would be under less stress in the X-Y plane allowing use of a weaker material. Printing in plastic also allowed the experiment of printing with and without PVA support to assess necessity. This also cut down on reliance on the metal printer Xerox Elem-X [13] which was undergoing maintenance and updates at the time of production.

Considerations had to be taken for the initial loops and the higher velocities observed, which resulted in thicker walls at the entrance. The first print using support failed catastrophically due to inherent moisture inside the support. The model was found not to require support and can be printed free standing as evidenced by the overhangs at the top of the build, shown in the red circle in Figure 20.

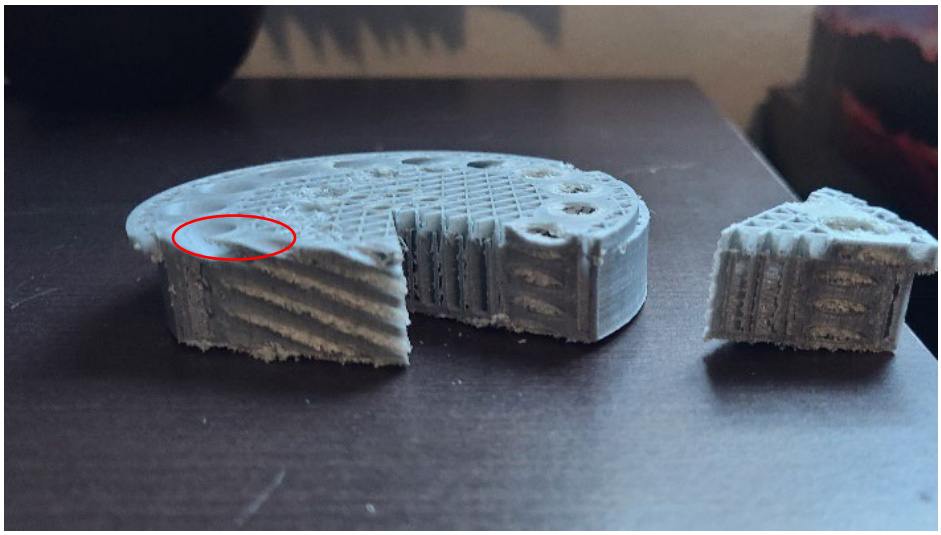

Figure 20. Failed Print Cross Section with Support.

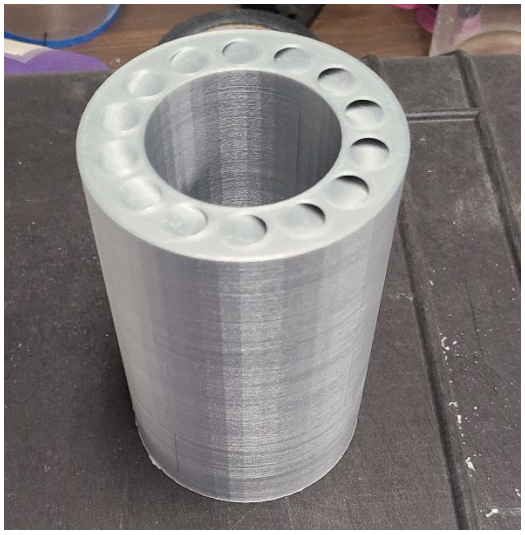

Figure 21. Helical Model.

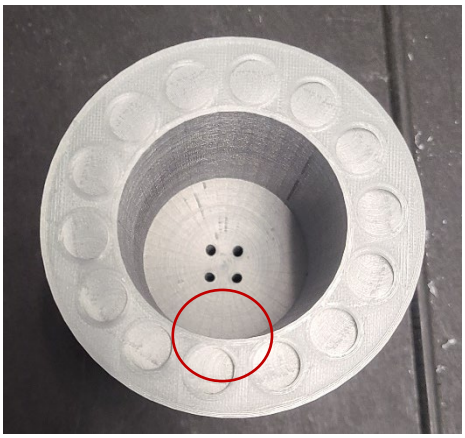

Figure 22. Helical Model Top View.

The final print can be seen in Figures 21 and 22 does not require any post-processing due to its simple design and lack of supports. The center is hollow for weight considerations with 4 small orifices in the center of the plate. The orifices, highlighted in the red circle in Figure 22, are negligible due to their small size and their design to relieve areas of back pressure within the component. There is also no back plate for further weight reduction.

THIS PAGE INTENTIONALLY LEFT BLANK

III. EQUIPMENT

A. A-M PRODUCTION MACHINES

Production of the components utilized two different A-M Printers. The decision to use two different printers was again due to maintenance of the Xerox Elem-X. The Elem-X boasts faster production times than previously seen in other machines. The print times for similar builds can be seen in Appendix K.

1. Xerox Elem-X Aluminum 3-D Printer

The Xerox Elem-X printer is a metal filament, nozzle fed, argon shielded, deposition printer produced by Xerox, seen in Figure 23. This printer is the first one released of its kind and licensed to NPS for student and faculty use. Parts produced on this printer are rapidly cooled in a liquid bath to remove from the build plate [13].

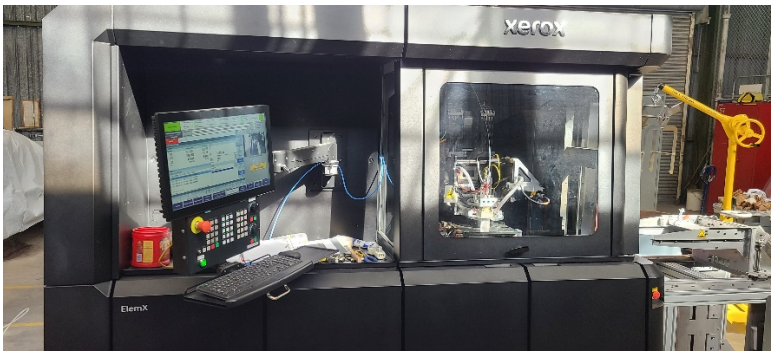

Figure 23. Xerox Elem-X Printer

2. Ultimaker 3 3-D Printer

The Ultimaker 3 printer, seen in Figure 24, used for the Helical design is a plastic filament fabricator utilizing two possible material injection nozzles, removable print cores for different types of materials, with speeds up to 16 mm^3/s extrusion speed. The maximum build volume is 215 mm x 215 mm x 200 mm [16].

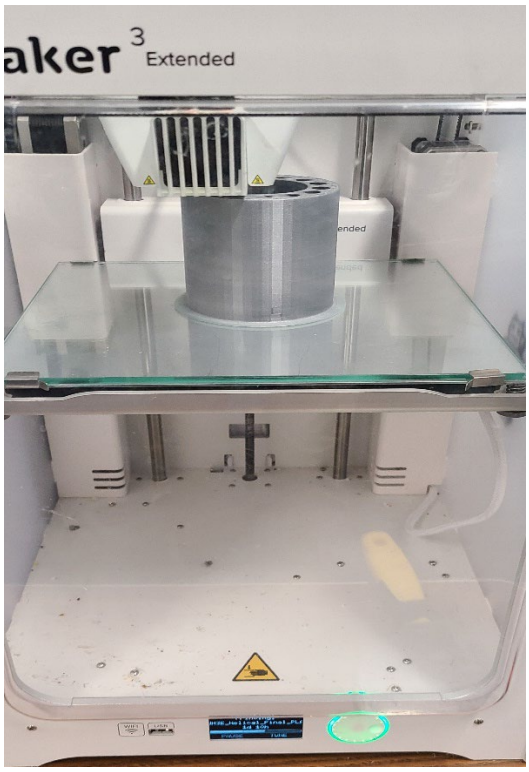

Figure 24. Ultimaker 3 Printer.

B. TEST LOOP FACILITY AND COMPONENTS

1. Loop Design

The test loop that was designed is composed of 4 main legs pictured in Figure 25.

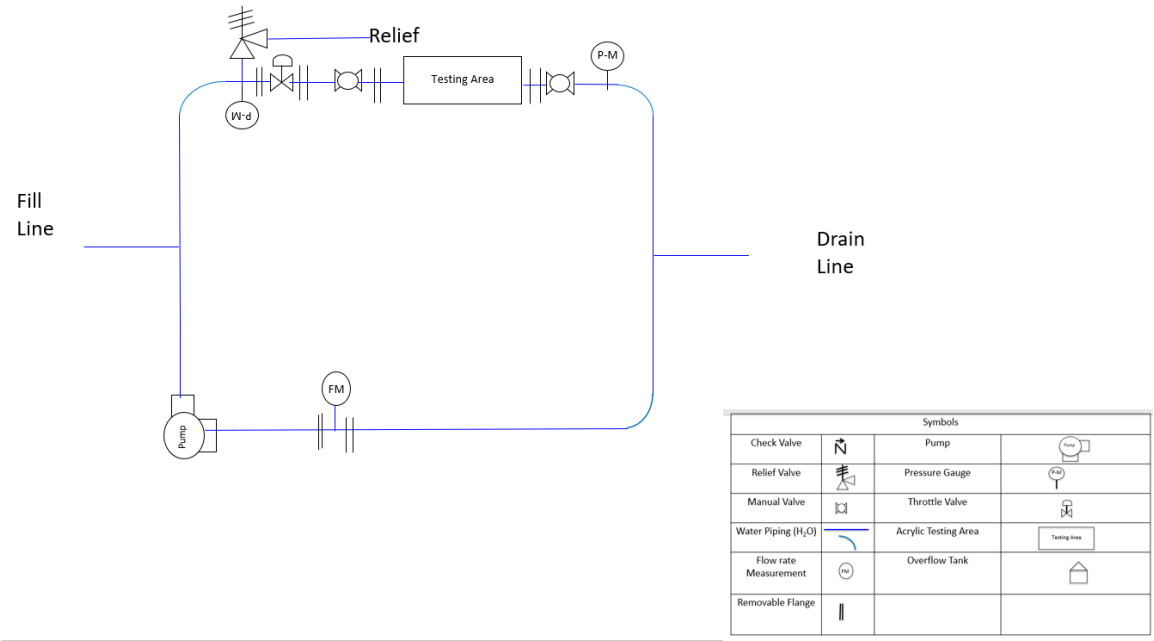

Figure 25. Test Loop Schematic Diagram

The four main legs are composed of primarily Size 4, Schedule 40 PVC pipe with 3 corners comprising of two 45° corners to minimize sharpness of curves. The inlet leg receives the discharge from the pump as well as a PVC pipe for filling of the loop. The test leg inlet receives the inlet leg discharge where a pressure monitor device and a pressure relief are located. The relief is set to 689.48 kPa (100 psi) providing a factor of safety of 1.5 for its most limiting component located at the isolations on the inlet and outlet legs. The pressure ratings for each component of the pressure vessel are in Appendix J and is up to ASME Standard B31.9. The acrylic test section was ensured to have a built-in factor of safety of 10 to ensure the brittleness of the part does not cause failure.

The flow then continues through a butterfly valve and gate valve, both with removable flanges on each side. The test section comprises of a 0.152 m (6”) long acrylic section confined by an open box to house water. All pressure vessel pipes are Size 4 U.S. custom or 10.16 cm (4”) inner diameter. The inlet and outlet legs utilize Size 1.5 PVC junctions, or pipes with a 3.81 cm (1.5”) inner diameter. This open box allows observation of flow and turbulence and allows for opportunity to use other measuring devices in the future such as Particle Image Velocimetry. The test section is also connected to removable

flanges for interchanges. Flow then travels by another pressure monitoring device before reaching the outlet line where a drain line is also present to discharge the loop. After the discharge section, flow travels to the Velocity Measurement (VM) section. The venturi used for velocity measurements is placed at 1.52 m (5') away from the inlet and is removable through two flanges. The loop's initial construction is seen in Figure 26.

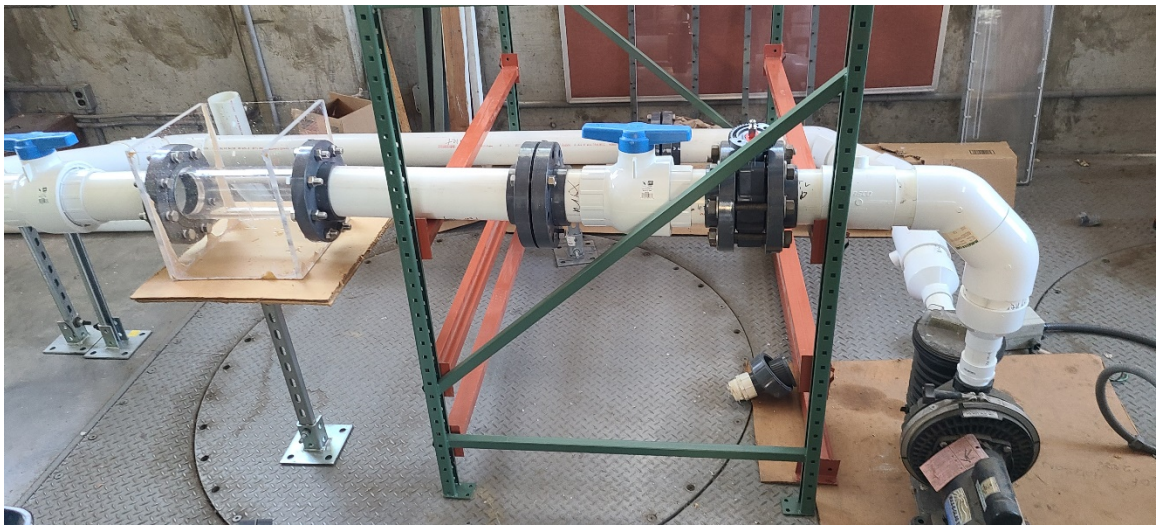

Figure 26. Initial Testing Loop Construction.

2. Pump

The pump in this experiment is a 560 W (3/4 hp) 120V centrifugal water pump (McMASTER-CARR - 8249K82). The maximum flow rate is 4.54 $\frac{kg}{s}$ (72 gpm) with a maximum pressure of 1380 kPa (200 psi) [17]. The pump can be seen Figure 27.

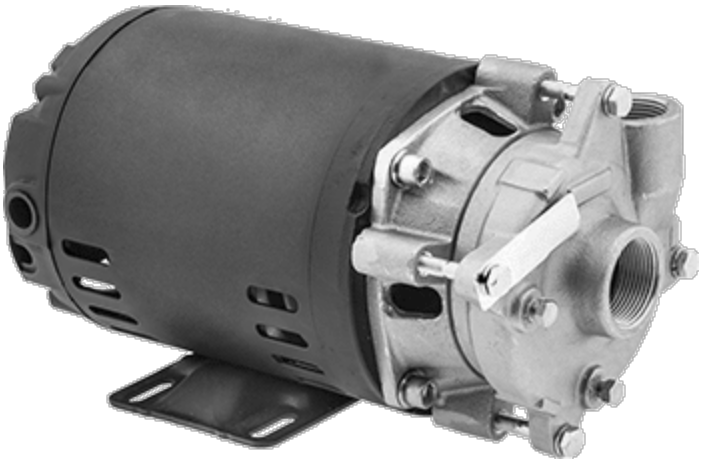

Figure 27. McMASTER-Carr Part 8249K82.

3. Variable Frequency Drive

The Variable Frequency Drive (VFD) used in coupling with the motor in this experiment is the Fuji Electric – FRN0010C2S-2U seen in Figure 28. This VFD is configured for 1 phase 115V with a range of 93 to 746 W (1/8 to 1 hp) motor.

Figure 28. Fuji Electric – FRN0010C2S-2U.

4. Flow Monitoring Devices

To acquire data from the loop, different monitoring devices are placed into the loop. These instruments will measure the flow characteristics and changes resulting from the inserted pressure loss device.

a. Venturi – Velocity Measurement

Velocity measurement inside the loop will utilize a 3-D printed venturi placed at bottom leg in Figure 25. The Venturi is a cost-effective component which operates on the basic Bernoulli's principle to determine velocity. A simplified Bernoulli's equation, negating any height differential is presented in Equation 11 where P is the pressure, ρ is the density of the fluid, and v, is the velocity at each point [19,20].

$$P_1 + \frac{\rho v_1^{\,2}}{2} = P_2 + \frac{\rho v_2^{\,2}}{2} \tag{11}$$

$$Q = A_o \sqrt{\frac{2}{\rho} * \frac{\Delta P_{low}}{\left(\frac{A_o}{A_i}\right)^2 - 1}} \tag{12}$$

$$Q = Av \tag{13}$$

The difference in pressure is measured using the Venturi component itself and substituted into a calibration equation, Equation 12, where Q is the volumetric flow rate, A is the area of the respective locations, and the ΔP is the differential at each relative location. The flow rate Q rate can then be converted to velocity using the conservation of mass equation in 13.

The Venturi used in this system was designed with corresponding calculations found in Appendix I. The design is based on having a pressure transducer with a 138 kPa (20 psi) range inside the system, allowing enough of a differential to be observed between monitoring points. The Venturi, seen in Figure 29, is printed using Elem-X printer technology.

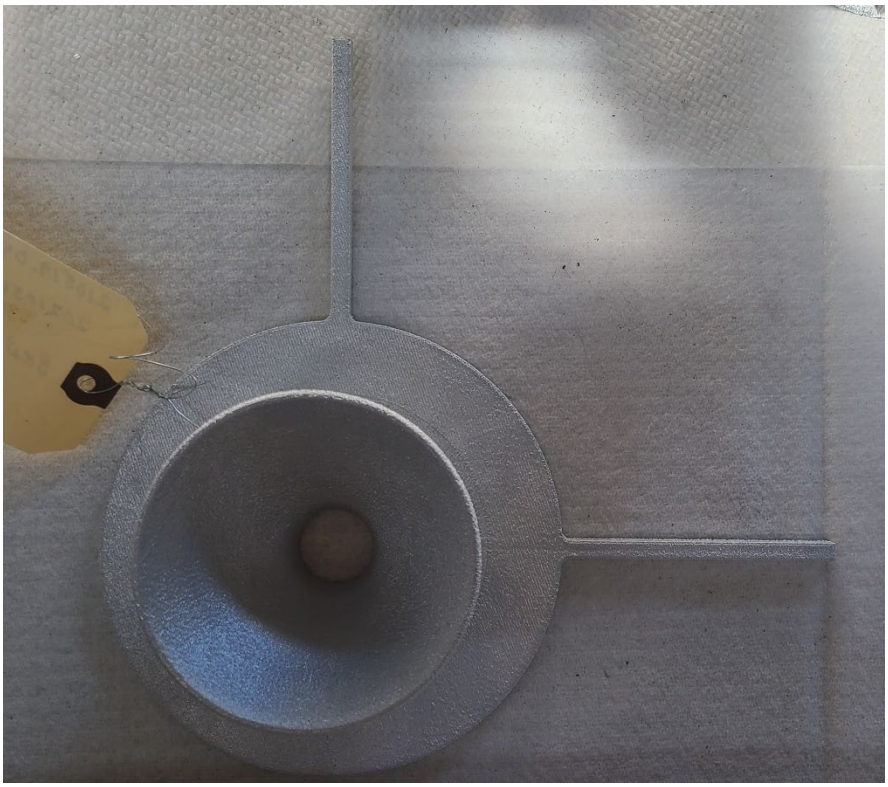

Figure 29. Elem-X Printed Venturi

b. Pressure Monitoring

The data acquisition control unit, seen in Figure 30, is the National Instrument CDAQ 9181. This unit receives input through either analog or digital sensors and is designed for wet environments [21].

Figure 30. CDAW 9181.

The sensors used are the Omega PX273, wet differential pressure sensors seen in Figure 31. The PX273 is rated for 0 – 137.90 kPa (0-20 psid) differential pressure.

Figure 31. Omega PX273.

5. Equipment Scaling

a. Pump

Future loops will use a different pump that more accurately reproduces flow within a heat rejection system. The pump is a U.S. Electrical Motor, ID B530, mounted on a UNIMOUNT 125 Frame 286T body, seen in Figure 32. The pump is a 3 phase AC motor running on either 230 or 460v. The UNIMOUNT 125 operates at 1765 rpm with an efficiency of 91% at its designed operating point. This experiment was unable to use this pump at the time due to electrical capabilities in B213 of the Turbopropulsion Laboratory.

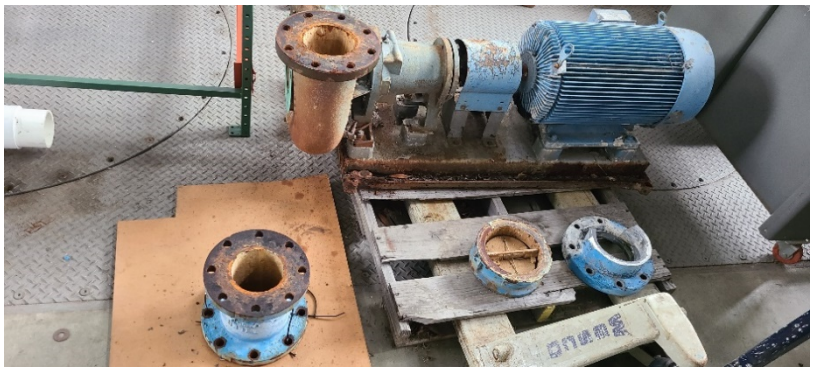

Figure 32. UNIMOUNT 125 ID B530 Pump.

b. VFD

The VFD to be used in conjunction with the UNIMOUNT 125 B530 is the Ac Tech M32250B, seen in Figure 33. The M32250B can be used with pumps up to 15 kW with an input voltage of 240/480 V. Like the UNIMOUNT 125 B530, wiring limits at the time did not allow installation.

Figure 33. Ac Tech M32250B VFD.

THIS PAGE INTENTIONALLY LEFT BLANK

IV. RESULTS

A. COMPUTATIONAL

To gather computational results, each model must be inserted into a CFD software and flow characteristics calculated. Both models underwent the same process and analysis.

1. Packed Bed

Analysis was completed using ANSYS Fluent – Workbench's CFX software [23]. The effects that occur after two layers should be repeated at each additional layer, reducing computation time, and allowing for more detailed analysis. The first initial CFD run was designed in order gain a starting mesh. The model utilized only had one "unit cell" at the inlet, rather than the full diameter, and two layers in thickness to minimize the runtime necessary. The differences between a whole-body model and a "unit cell" can be seen in Figures 34 and 35.

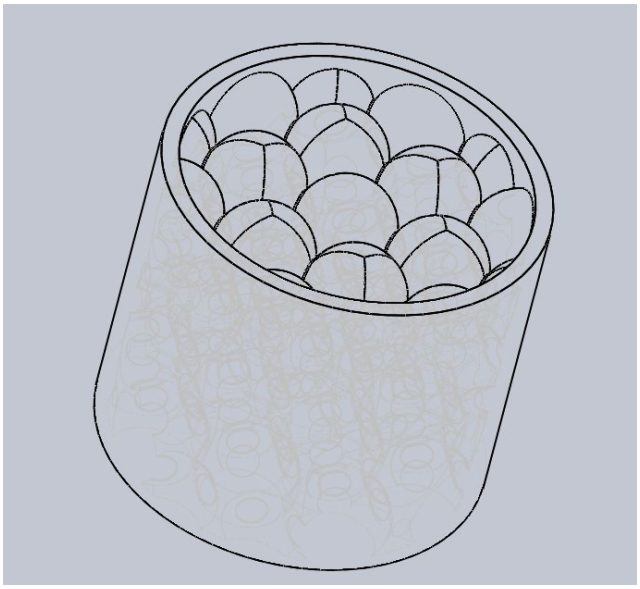

Figure 34. Whole Body Packed Bed.

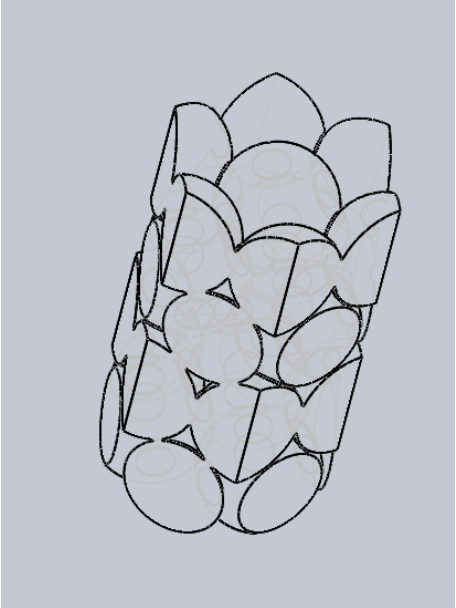

Figure 35. Unit Cell Packed Bed.

To save computational time, the unit cell model is utilized. The flow characteristics within this hexagonal cut out would be the same throughout the body. By designating the conditions on the outside of the cell as a "symmetry plane," the unit cell model mimics the results of the entire whole-body model at a fraction of the run time. The symmetry plane characteristics are discussed later. Using the unit cell method expedites refinement process and allows for a viable set of initial conditions to be determined prior to running the time intensive whole-body model. The unit cell CFD model had a resulting C_v of 10.24, seen in Appendix B.

To run this CFX project, the selection menu, numerical settings, and other options are seen in Appendix C. Running CFX Projects begins by importing the geometry which is first saved as a Parasolid (.x_t) through SolidWorks Once the import is completed, the next step is to generate a mesh. The mesh is comprised of numerous pyramid and cubic elements. Each mesh cell contains its own boundary conditions and derives its input data from the adjacent mesh cell's output. The initial mesh generated is seen in Figure 36.

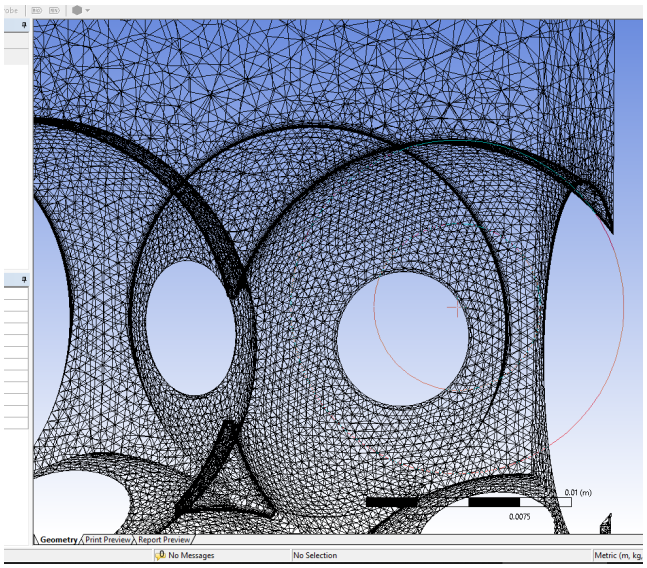

Figure 36. Generating Initial Mesh.

Afterwards, an inflation layer is added to the walls. The purpose of the inflation layer is for the program to create a layer of cubic mesh element at the designated walls that are better aligned to the boundary layer flow field and that are sized appropriately to result in a low Y+ value in the simulation. In fluid mechanics, Y+ is a non-dimensional parameter that is indicative of where shear stress is measured within the flow surface. Those layers in these models are extremely important as shear stress is proportional to the pressure drop developed.

Initial values were used from previous simulations using coarse meshes. Minimum inflation layers with small growth rates are desired for more precise calculations. This initial run was completed as a calibration run to gather information for future iterations. Convergence results were imprecise but accepted to continue.

Once the layers were constructed, named selections are designated on the model. These named selections designate what function each face of the model is for. The inlet for this model is placed on the top face while the outlet is placed at the bottom face, directly opposite from the inlet.

The surface names simplify the future steps of the simulation. Workbench's recognition helps the user designate the specific boundary conditions relative to the type

of surface the flow will interact with. Walls are designated with a “no slip” condition, referring to the fluid being stationary at the surface, acting as an expected wall would. The symmetry faces subject to zero gradient conditions. This sets the conditions of the space on the inside of the symmetry face equal to the outside of the face creating a simplified whole-body calculation. As mentioned earlier, the results within this hexagonal shaped spaced would be the same as any other hexagonal shaped cell in the entire body. With this completed and updated, the next step in running CFX is to set up the run.

The setup phase, CFX Pre, begins with designating the domain, in this case, liquid water at standard atmospheric temperature and pressure. After clicking on the default domain tab the characteristics of the fluid measured and the surrounding environment are designated.

Following the previous steps, named selections must be added again. The addition of the named selections in this process allows the respective boundary conditions to be designated. Due to the naming structure described above, typing in the designated names such as Inlet, Outlet, Wall, or Sym into the naming entry allows default settings to be applied and adjusted, saving time in manually inputting settings. Symmetry settings do not need to be adjusted as explained prior. All settings can be seen again in Appendix C. After Named Selections are finished, the solver parameters must be set.

The turbulence numeric option of First Order is desired in this situation for faster and more stable run times. More precise numeric options can be utilized for better results at the cost of processing hours. As the purpose of these simulations were for preliminary scoping to move forward with production, lower fidelity options were adequate. Concluding the setup is the insertion of monitoring points. Monitoring points instruct CFX to derive the conditions at specified locations, use the conditions in specified calculations, and deliver a simplified result.

The first monitoring point instructs CFX to take the differential pressure felt at the inlet and outlet and calculate in psi. The second monitor point inputs the calculated inlet volumetric flow rate, differential pressure from the first equation point, and uses Equation 5 to calculate the simulated value of C_v.

After concluding the setup processes, the solver is initiated through the solution tab on the main screen. The option of double precision is selected to allow for more precise calculations. Double precision option designates CFX to run the calculations using 32 bits instead of 16. The large problem option notifies CFX of a large simulation, allowing the processes to be completed using parallel partitions. Using parallel partitions allows CFX to run calculations simultaneously using separate processers, compared to serial where CFX utilizes all the processors to solve the simulation sequentially. Afterwards, the desired processor can be designated, and the number of cores can be allotted in the partition's selection. Once initialized, the outputs are seen in Appendix . The initial runs were done to minimize Y+ and determine a baseline mesh size. The k-epsilon turbulence model that is used in this simulation delivers more accurate results when the Y+ is below 30. By taking the Y+ calculated in the initial run, determining how many multiples were required to reach a desired Y+ of 30 or less, the initial inflation layer size is then divided by the same number to reach a new inflation layer. The first iterations were done to establish a nominal mesh size, and a starting mesh of 0.5 mm is generated, utilizing 600,574 nodes and 1,667,922 elements resulted in a very coarse result, with a Y+ of > 200 in most places.

Refining the mesh to 0.1 mm at the wall, resulted in over 2,000,000 nodes and 8,500,000 elements, resulted in similar results but the price of more than tripling the runtime. Increasing the mesh size to a 1.0 mm caused the model to reach convergence faster with similar results. Continuing with a wall 1.0 mm mesh was decided upon to minimize processing time. Reduction of the inflation layer was done by a factor of 11.875. The resolved mesh is seen in Figure 37.

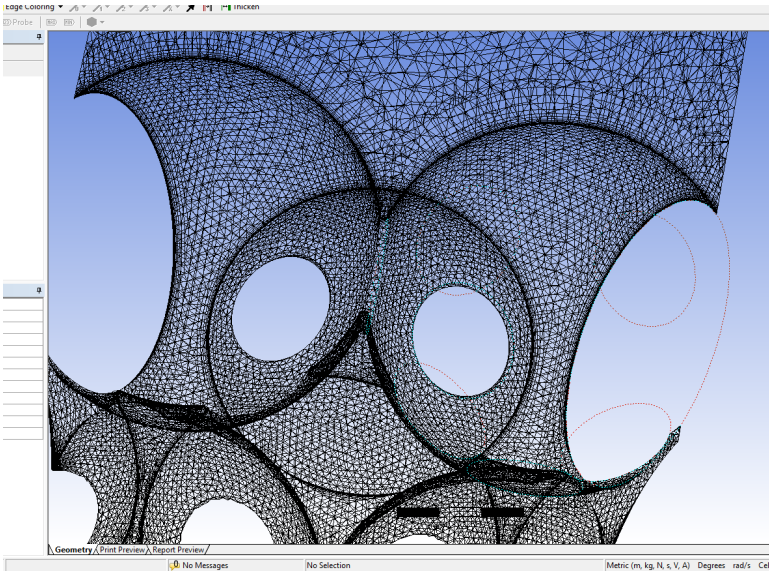

Figure 37. Resolved Mesh.

This resulted in Y+ values at less than 5 across the model seen in Figure 38. Figure 39 illustrates the overall pressure gradient seen in the unit-cell model.

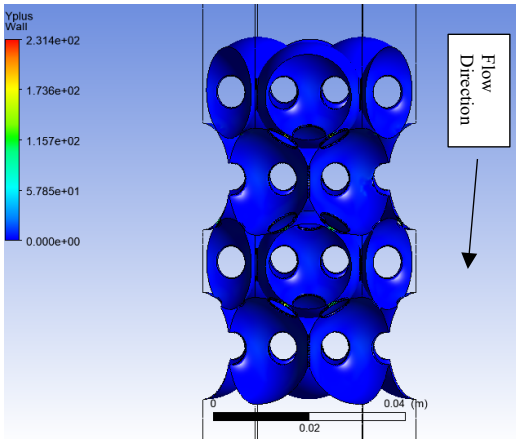

Figure 38. Resolved Mesh Y+

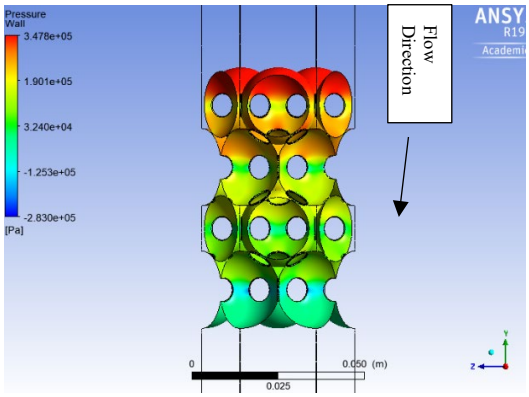

Figure 39. Pressure Gradient

The pressure gradient shows both continuity and the desired stagnation points as expected. The pressure drop is higher than predicted by the analytical models. Over the entire model, the ΔP is 347.77 kPa (50.44 Psi), a 29.6% increase from what was analytically predicted. The C_v of 12.2, is 19.1% higher than expected. Possible differences stem from the inclusion of fillets between each sphere. The Packed Bed calculations relied on unconnected spheres resulting in a wider channel for flow, resulting in less head loss compared to the actual cells. Once the unit cell model provided initial mesh configurations, the full model referenced in Figure 32, was run utilizing a 1.0 mm mesh to streamline runtime. The settings were maintained as the whole body is the expansion of the unit cell in the radial direction. Mechanics for pressure drop remain the same and similar results should be achieved as pressure remains relatively constant throughout the radial direction of any component.

The mesh of the overall model is ~18,500,000 nodes and ~44,000,000 elements. The final model's resulting C_v was a value of 10.12, an error of 28.8%. This model however was never able to converge possibly due to the actual flow field having transient characteristics. Further refinement of the mesh required more processing power than what was available in the hardware. As this was a preliminary study of a whole-body model, the results were adequate to begin physical production. The final pressure gradient can be seen in Figure 40. The turbulence is developed as flow is forced to enter the channels, reaching the maximum in the middle of the channels. The turbulence is then dissipated once the

channels begin to expand, seen in Figure 41. This mechanism for overall energy dissipation contributes to pressure loss.

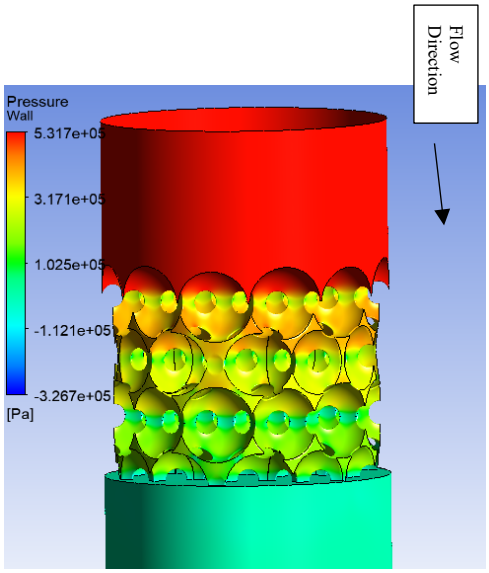

Figure 40. Overall Packed Bed Pressure Loss

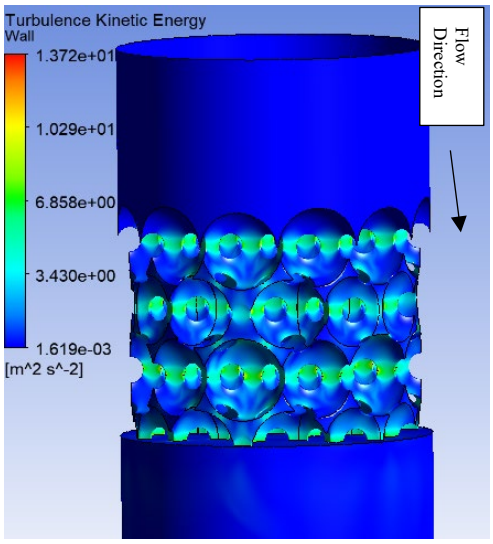

Figure 41. Overall Packed Bed Turbulence Kinetic Energy

2. Helical

The Helical Model simulation was less resource intensive to run than the Packed Bed. An initial mesh generation of 1.0 mm was used, similar to the Packed Bed, but produced bad convergence results. Further refining past 0.1 mm yielded the same

convergence patterns seen in Appendix F. Data from a mesh of 0.5 mm was utilized and the final Y+ numbers were less than 30 at each point. The final number of nodes was ~8,500,000 and the number of elements was ~20,000,000.

The numerical prediction of the helical channel's pressure loss coefficient, C_v, was a value of 9.21, an error of 6.2%. The Helical showed a much more gradual gradient than for the packed bed geometry which was expected. As there is only one area of constriction, the velocity spike and associated turbulence can be seen at the entrance. The pressure gradually reducing over the coils can be contributed to the consistent direction change and the friction from within the cylinders. The pressure gradient can be seen in Figure 42 and the Turbulence Kinetic Energy can be seen in Figure 43.

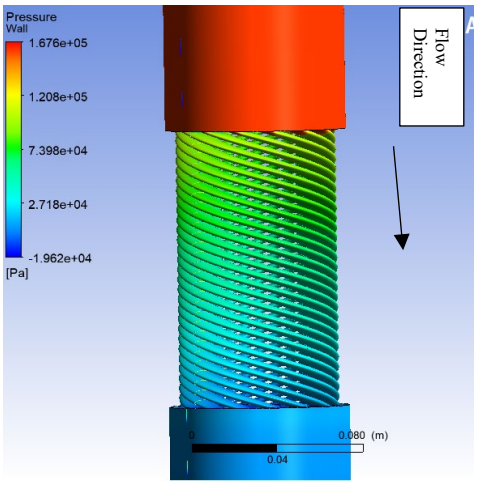

Figure 42. Helical Model Pressure Gradient

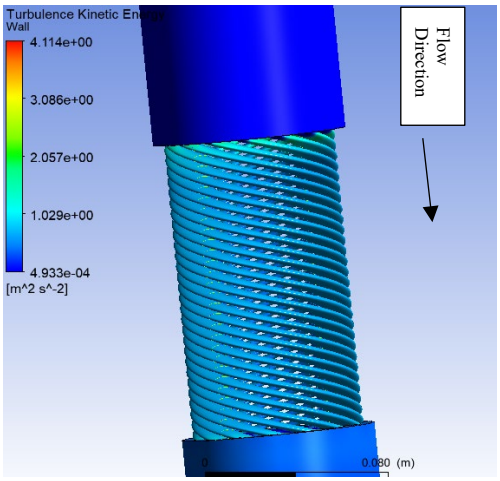

Figure 43. Helical Model Turbulence Kinetic Energy

The sudden increase in velocity at the entrance also resulted in a slight redesign where the initial entrance's walls are made thicker to account for a higher stress at that location.

The un-converged residuals seen in Appendix F are due to the model calculations based on steady state flow. The residuals seen in Figure 44 illustrate that the flow in this field is not steady but rather pulses.

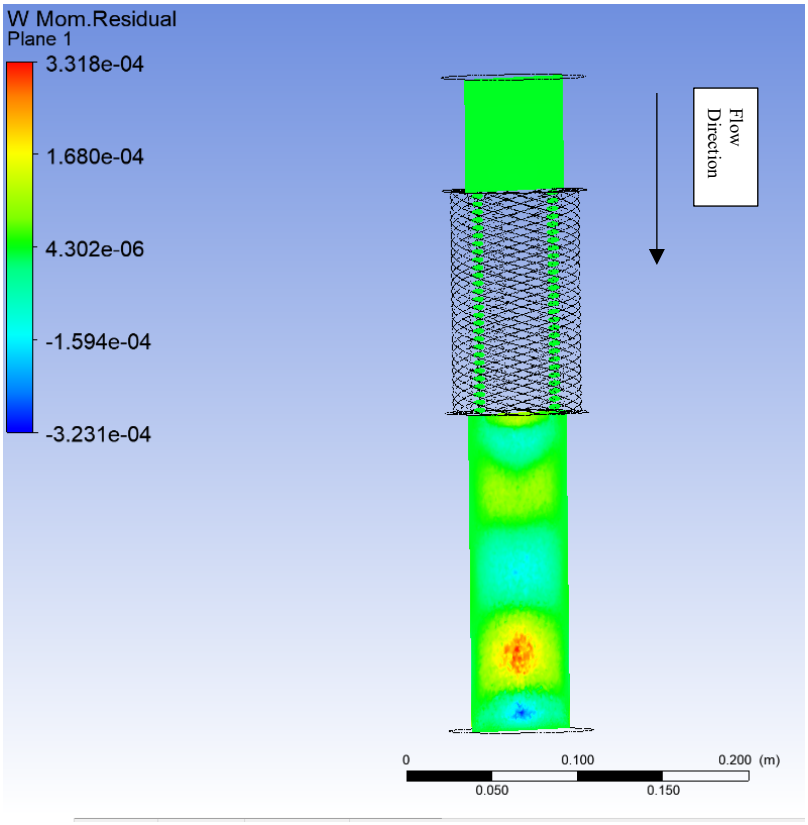

Figure 44. Pulsing Flow Residuals.

A flow exiting a channel at an acute angle instead exiting parallel to flow direction centerline causes a miniature vortex that requires time to develop steady behavior. As there are many of these vortexes due to the numerous exit channels, a steady behavior was not observed. Outlet velocities and resulting pressure differences, are seen to have a pulsing behavior. If a real time video were developed, the red area of lower convergence would begin at the exit of the channels and continue to travel down the flow direction. The residuals observed within the channels themselves were two degrees of convergence more precise than the outlet. As these runs were completed for a preliminary study, they were adequate in predicting average pressure loss. Additionally, the pulsing behavior will produce excess vibrations which is not ideal for the application.

THIS PAGE INTENTIONALLY LEFT BLANK

V. CONCLUSION AND FUTURE WORK

A. CONCLUSION

Additive Manufacturing proved a viable way to produce pressure drop component replacements. Current components suffer from vibration and require excess fabrication and machining. The production of the Packed Bed model highlighted the ability to manufacture an extremely complex geometry successfully. The Packed Bed model proved successful in its ability to create head loss in a flow loop, performing 28.8% better computationally than analytical results. The Helical model's production was also successful, highlighting the ability to produce a design without excess support requirements. The Helical performed as expected for pressure loss with a 6.2% difference in computational and analytical calculations. However, the Helical model is not viable at this point due to the pulsing vibrational concerns. Slight adjustments at the model's outlet are hypothesized to alleviate most of the pulsing seen.

B. FUTURE WORK

1. Complete Test Loop

The loop construction process began with equipment that would not be electrically safe to connect to the facilities. A redesign was required, with a new motor and VFD being ordered. Delays in shipping resulted in the final construction being incomplete. Future work will consist of connecting the designed motor and VFD and testing the integrity of the loop.

2. Model Refinement

a. Pebble Bed

The Pebble Bed's CFX runs were limited by the amount of processing power and time. Though convergence was acceptable for a preliminary study, future work will have additional processors to evaluate the model using higher fidelity numeric options. Different fluid transport models will also be used to evaluate different results.

b. Helical

The Helical Model's CFX were run under the steady state condition, resulting in residuals that were unable to converge. Future work, if investigating this component, will be developing a CFX model with appropriate time dependent conditions to achieve better convergence results. This component causes too much vibration as it stands. A redesign of its outlets for a straight exit may alleviate the vortex phenomenon and the pulsing behavior.

3. PIV

Initially, this project was designed to incorporate Particle Image Velocimetry (PIV) to investigate the flow. PIV utilizes laser interrogation of a fluid in which particles or seeds are suspended. The different positions of the seeds observed with respect to time measured through the laser's frequency can be interpolated into a velocity. PIV would have allowed not only velocity measurements in which pressure can be derived, but also a visual representation of turbulence within the system [24]. The constructed loop already utilizes a clear acrylic test section, housed in an acrylic box filled with water. The laser enters the box's surface, the housing water, and then the test tube which reverts the index of refraction back to 1 which allows for undistorted measurements. Figure 45 shows a simplified operation of PIV.

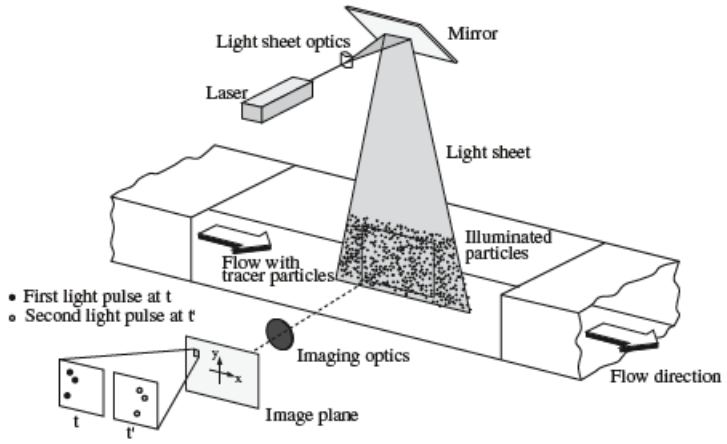

Figure 45. PIV Operation

APPENDIX A. PACKED BED MODEL CALCULATIONS

These calculations are the initial calculations determining the loss coefficient, C_v, for the Packed Bed Model.

$rho := 1000 \frac{kg}{m^3}$ $d := .875\ in$ $Space := .85\ in$ $V := 1 \frac{m}{s}$ $pi := 3.14\ rad$ $L := d \cdot 4$

$mu := 0.001 \frac{kg}{m\ s}$ $A := \left(\frac{3.325\ in}{2}\right)^2 \cdot pi = 0.0056\ m^2$ $theta := 60\ deg$

$Q := A \cdot V = 88.748 \frac{gal}{min}$

$$Void := \frac{pi}{6 \cdot (1 - \cos(theta)) \cdot \sqrt{1 + 2 \cdot \cos(theta)}} = 0.7401$$

$v := 1.0035 \cdot 10^{-6} \frac{m^2}{s}$

$Void_Frac := 1 - Void = 0.2599$

$$Re_d := \frac{\frac{0.45}{(1 - Void_Frac) \cdot \sqrt{Void_Frac}} \cdot V \cdot d}{v} = 26414.636$$

$$lambda := \frac{30}{Re_d} + \frac{3}{Re_d^{0.7}} + 0.3 = 0.3035$$

$$k := \frac{1.54}{Void_Frac^{4.2}} = 441.9469$$

$$Loss := k \cdot lambda \cdot \frac{L}{d} = 536.6026$$

$Delta_P := rho \cdot \frac{V^2}{2} \cdot Loss = 2.683 \cdot 10^5\ Pa$

$$C_v := \frac{Q}{\frac{(gal)}{min}} \cdot \left(\frac{1}{\frac{Delta_P}{psi}}\right)^{.5} = 14.2268$$

$Delta_P = 38.9138\ psi$

THIS PAGE INTENTIONALLY LEFT BLANK

APPENDIX B. PACKED BED INITIAL CFD CALCULATIONS

These calculations are the initial calculations determining the loss coefficient, C_v, for the unit-cell version of the Packed Bed Model. Changes were required to account for less flow area, decreasing volumetric flow rate.

$rho := 1000 \frac{kg}{m^3}$ $d := .875\ in$ $Space := .85\ in$ $V := 1 \frac{m}{s}$ $pi := 3.14\ rad$ $L := d \cdot 4$

$mu := 0.001 \frac{kg}{m\,s}$ $A := \frac{d^2}{2} \cdot 3 \cdot (\sqrt{3}) \cdot pi = 0.004\ m^2$ $theta := 60\ deg$

$Q := A \cdot V = 63.8709 \frac{gal}{min}$

$Void := \frac{pi}{6 \cdot (1 - \cos(theta)) \cdot \sqrt{1 + 2 \cdot \cos(theta)}} = 0.7401$ $v := 1.0035 \cdot 10^{-6} \frac{m^2}{s}$

$Void_Frac := 1 - Void = 0.2599$

$Re_d := \frac{\frac{0.45}{(1 - Void_Frac) \cdot \sqrt{Void_Frac}} \cdot V \cdot d}{v} = 26414.636$

$lambda := \frac{30}{Re_d} + \frac{3}{Re_d^{0.7}} + 0.3 = 0.3035$ $k := \frac{1.54}{Void_Frac^{4.2}} = 441.9469$

$Loss := k \cdot lambda \cdot \frac{L}{d} = 536.6026$

$Delta_P := rho \cdot \frac{V^2}{2} \cdot Loss = 2.683 \cdot 10^5\ Pa$ $C_v := \frac{Q}{\frac{(gal)}{min}} \cdot \left(\frac{1}{\frac{Delta_P}{psi}} \right)^{.5} = 10.2389$

$Delta_P = 38.9138\ psi$

THIS PAGE INTENTIONALLY LEFT BLANK

APPENDIX C. CFX PROCESS

These figures show the menus and selections for running ANSYS CFX. Additionally, these figures also show the numerical settings and options for each step.

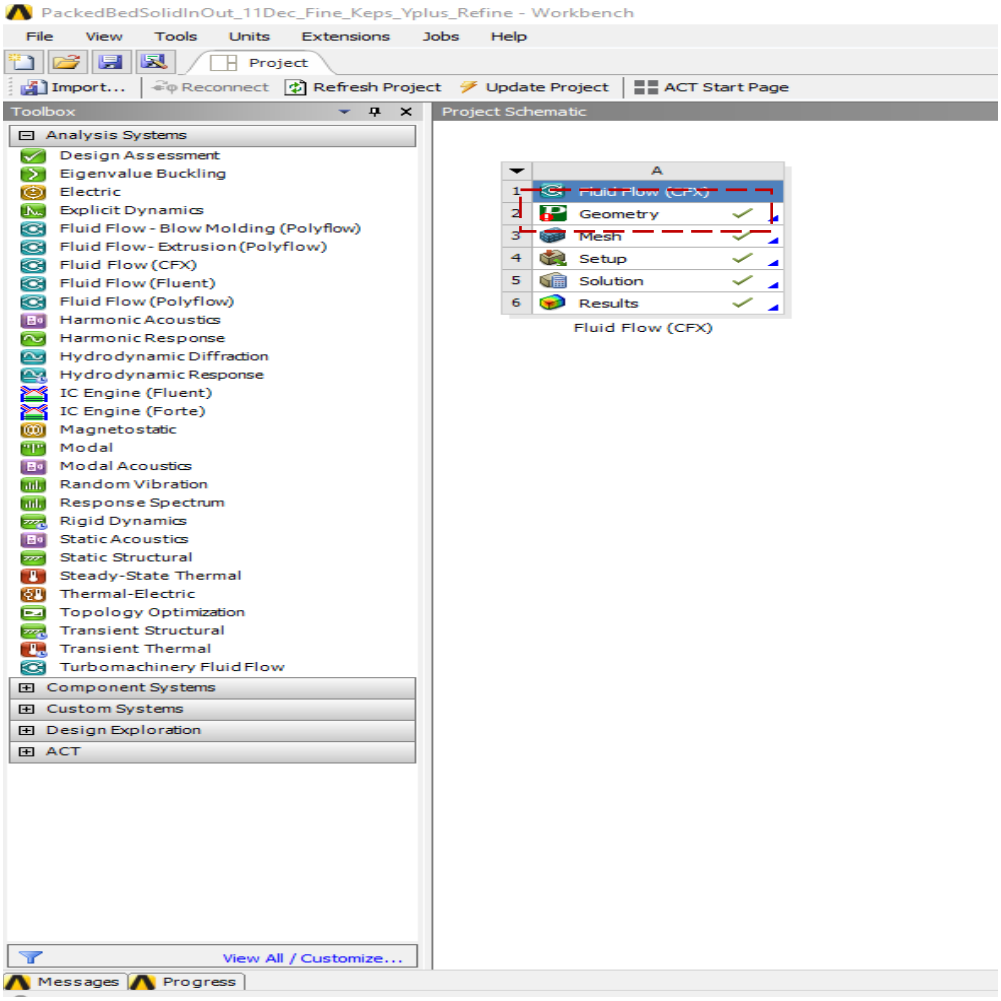

Figure C1. ANSYS CFX Main Menu with Geometry Selection.

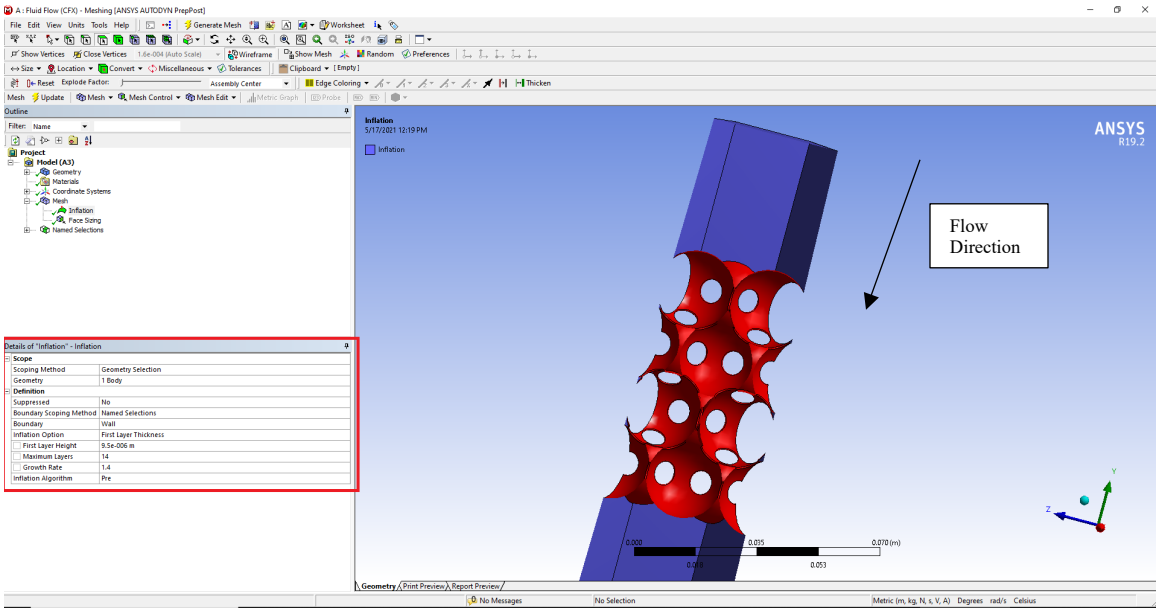

Figure C2. Initial Inflation Layer Selection.

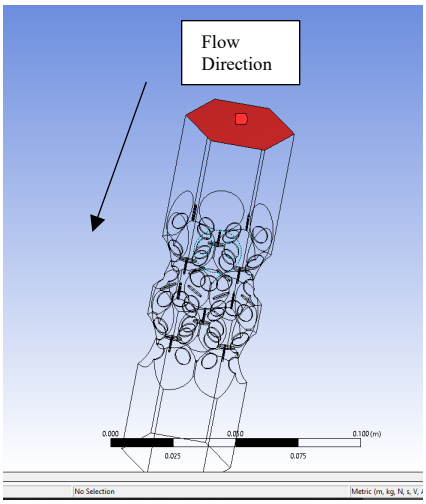

Figure C3. Named Selection – Inlet.

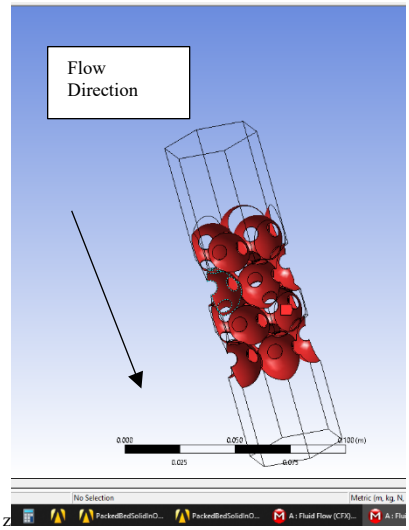

Figure C4. Named Selection - Wall.

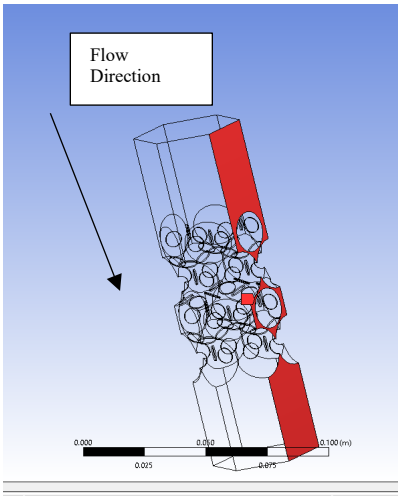

Figure C5. Named Selection - Symmetry.

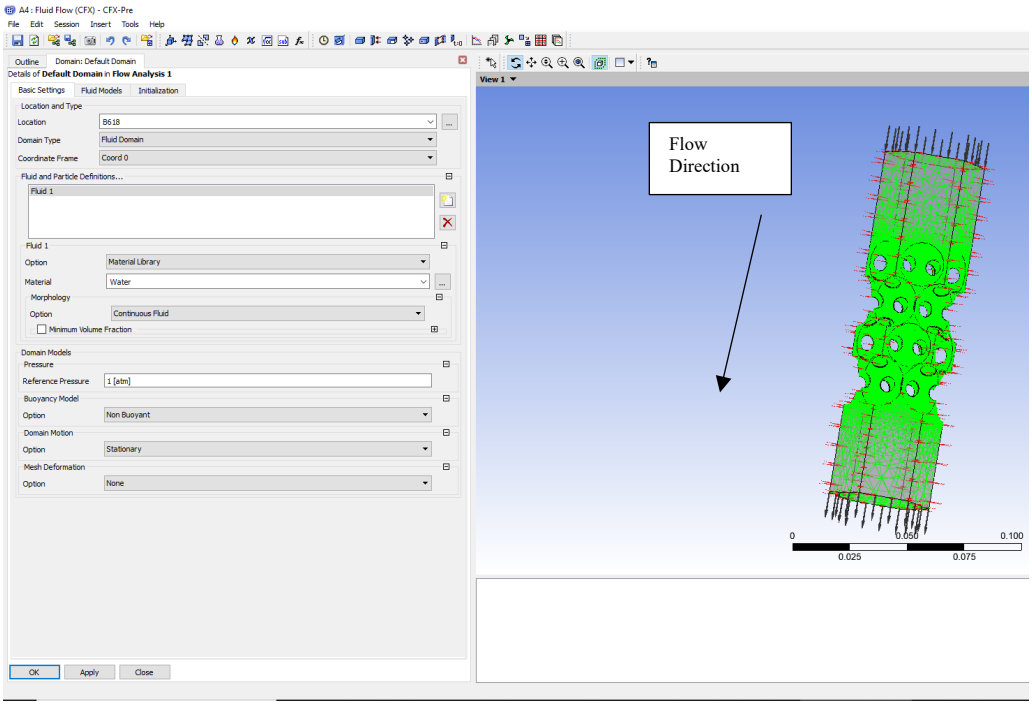

Figure C6. Default Domain Selection.

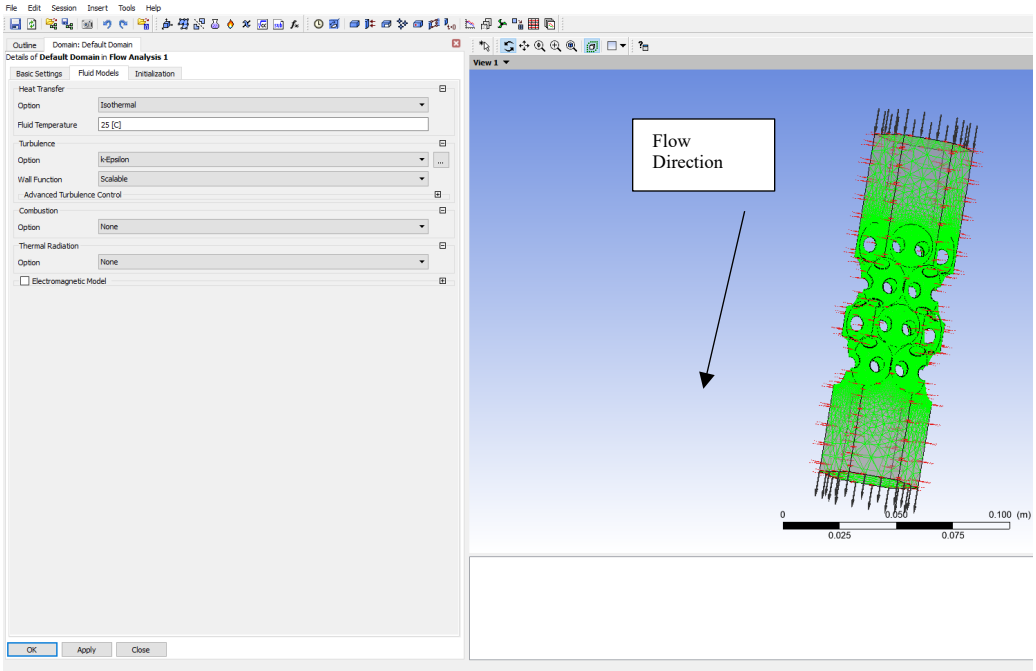

Figure C7. Fluid Models Selection.

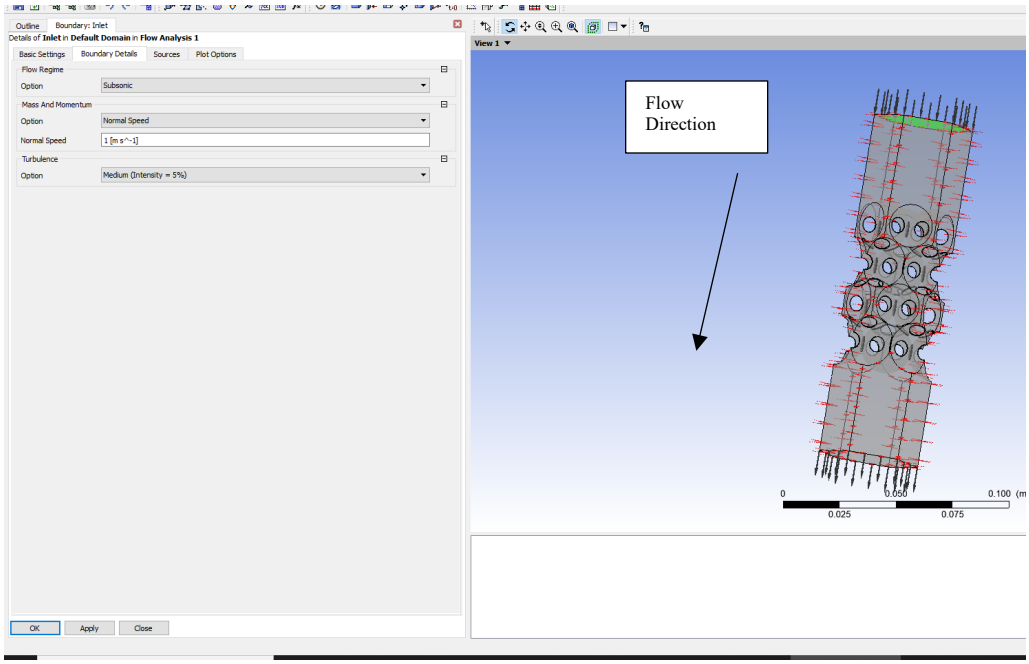

Figure C8. Inlet Conditions

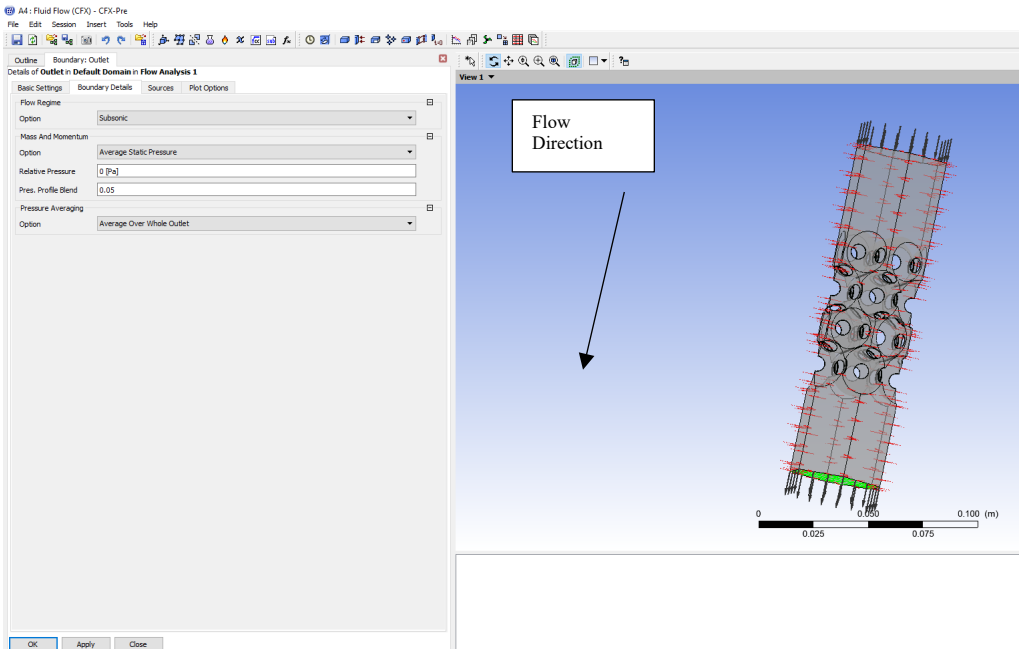

Figure C9. Outlet Conditions.

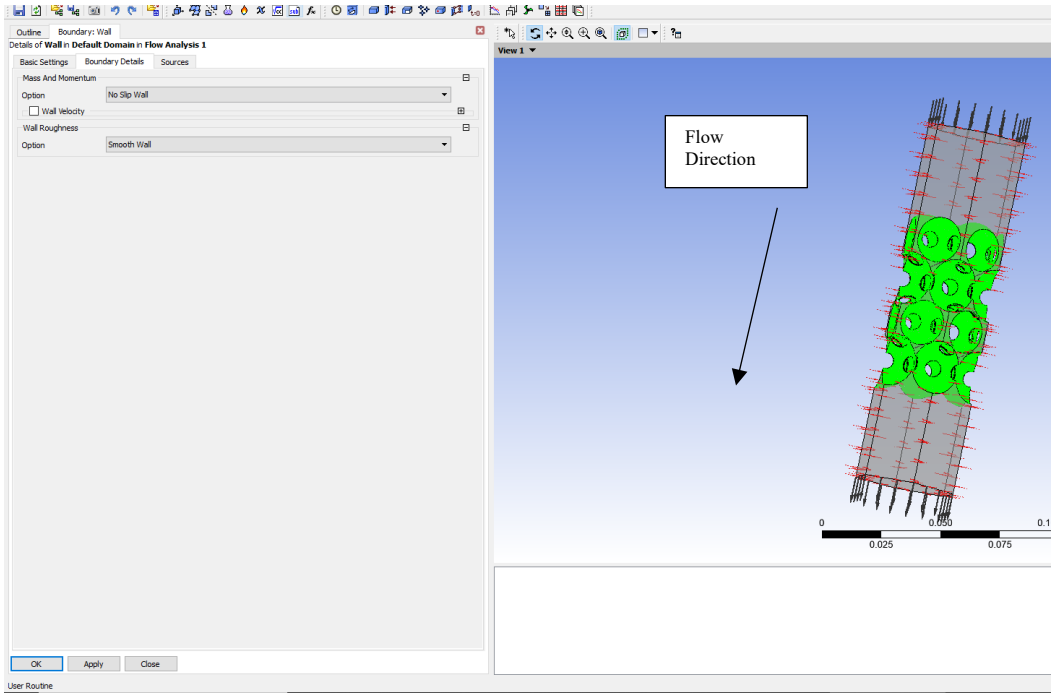

Figure C10. Wall Conditions.

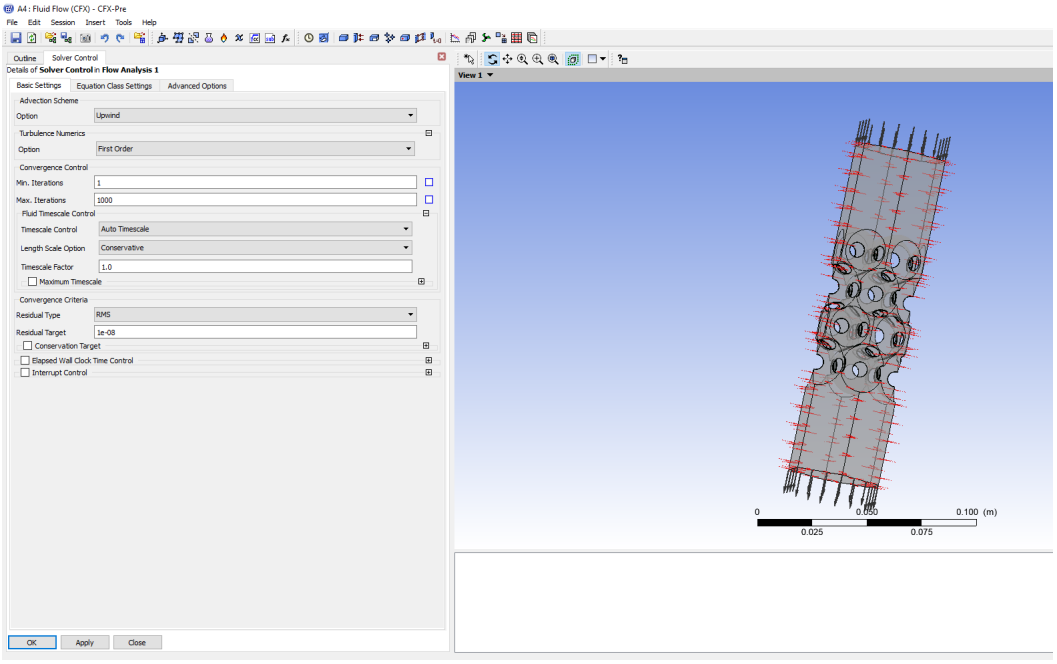

Figure C11. Solver Control Parameters.

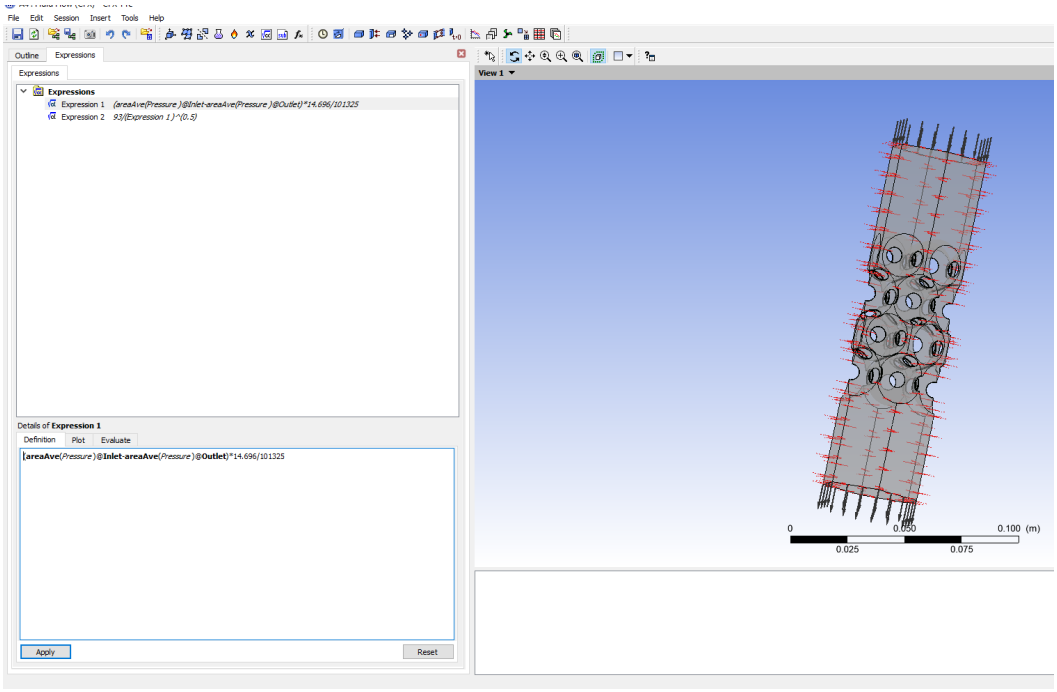

Figure C12. Monitor Point Designation.

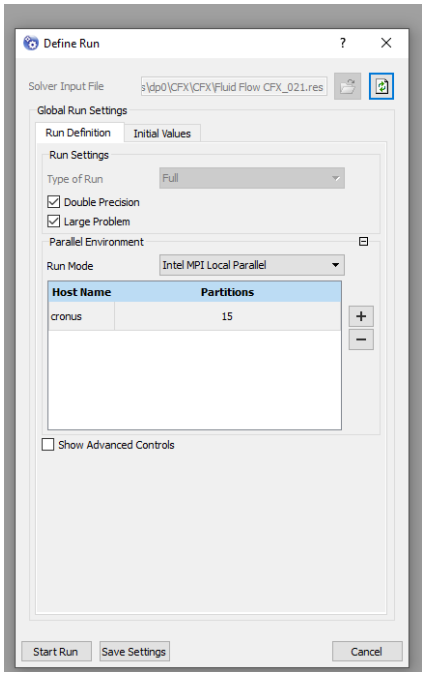

Figure C13. Solver Initialization Conditions.

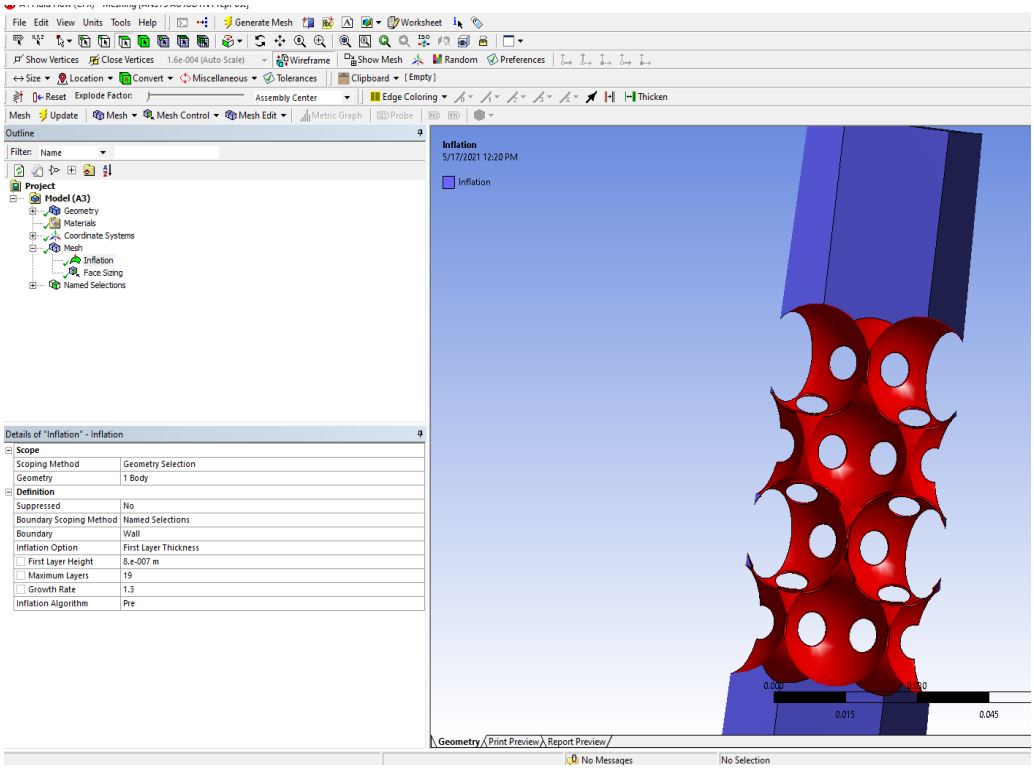

Figure C14. Resolved Inflation Layer Settings

APPENDIX D. PACKED BED MODEL CFX RESULTS

These are the convergences and monitor points for the unit-cell Packed Bed Model after initial CFX simulations.

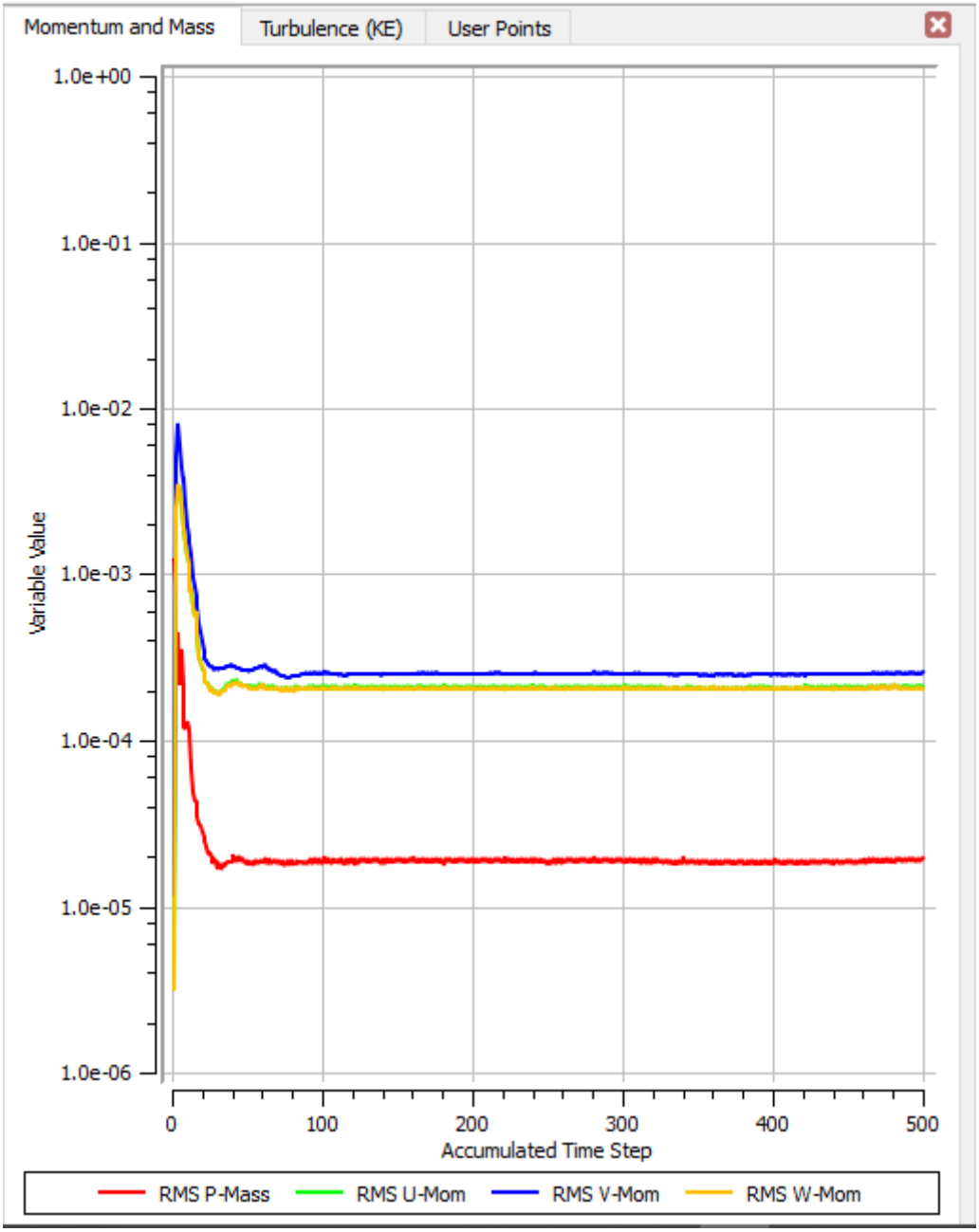

Figure D1. Unit-Cell Mass and Momentum Convergence.

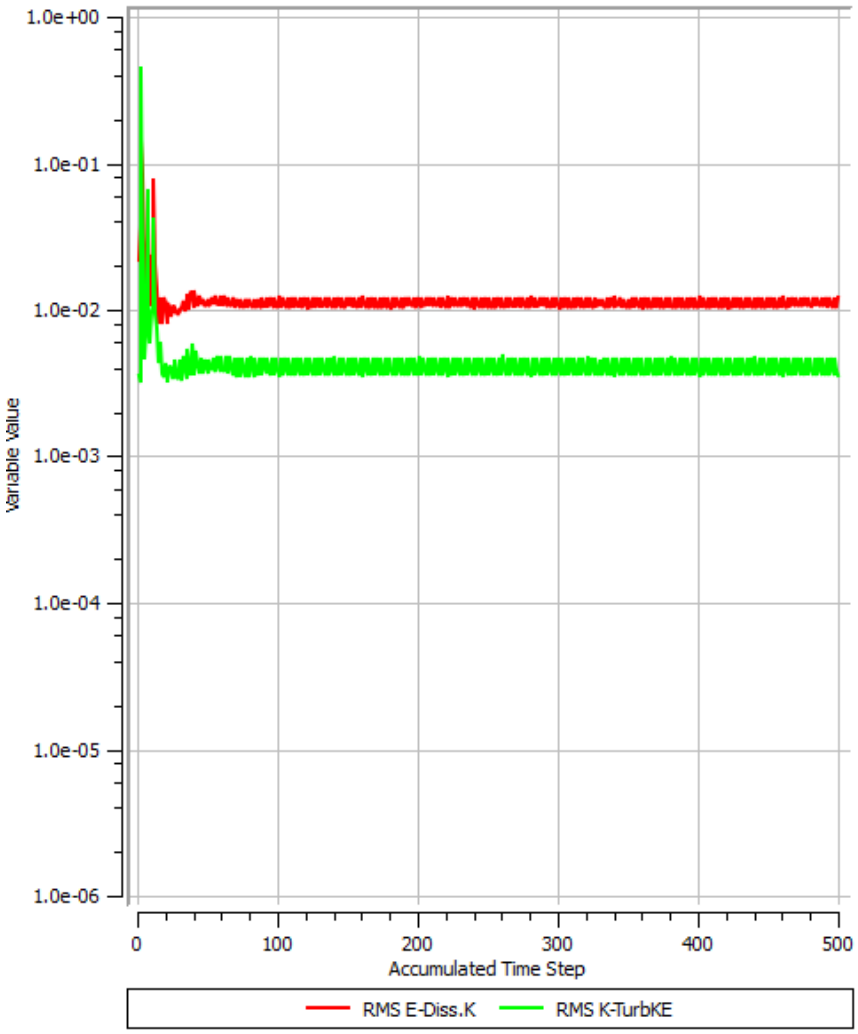

Figure D2. Unit-Cell Turbulence Convergence.

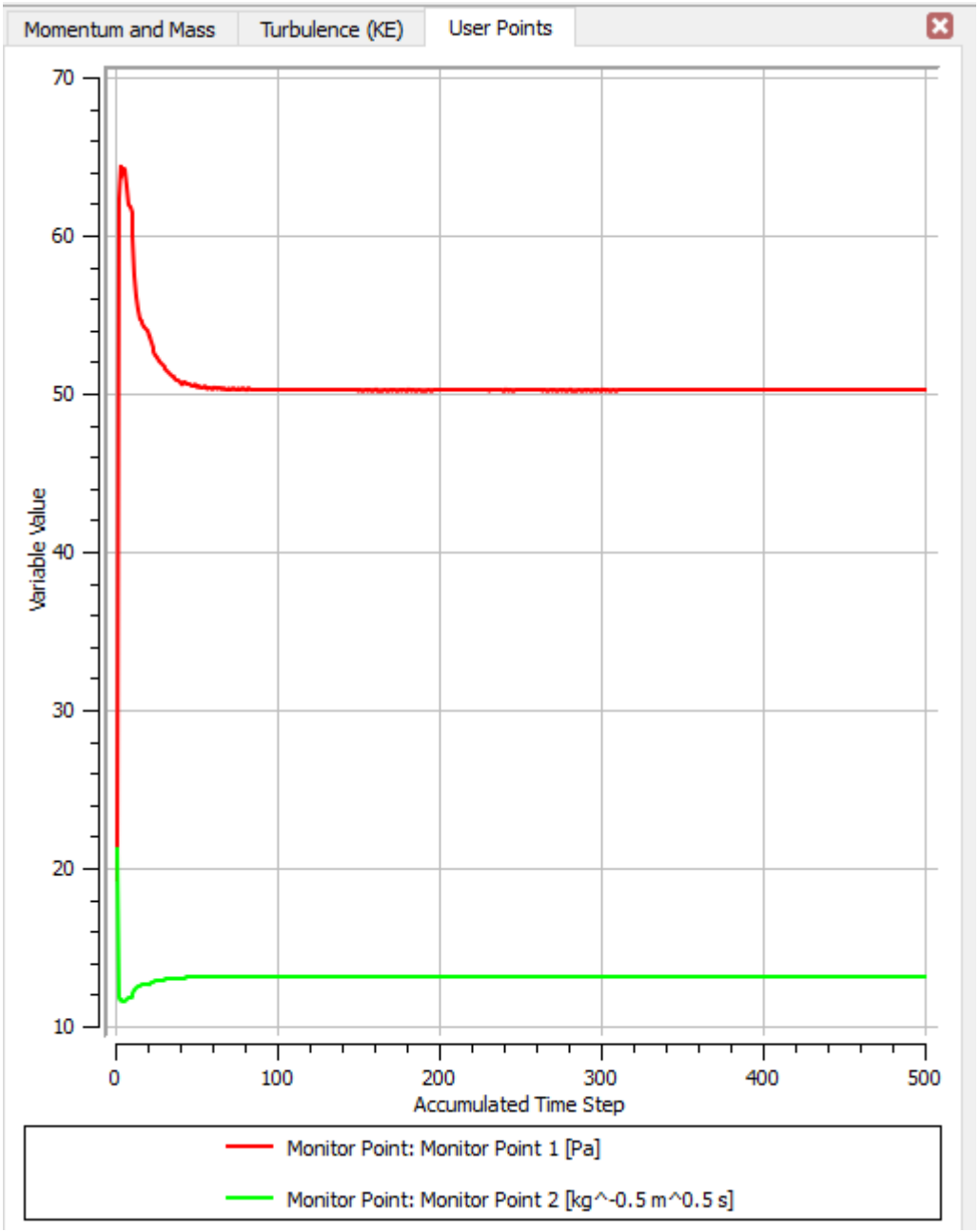

Figure D3. Unit-Cell Monitor Points. Red indicates ΔP in psi and green indicates C_v.

These figures are the convergences and monitor points for the whole body Packed Bed Model results from the CFX simulations.

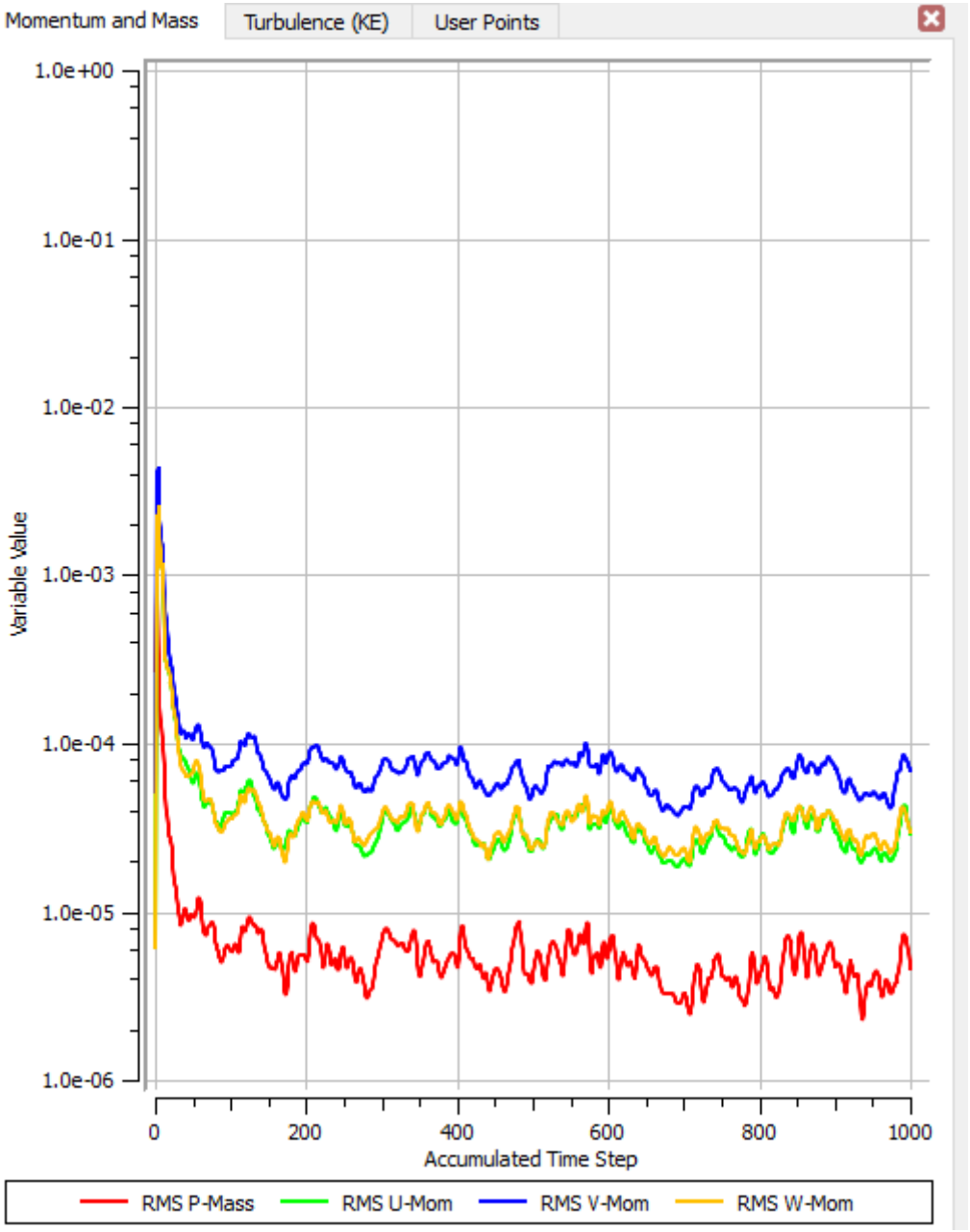

Figure D4. Whole Body Mass and Momentum Convergence.

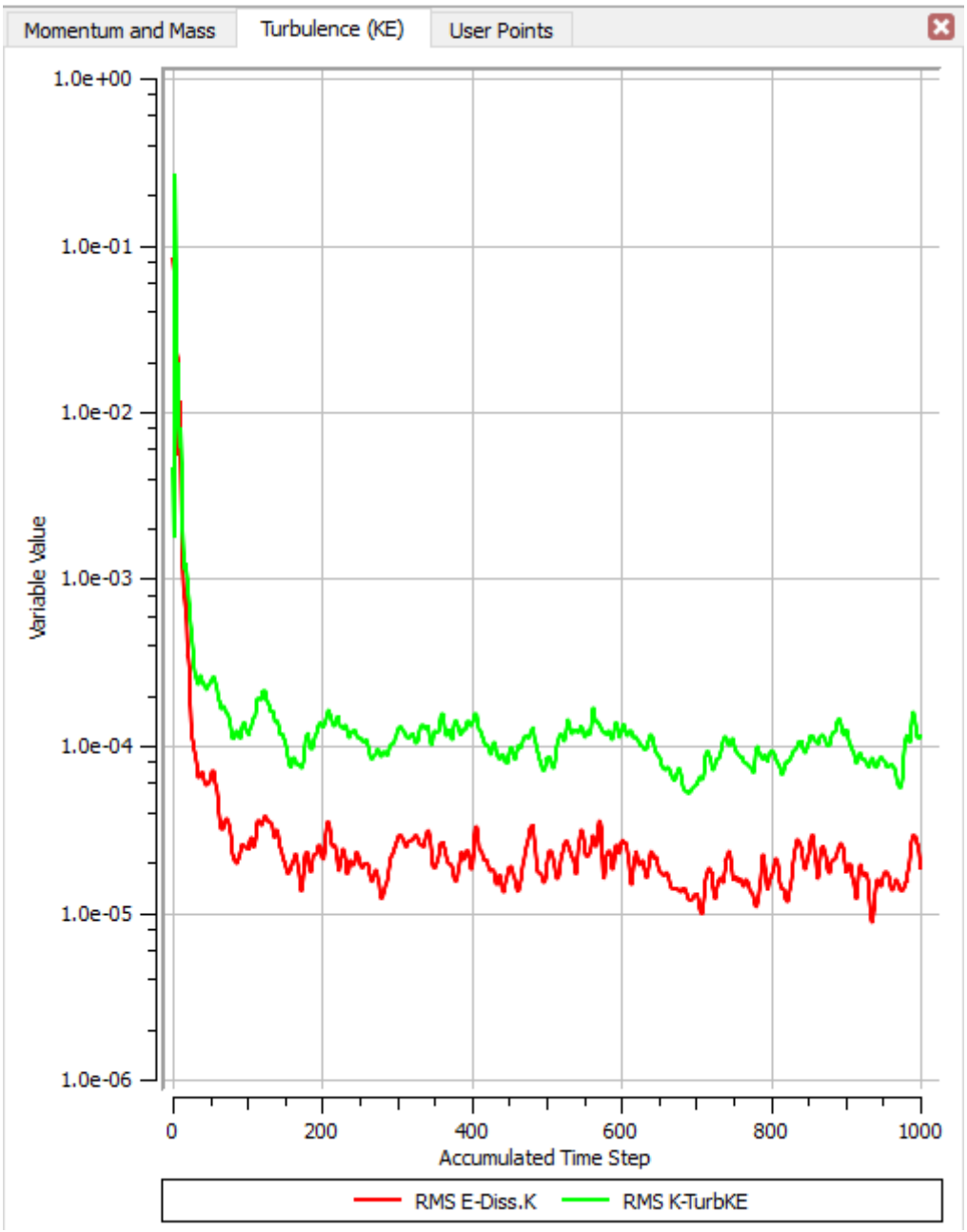

Figure D5. Whole Body Turbulence Convergence.

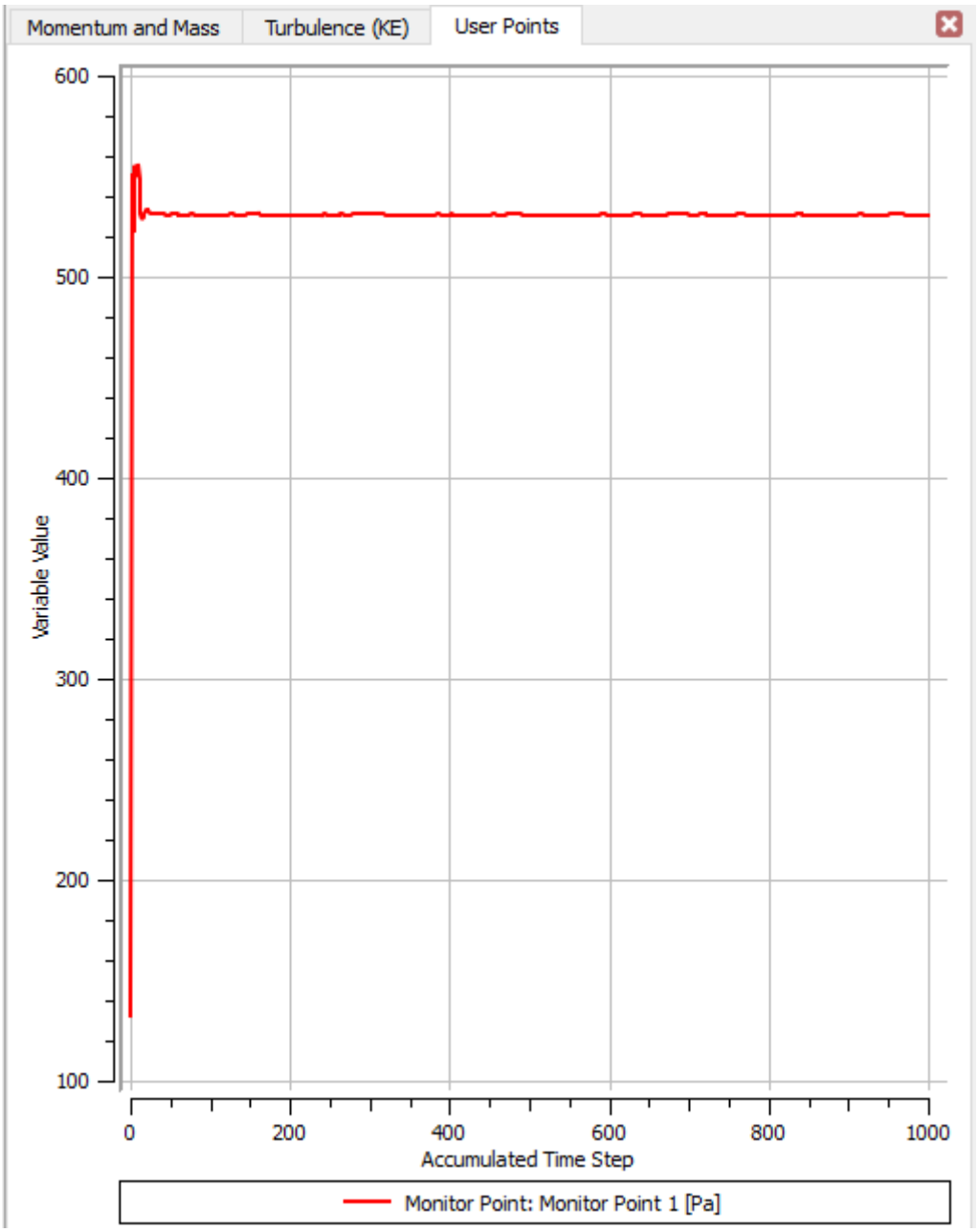

Figure D6. Whole Body Monitor Points of ΔP in kPa.

APPENDIX E. HELICAL MODEL CALCULATIONS

This is the analytical model developed for the Helical Model in order to gain the respective loss coefficient (C_v).

ENS Manjai Helical Redesign

$g := 9.81 \frac{m}{s^2}$ $pi := 3.14159$ $rho := 998 \frac{kg}{m^3}$ $mu := 8.9 \cdot 10^{-4}$ Pa s

$r_pipe := .2$ in

$d := 3.325$ in $rev := 2$ $theta := rev \cdot 360$ $n := 14$ $V := .5 \frac{m}{s}$

$r_coil := (1.275 - .2)$ in

$bend := \frac{r_coil}{2 \cdot r_pipe} = 2.6875$ $A_t := \frac{d^2}{4} \cdot pi = 0.0056\ m^2$ $A_flow := r_pipe^2 \cdot pi \cdot n = 0.0011\ m^2$

$Qin := A_t \cdot V = 44.3965 \frac{gal}{min}$

$V_pipe := \frac{A_t}{A_flow} \cdot V = 2.4678 \frac{m}{s}$

$Re := V_pipe \cdot 2 \cdot r_pipe \cdot \frac{rho}{mu} = 28115.0932$

$grade := Re \cdot \sqrt{\frac{r_pipe}{r_coil}} = 12126.9139$

$lambda := \frac{5}{Re^{0.45}} \cdot \left(\frac{r_pipe}{r_coil}\right)^{0.275} = 0.0313$

$ff := 0.0175 \cdot lambda \cdot \frac{r_coil}{2 \cdot r_pipe} \cdot theta = 1.0612$

$d_p_1 := ff \cdot 2 \cdot V_pipe^2 \cdot rho = 12.8998$ kPa

$d_p_total := n \cdot d_p_1 = 180.5973$ kPa $d_p_total = 26.1934$ psi

$C_v := \frac{Qin}{\frac{gal}{min} \cdot \left(\frac{d_p_total}{psi}\right)^{.5}} = 8.6747$

THIS PAGE INTENTIONALLY LEFT BLANK

APPENDIX F. HELICAL MODEL CFX DATA

These figures show the fluctuating convergences and the monitor points for the Helical Model's CFX simulation.

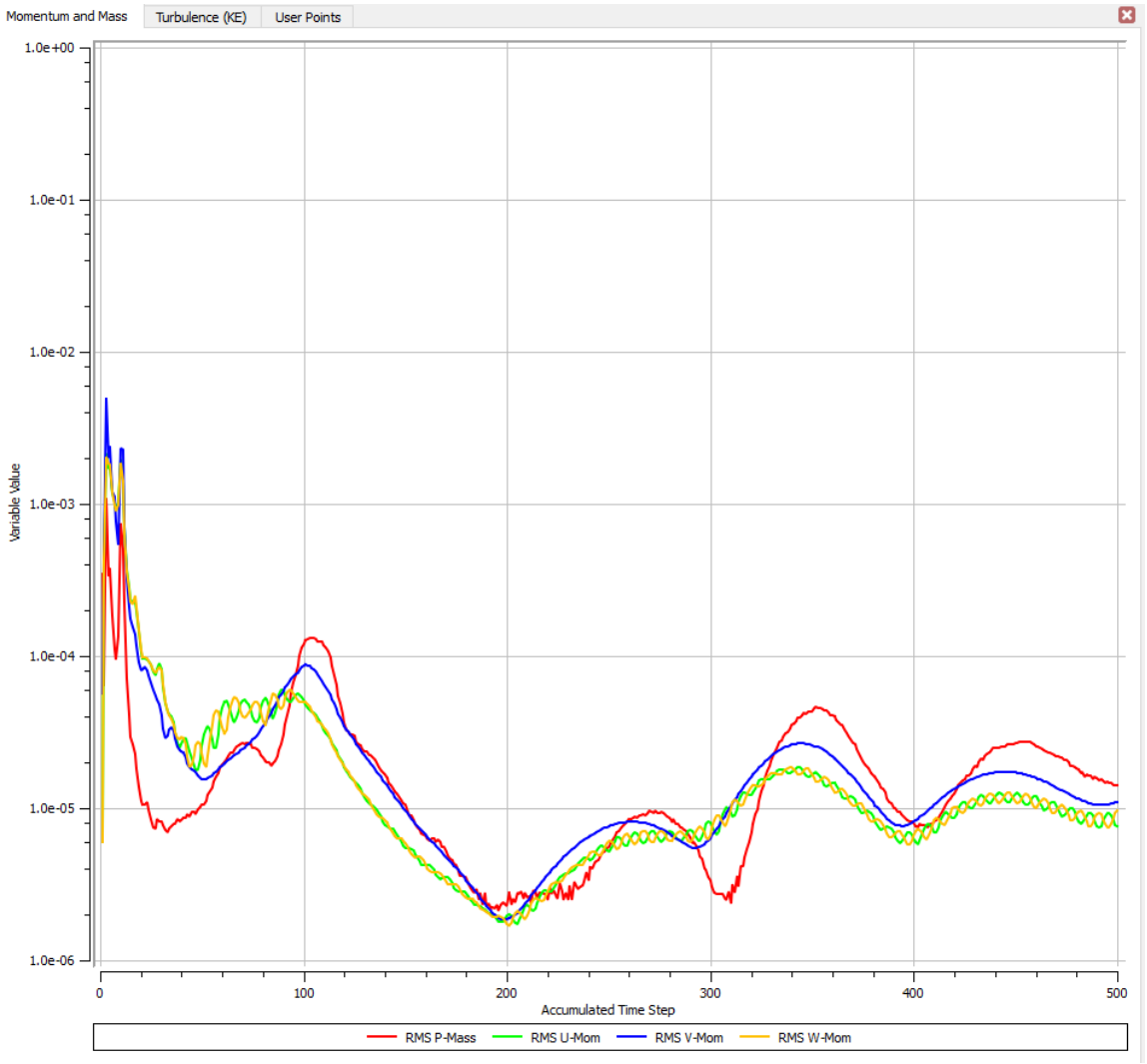

Figure F1. Mass and Momentum Convergence.

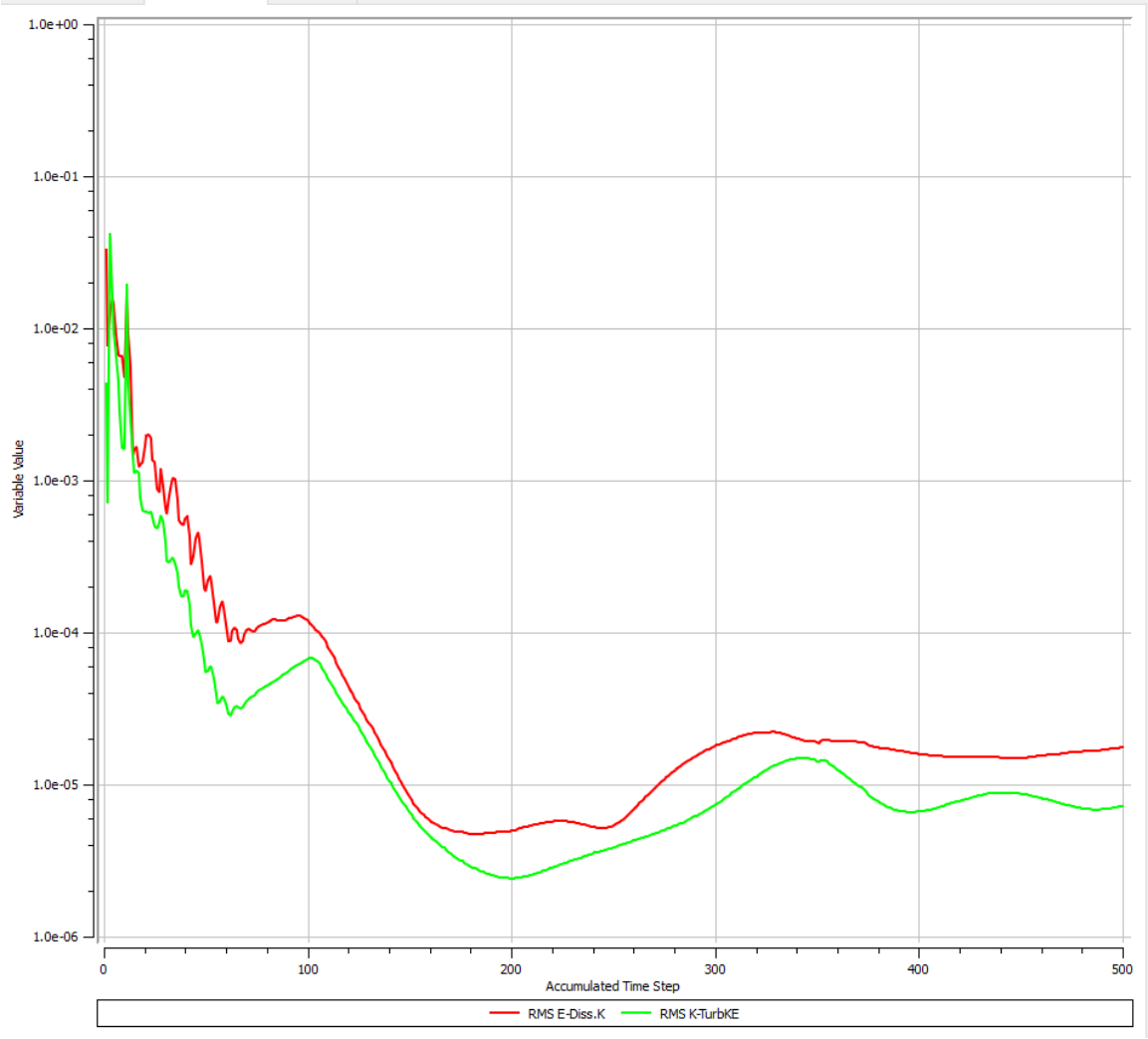

Figure F2. Turbulence Convergence.

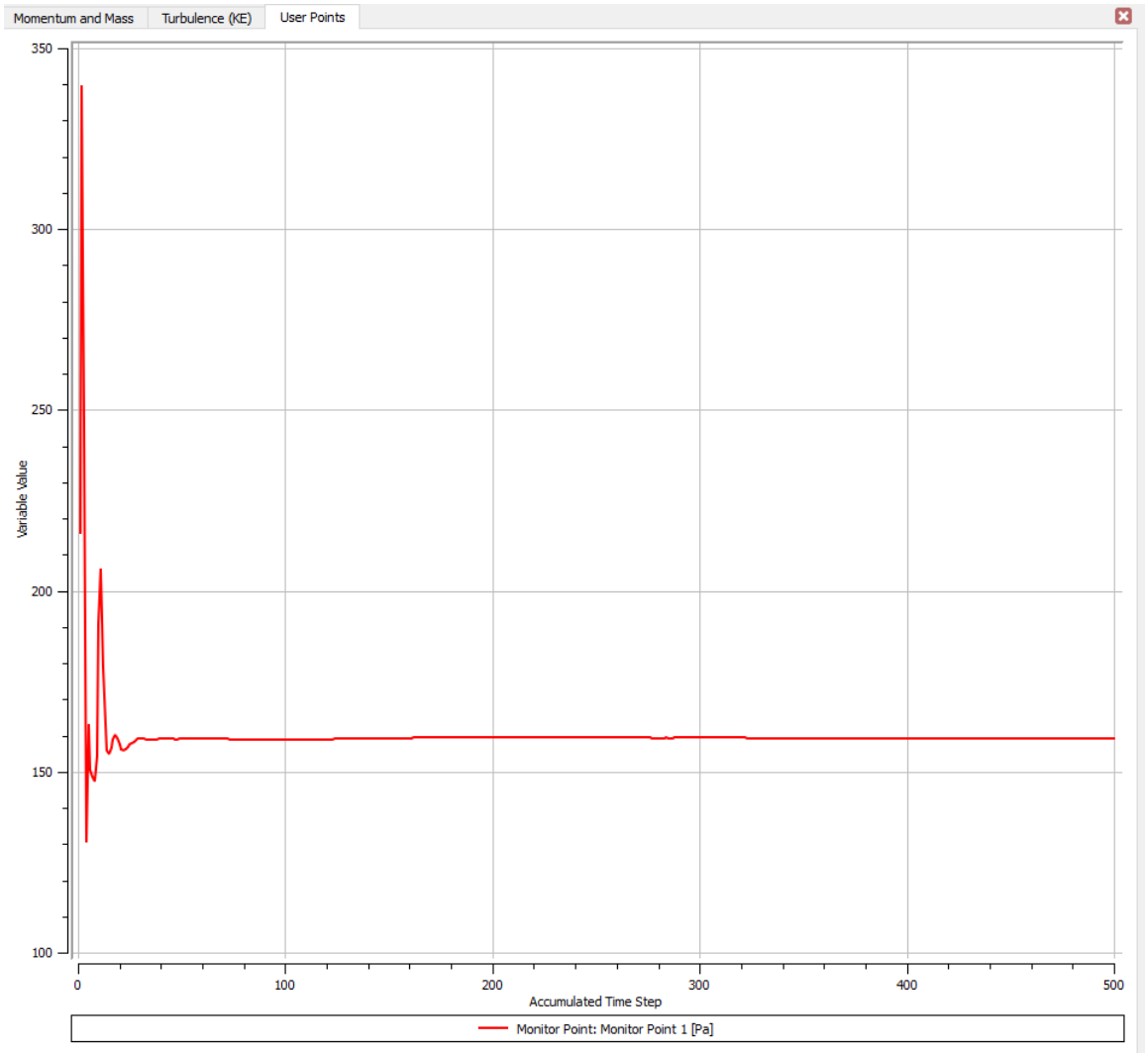

Figure F3. Monitor Points.

THIS PAGE INTENTIONALLY LEFT BLANK

APPENDIX G. ELEM-X PRINT SCANS

These figures are the in-situ scans of the Elem-X prints. These scans can be used to determine any flaws or errors during printing. Additionally, they can be combined into a 3-D computer image to highlight internal feature.

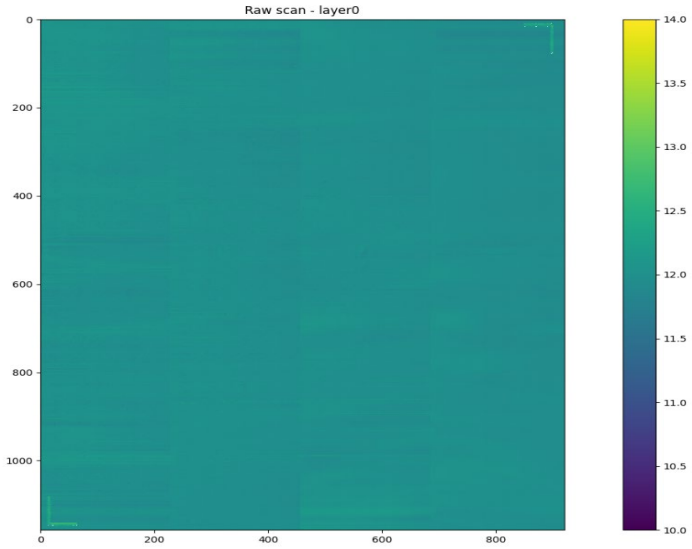

Figure G1. Initial Layer.

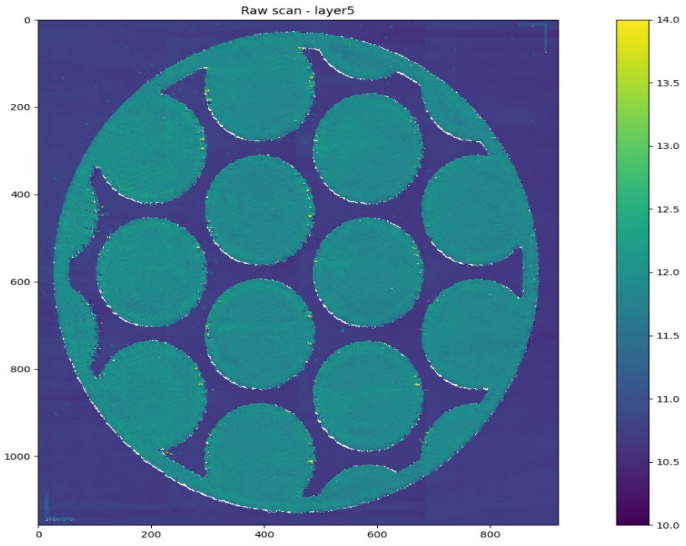

Figure G2. Layer 5.

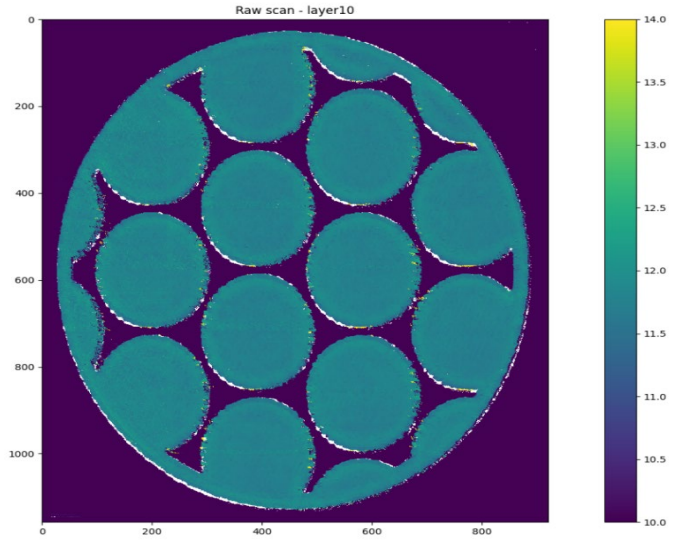

Figure G3. Layer 10.

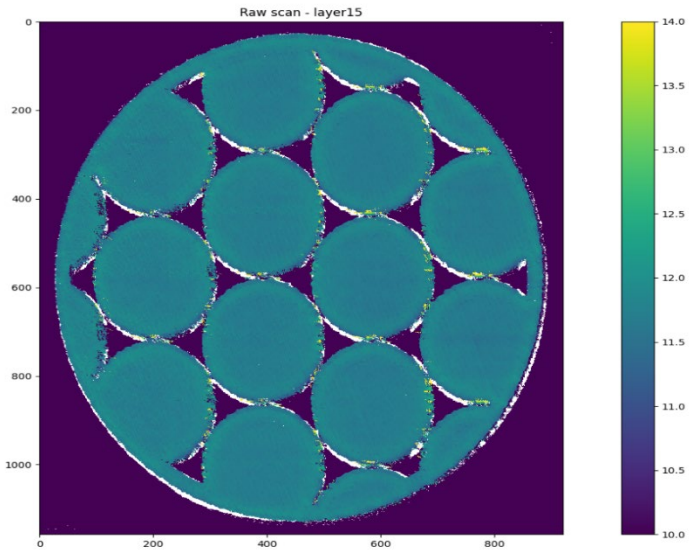

Figure G4. Layer 15.

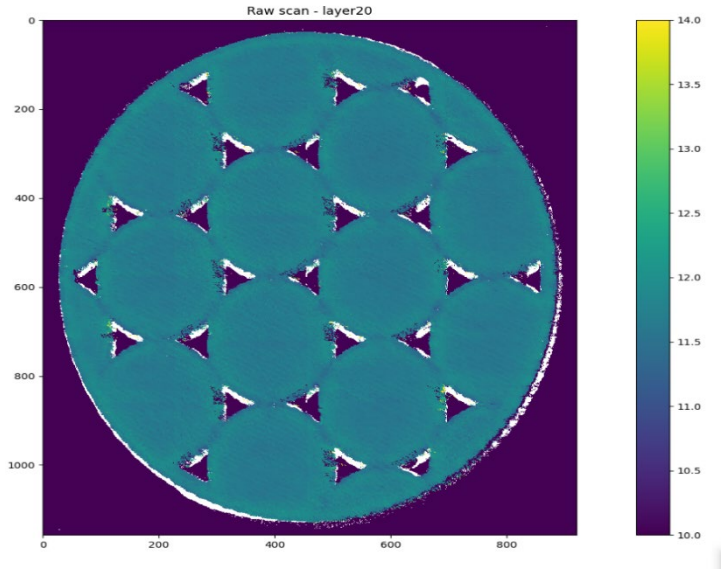

Figure G5. Layer 20.

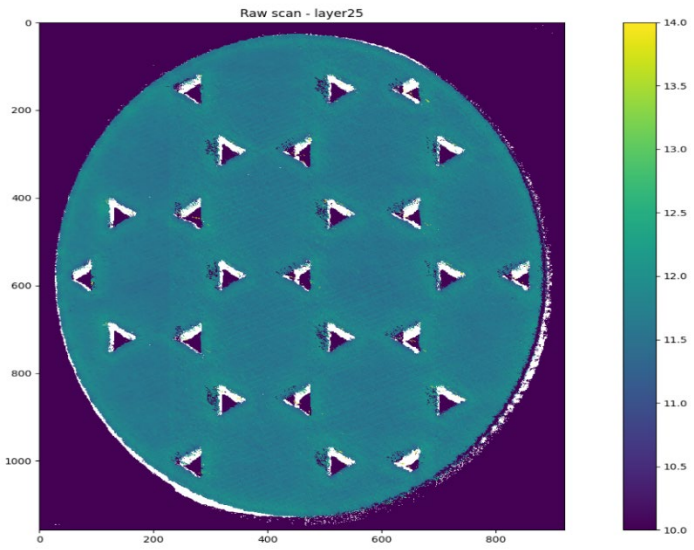

Figure G6. Layer 25.

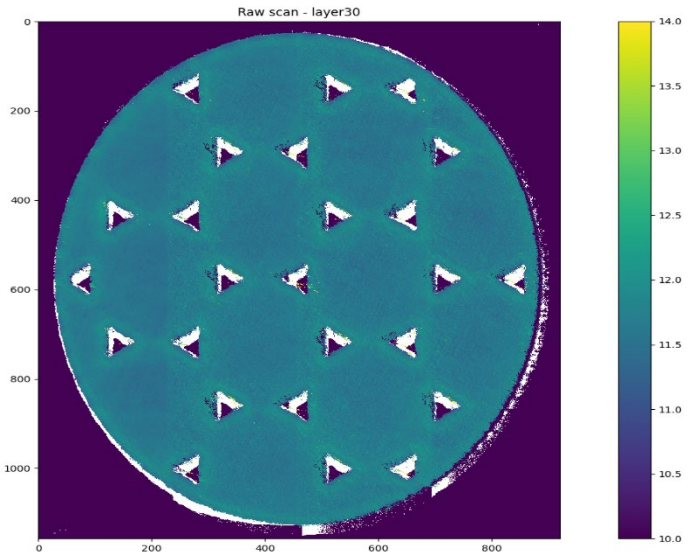

Figure G7. Layer 30.

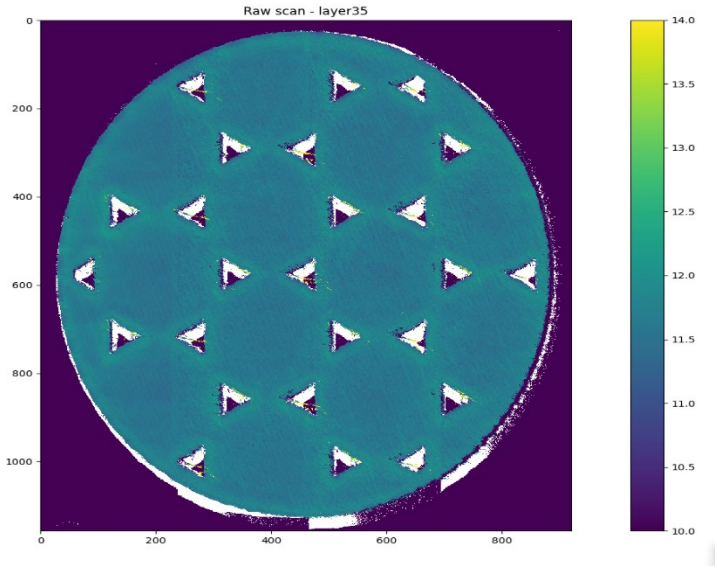

Figure G8. Layer 35.

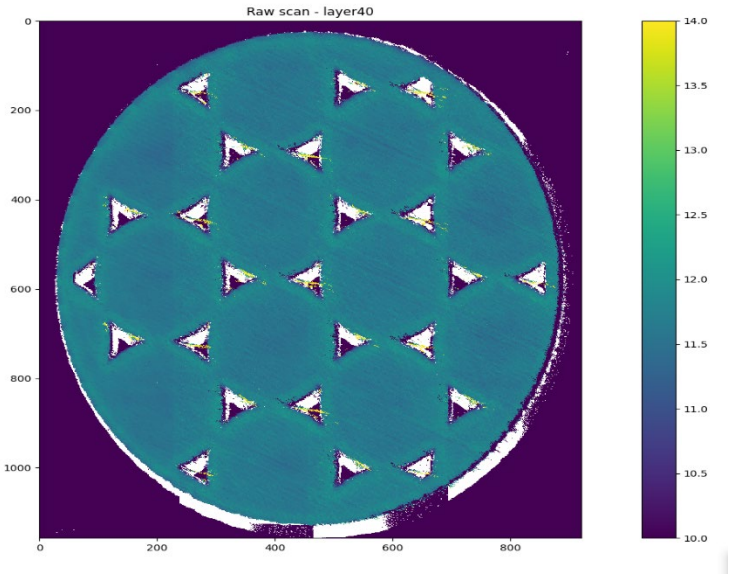

Figure G9. Layer 40.

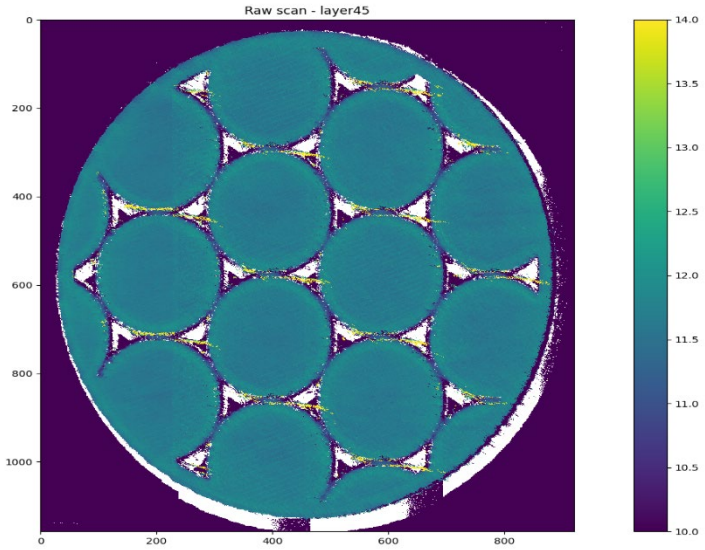

Figure G10. Layer 45.

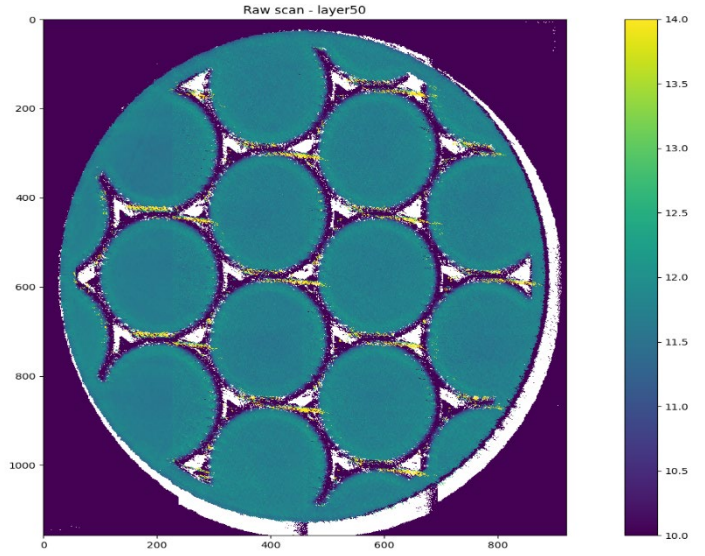

Figure G11. Layer 50.

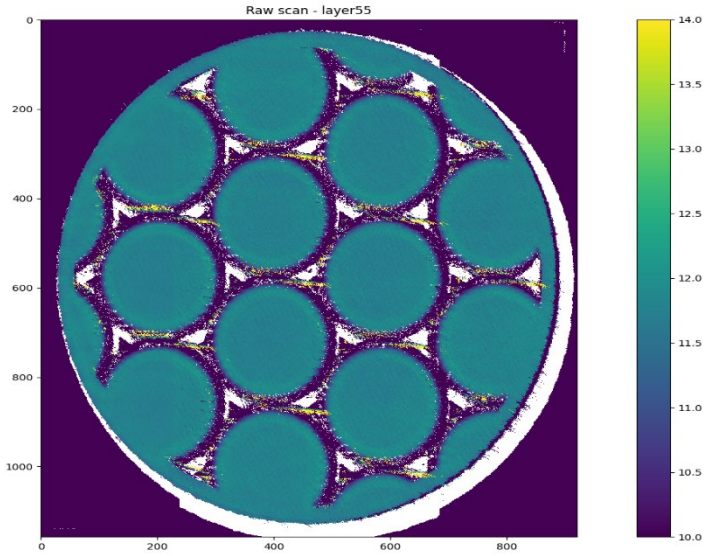

Figure G12. Layer 55.

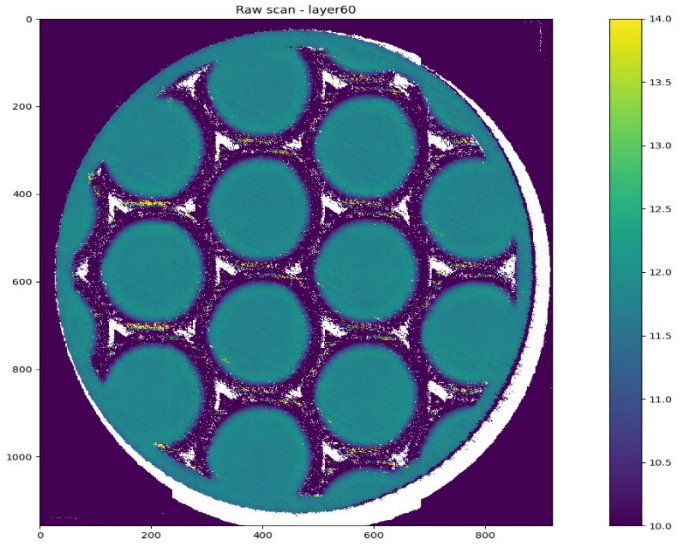

Figure G13. Layer 60.

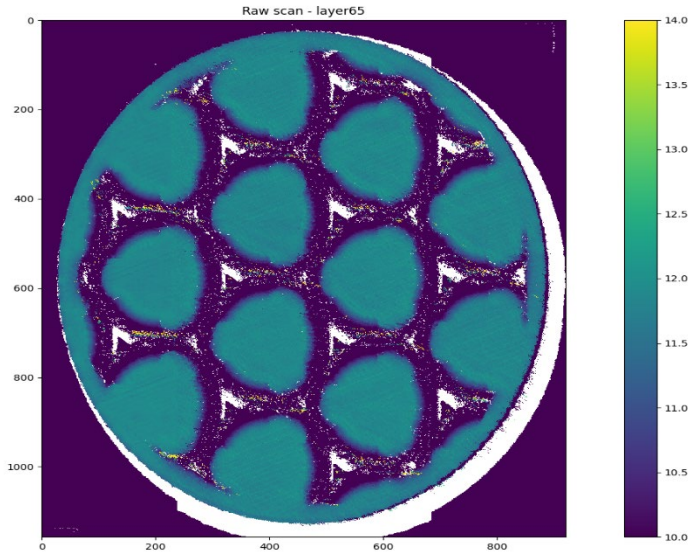

Figure G14. Layer 65.

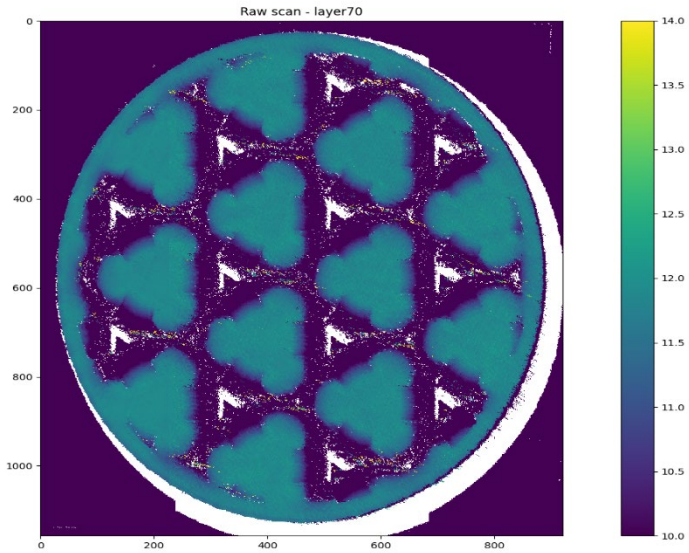

Figure G15. Layer 70.

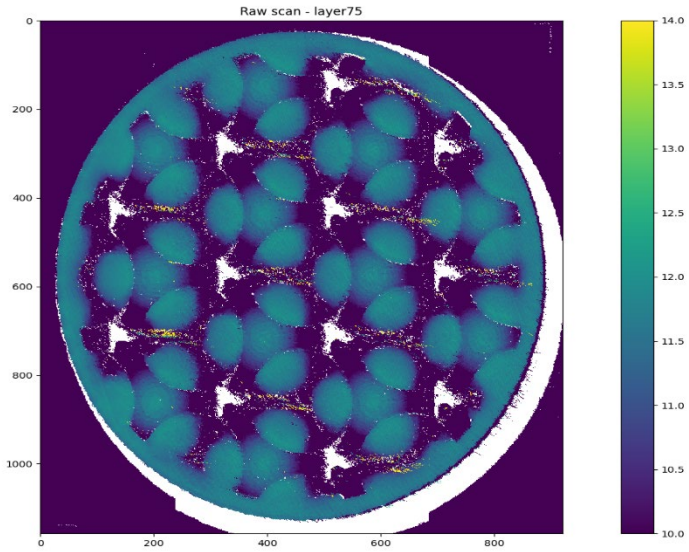

Figure G16. Layer 75.

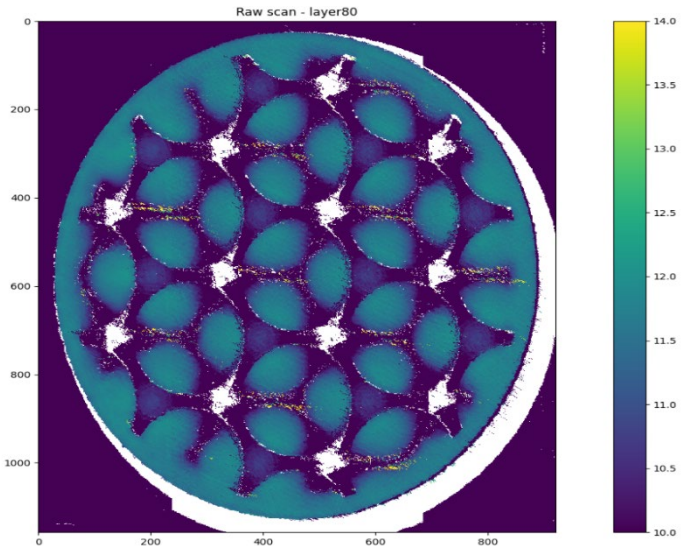

Figure G17. Layer 80.

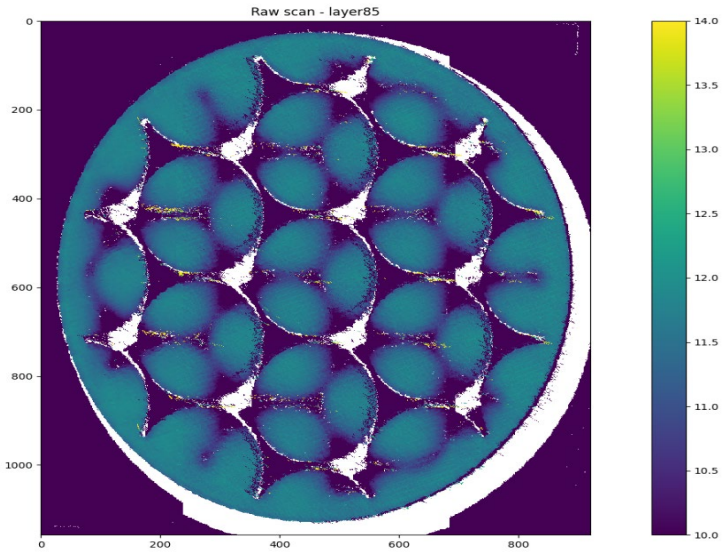

Figure G18. Layer 85.

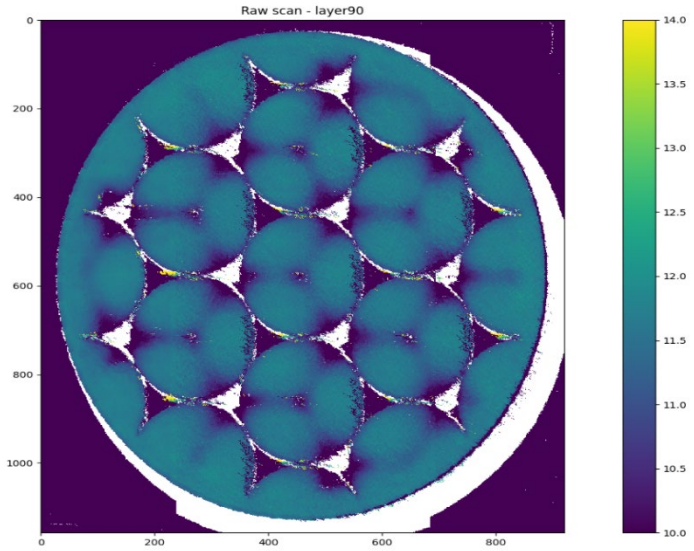

Figure G19. Layer 90.

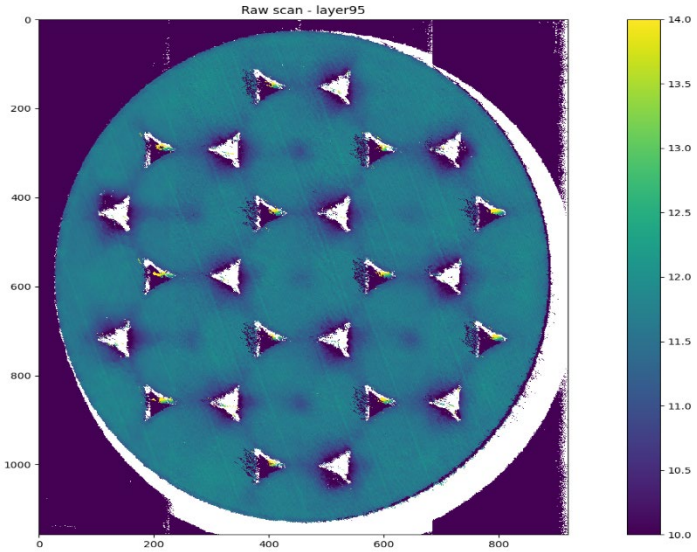

Figure G20. Layer 95.

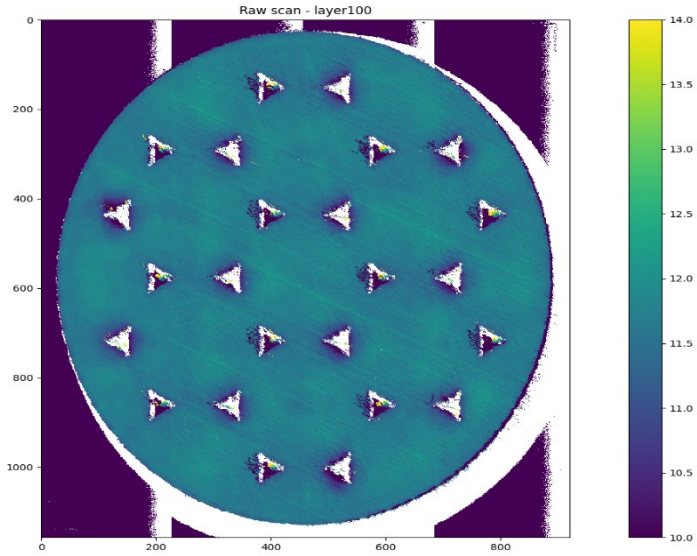

Figure G21. Layer 100.

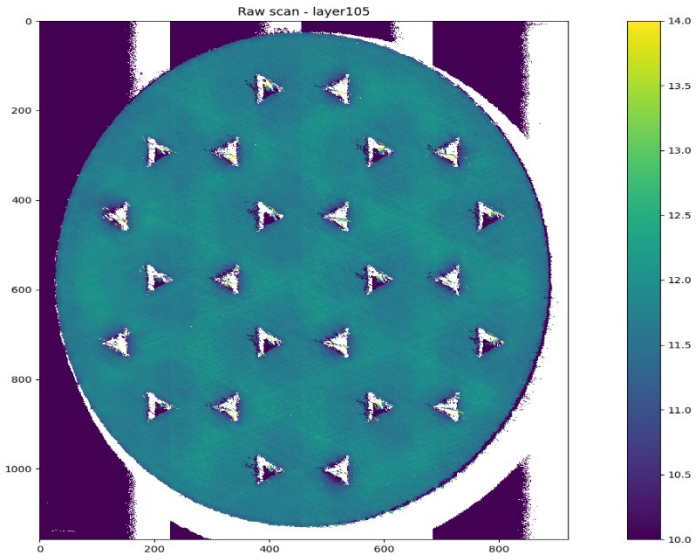

Figure G22. Layer 105.

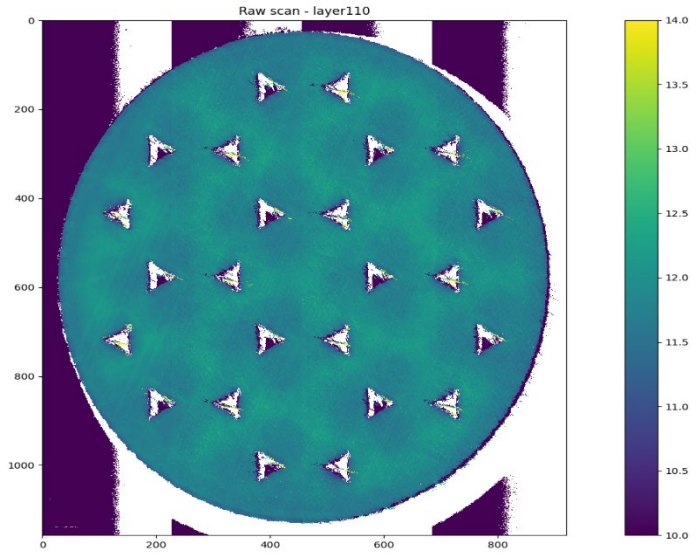

Figure G23. Layer 110.

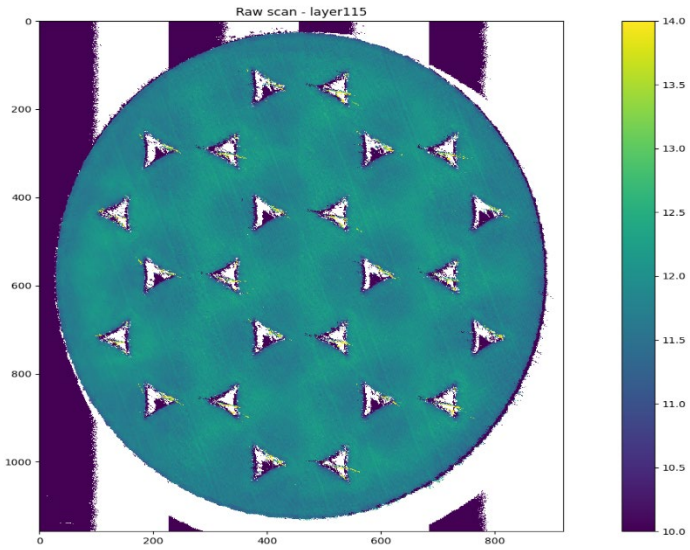

Figure G24. Layer 115.

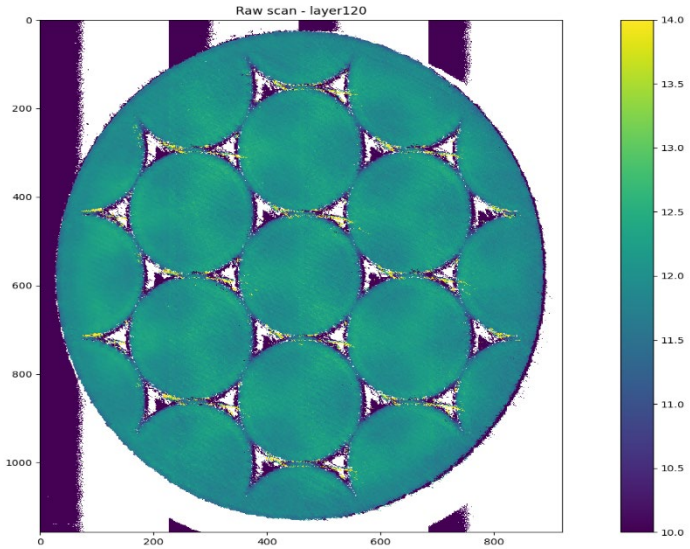

Figure G25. Layer 120.

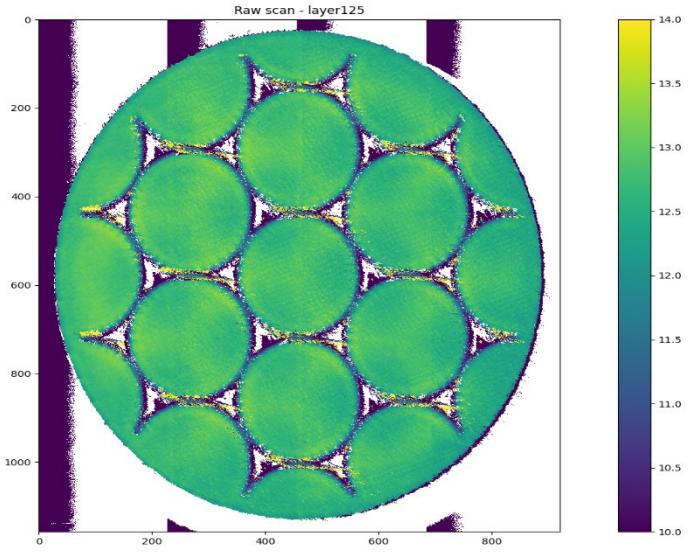

Figure G26. Layer 125

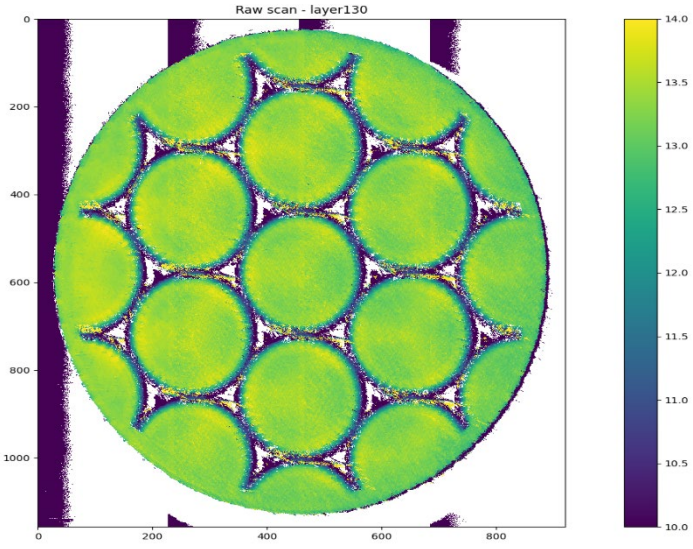

Figure G27. Layer 130.

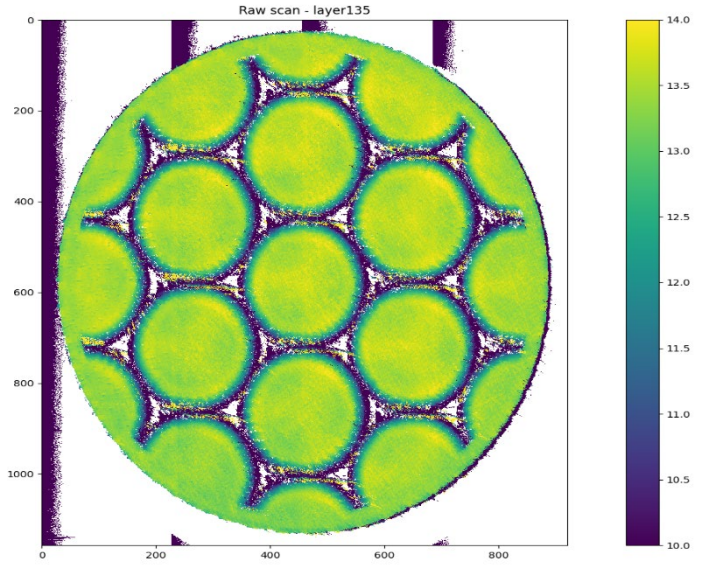

Figure G28. Layer 135

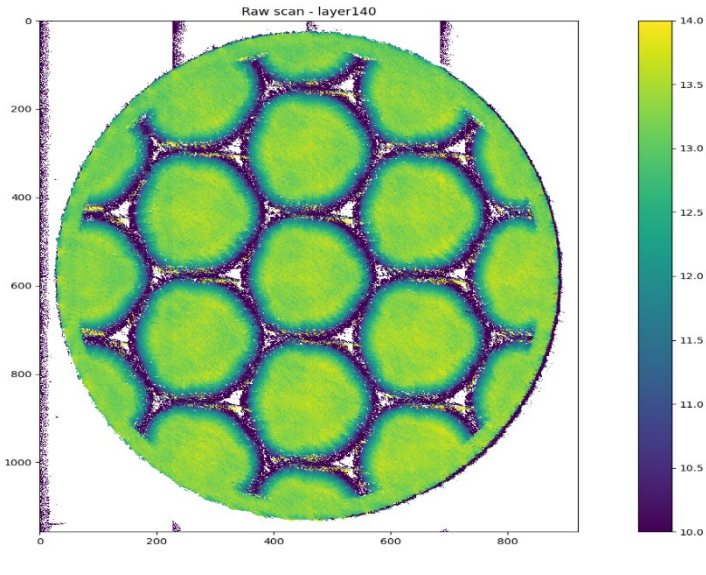

Figure G29. Layer 140.

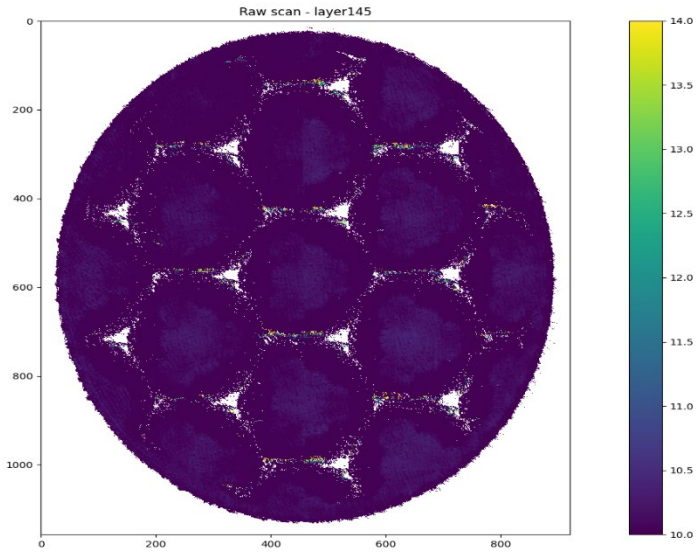

Figure G30. Layer 145.

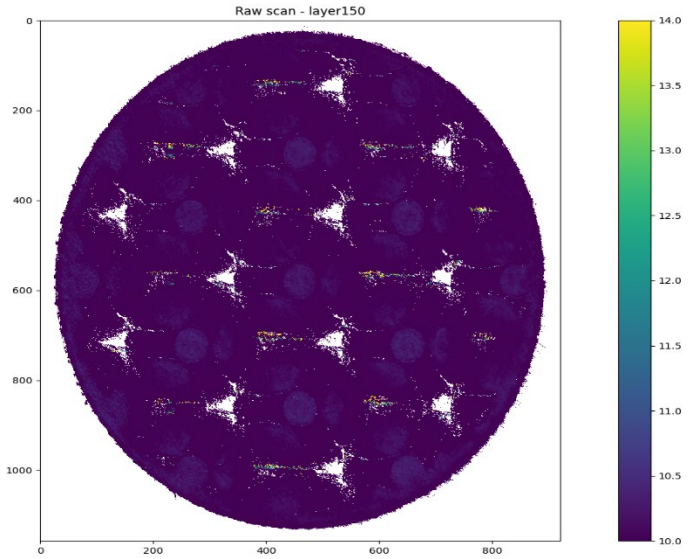

Figure G31. Layer 150.

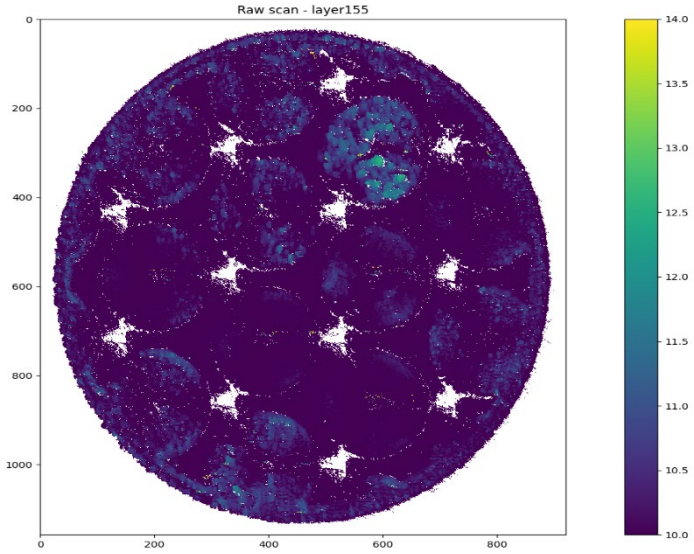

Figure G32. Layer 155.

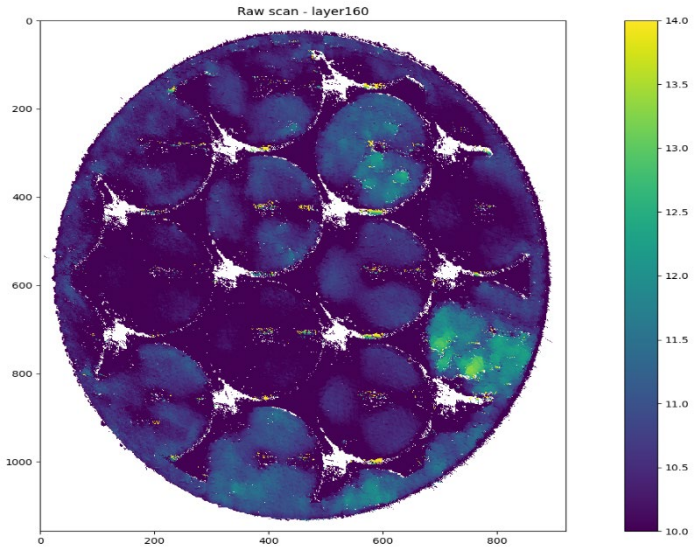

Figure G33. Layer 160

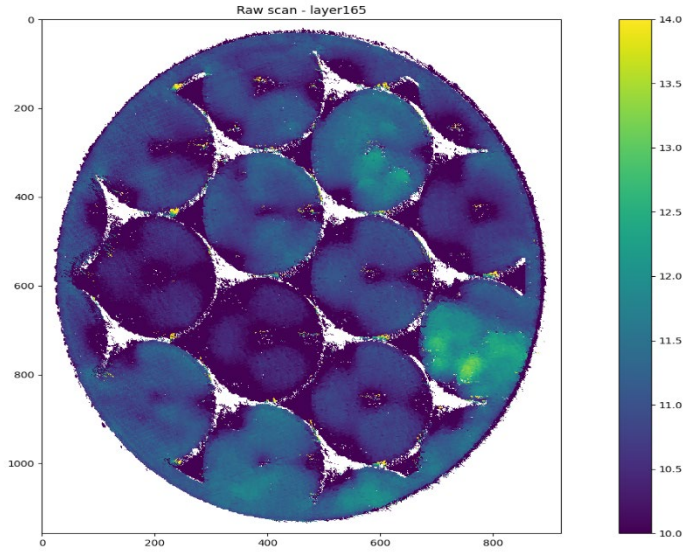

Figure G34. Layer 165.

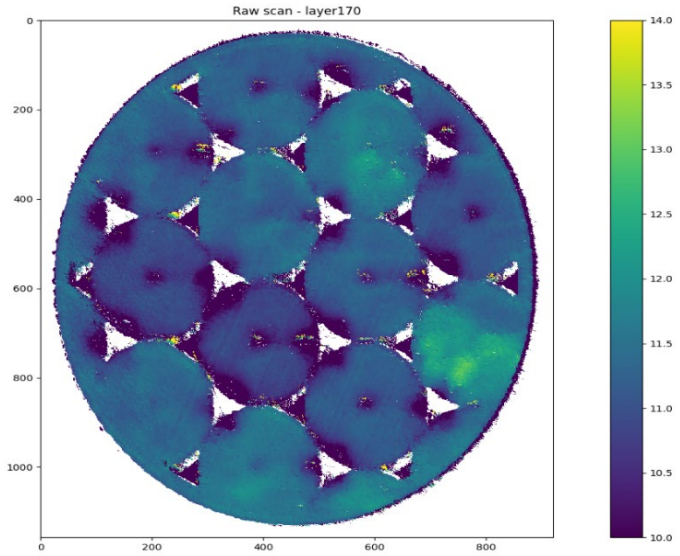

Figure G35. Layer 170.

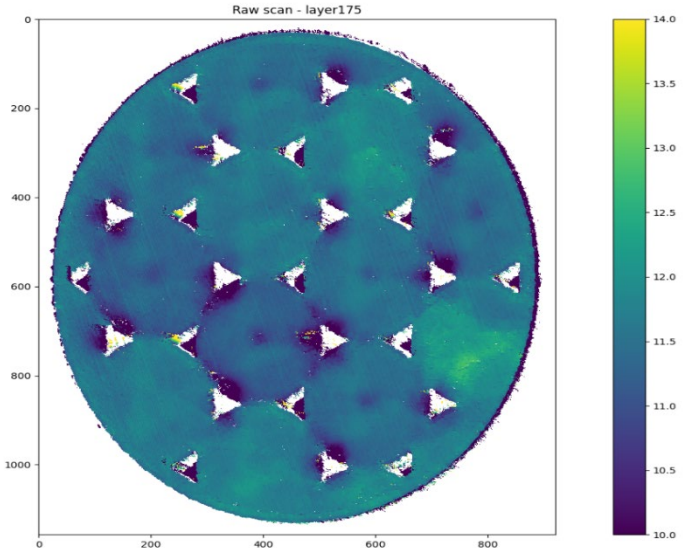

Figure G36. Layer 175.

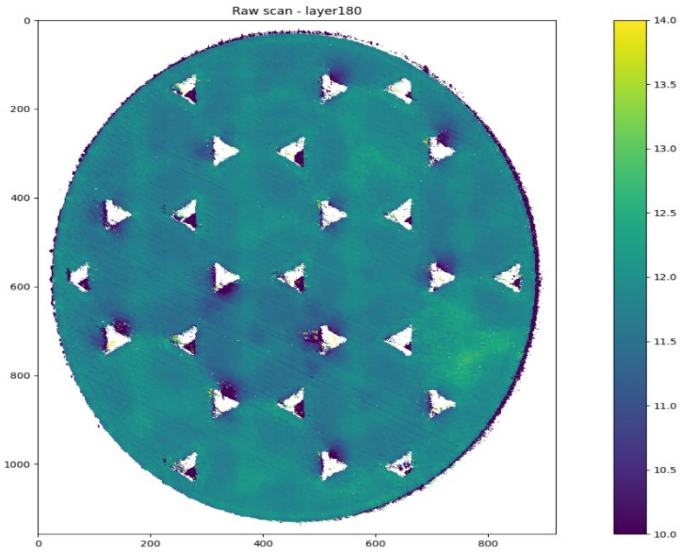

Figure G37. Layer 180.

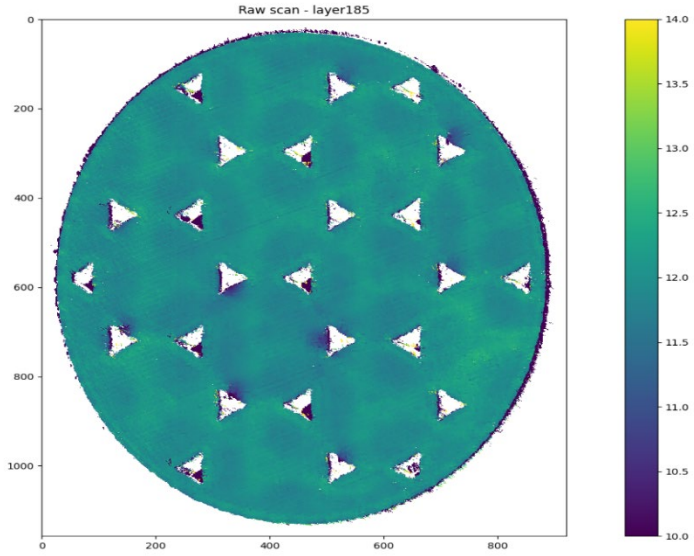

Figure G38. Layer 185.

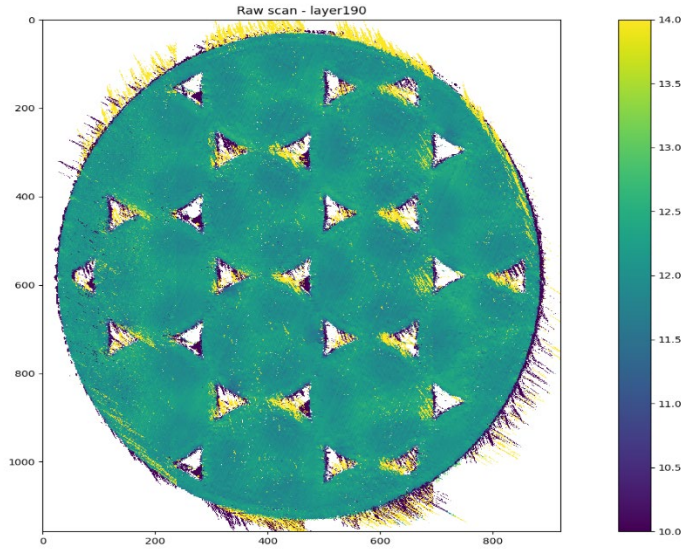

Figure G39. Layer 190.

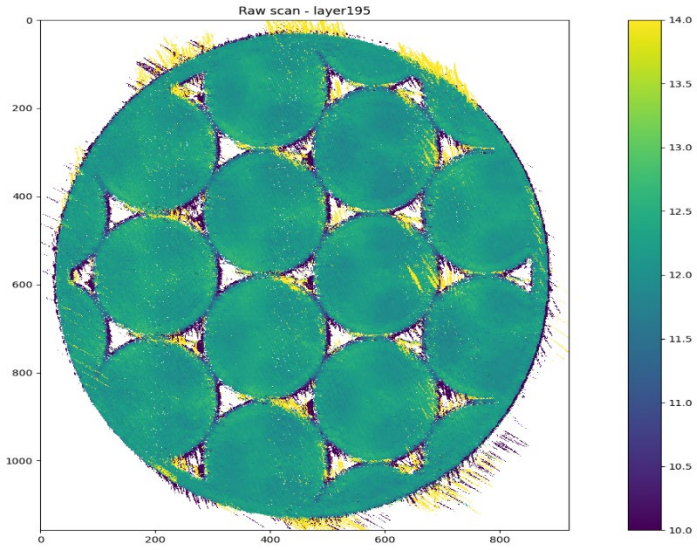

Figure G40. Layer 195.

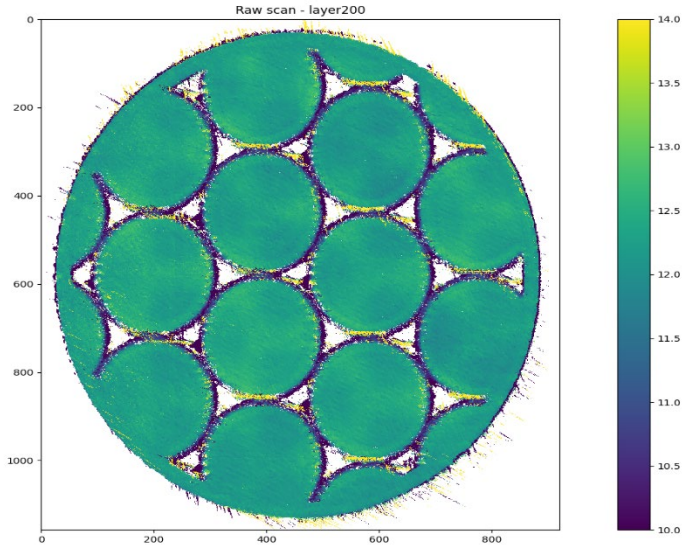

Figure G41. Layer 200.

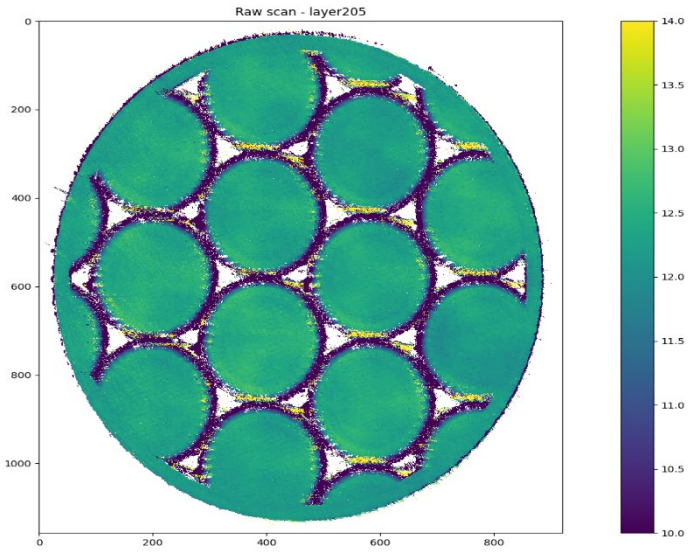

Figure G42. Layer 205.

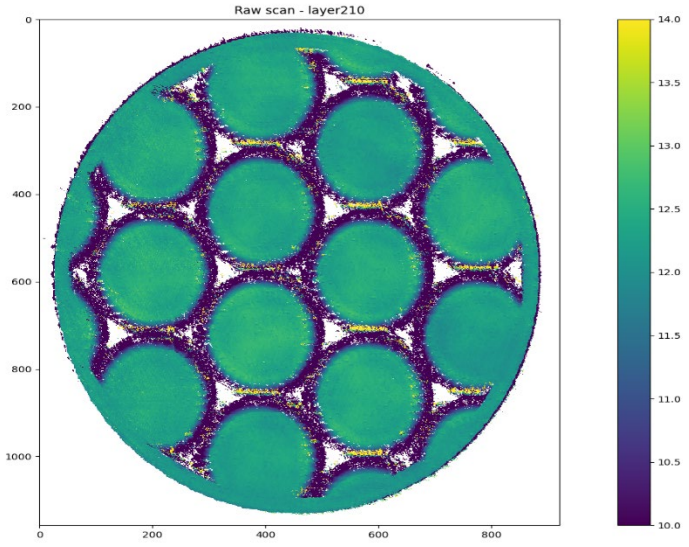

Figure G43. Layer 210.

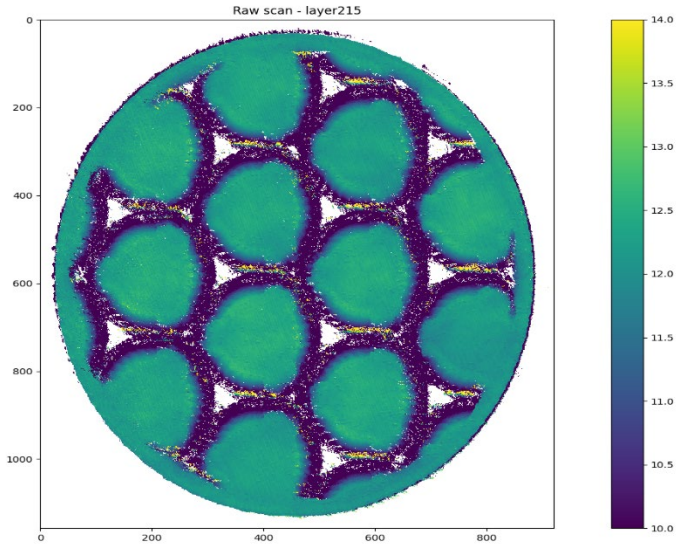

Figure G44. Layer 215.

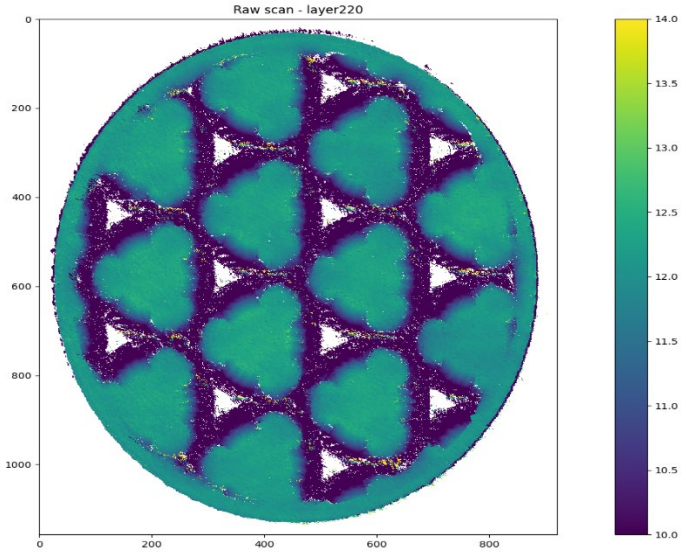

Figure G45. Layer 220.

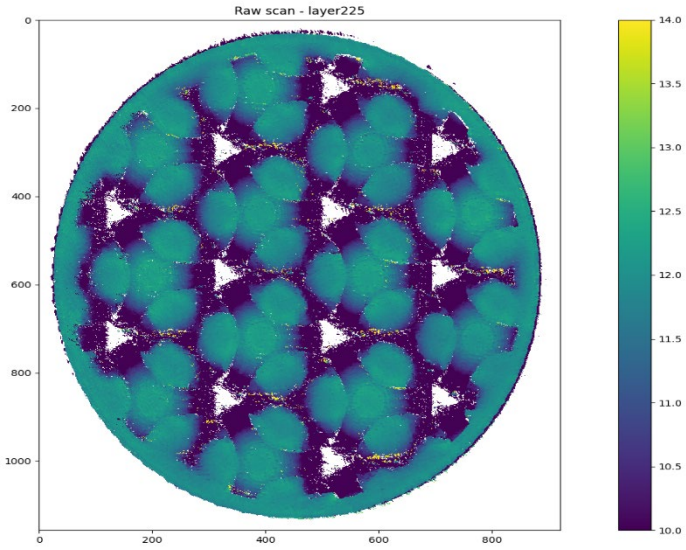

Figure G46. Layer 225.

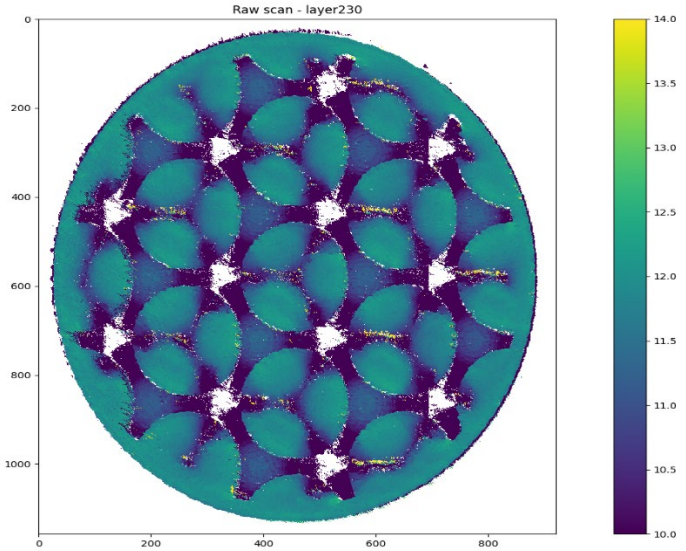

Figure G47. Layer 230.

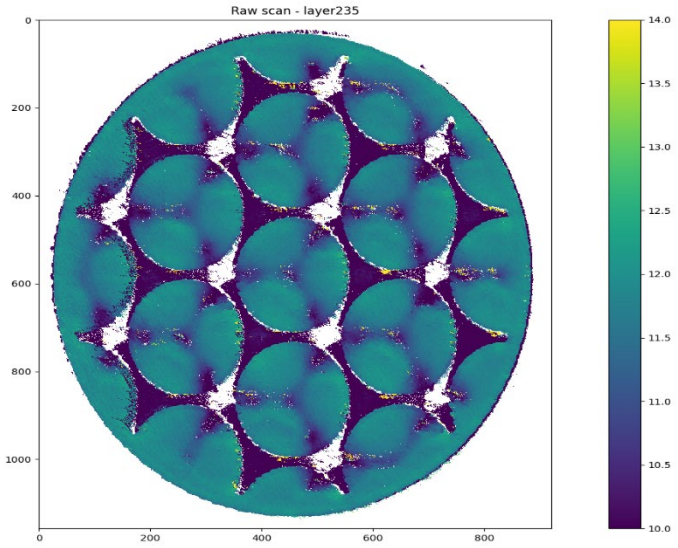

Figure G48. Layer 235.

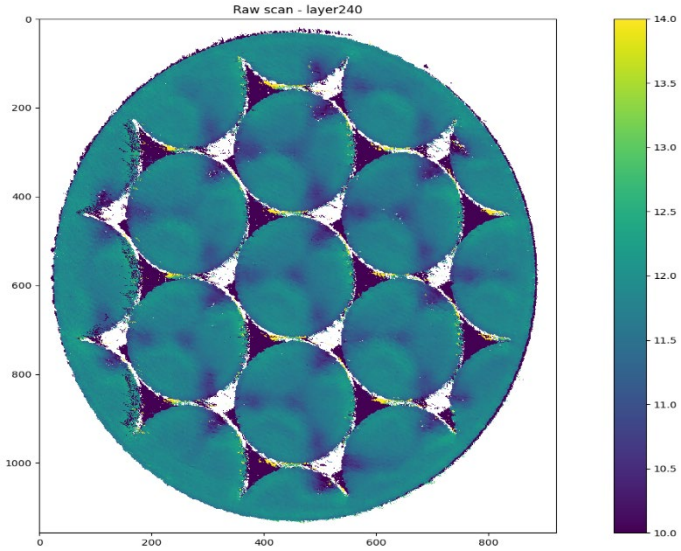

Figure G49. Layer 240.

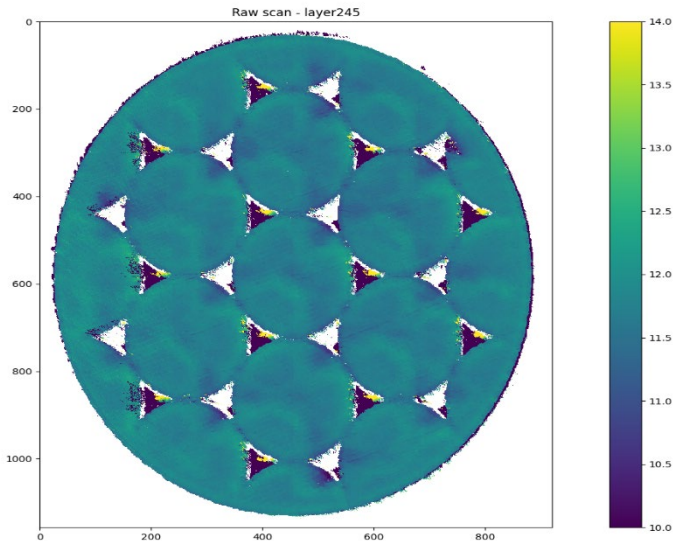

Figure G50. Layer 245.

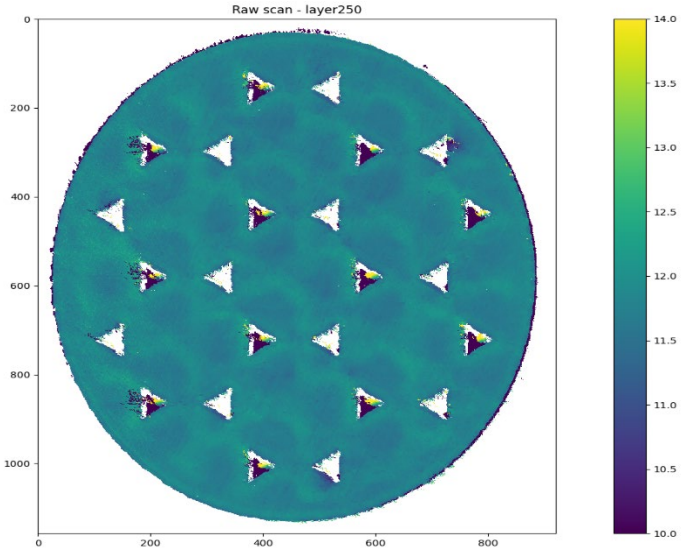

Figure G51. Layer 250.

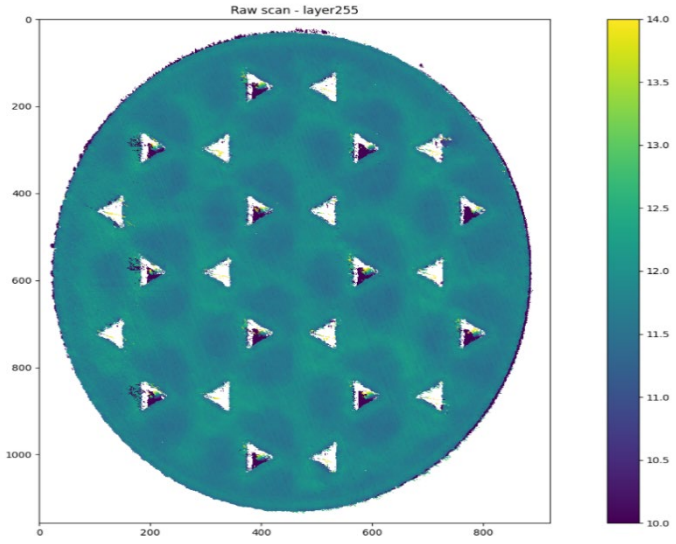

Figure G52. Layer 255.

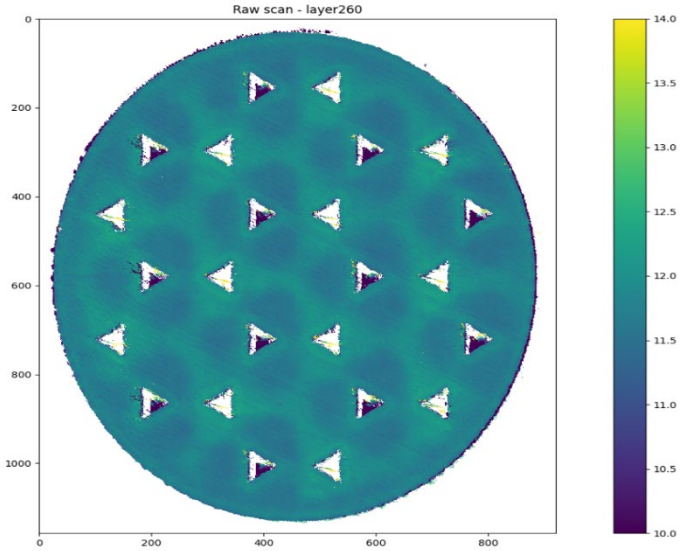

Figure G53. Layer 260.

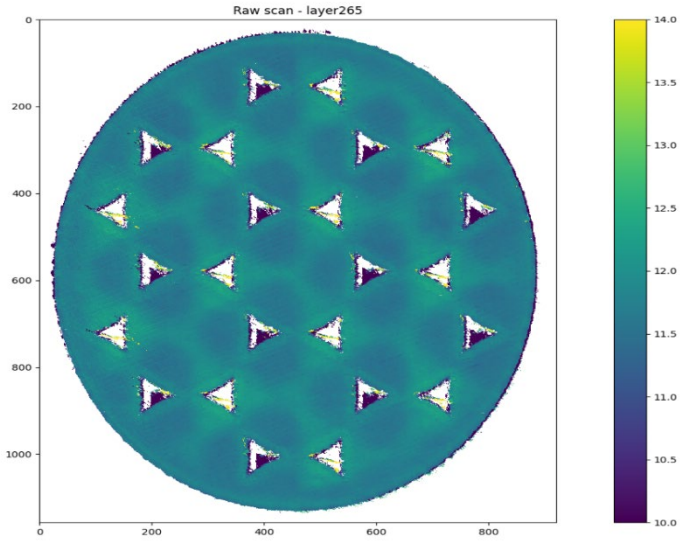

Figure G54. Layer 265.

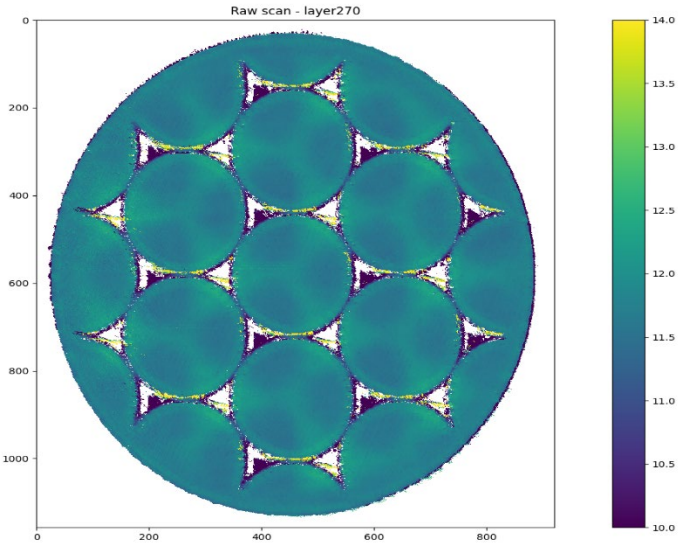

Figure G55. Layer 270.

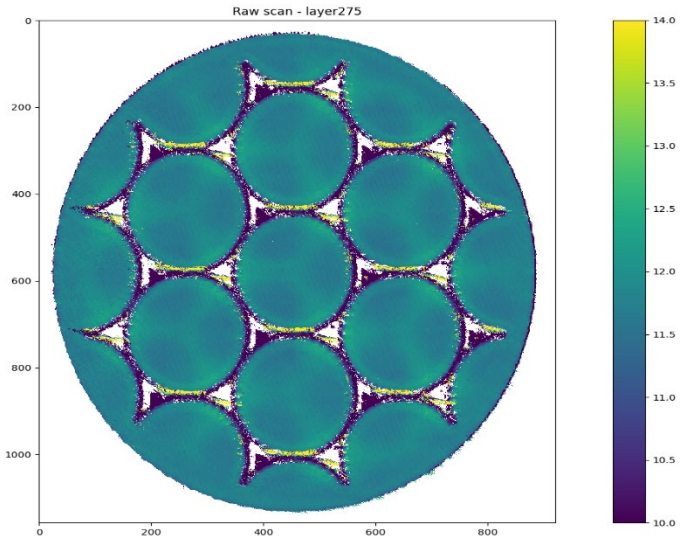

Figure G56. Layer 275.

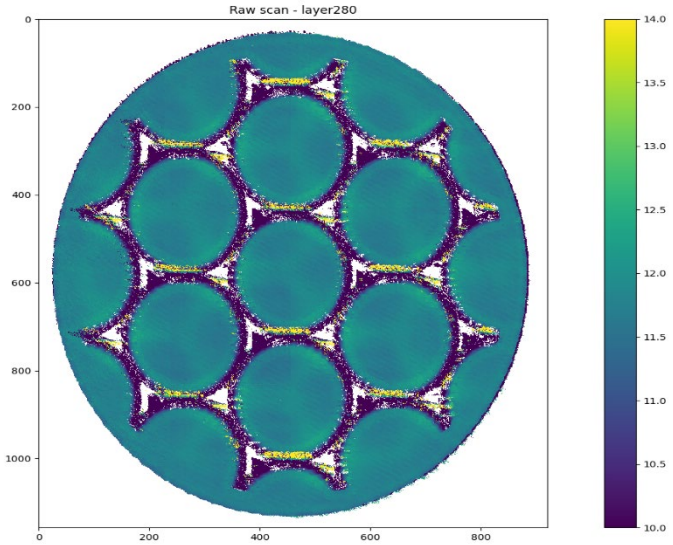

Figure G57. Layer 280.

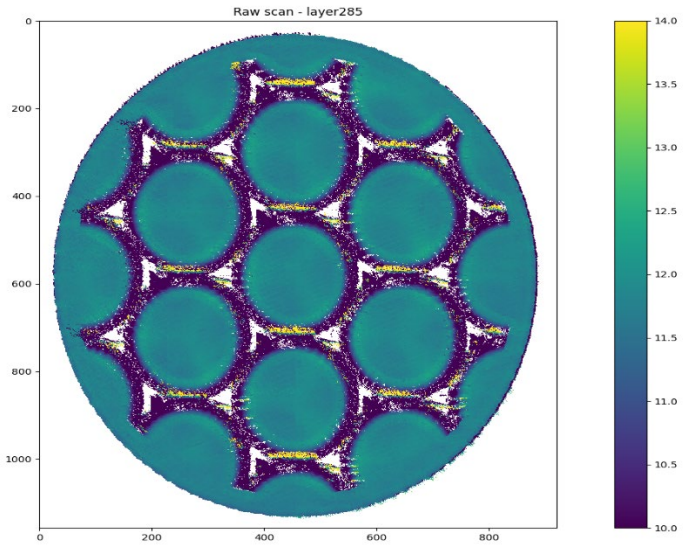

Figure G58. Layer 285.

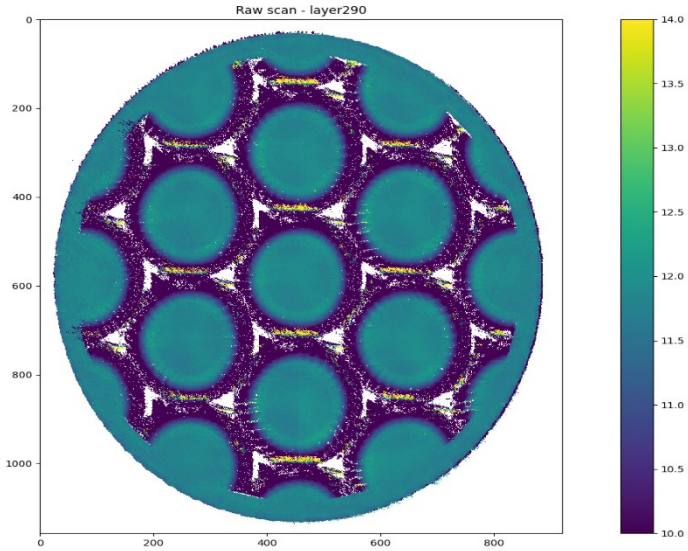

Figure G59. Layer 290.

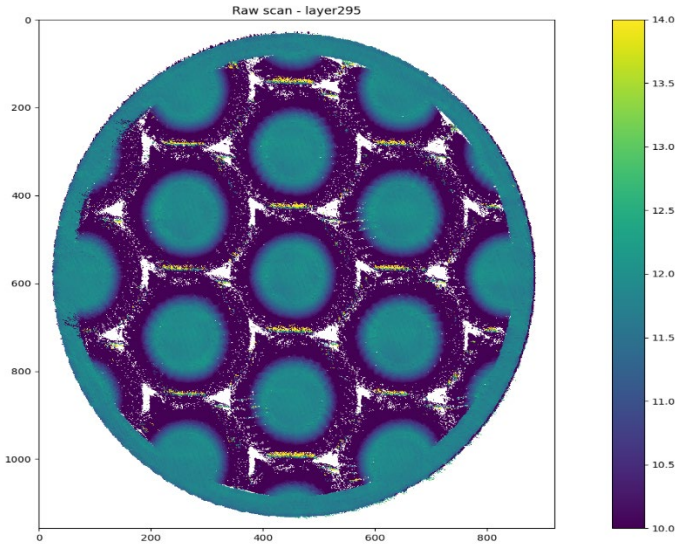

Figure G60. Layer 295.

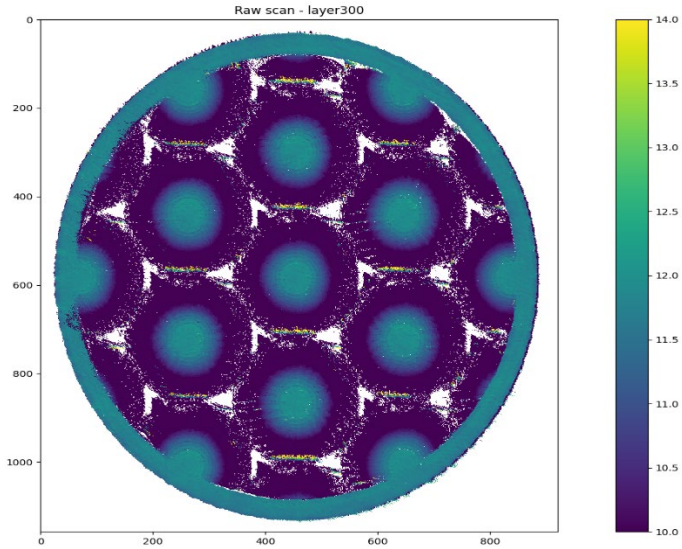

Figure G61. Layer 300.

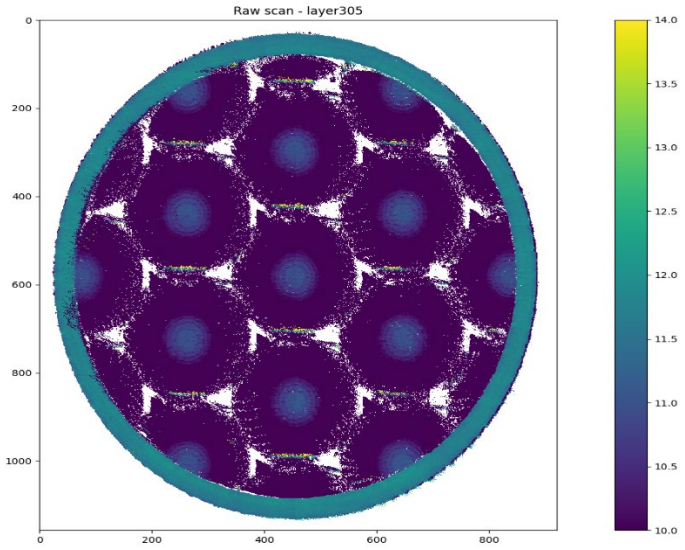

Figure G62. Layer 305.

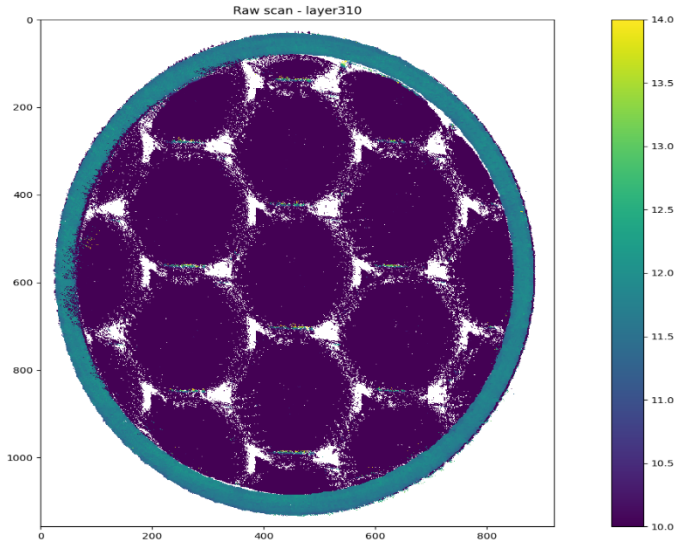

Figure G63. Layer 310.

APPENDIX H. MATLAB SCRIPT FOR IMAGE COMPILATION

This MATLAB script is designed to take a folder input containing pictures, located in Appendix G, and produce a 3-D representation.

```
dirname = 'layers0-150\'
myfiles = dir(dirname)

for iii = 190:350
   fname = [dirname 'layer' num2str(iii) '.png'];
   if exist(fname)==2
       A = imread(fname);
       B = rgb2hsv(A);

       figure(1);
       subplot(1,4,2);
       lowthresh = 250;
       highthresh = 400;
       As3 = sum(A,3); As3 = As3(63:879,77:715,:);
       As3(As3<lowthresh) = 0;
       As3(As3>highthresh) = 0;
       As3 = imgaussfilt(As3,8);
       As3(As3<lowthresh) = 0;
       As3(As3>highthresh) = 0;
       As3(As3~=0) = 1;
       contourf(As3,'linestyle','none');axis equal;colorbar;

       subplot(1,4,3);
       BW1 = edge(As3,'Canny');
       contourf(BW1,'linestyle','none');axis equal;colorbar;

       [xxx,yyy] = find(BW1~=0);
       yyy = 1.2836.*yyy - 423;
       xxx = xxx-423;
       rrr = sqrt(xxx.^2 + yyy.^2);
       ij = find(rrr>116);
       xxx(ij) = [];
       yyy(ij) = [];

       xxx = xxx*84/188;
       yyy = yyy*84/188;
       zzz = iii*0.24*2*ones(size(xxx));

       figure(9);
       hold all;
       plot3(zzz,xxx,yyy,'.k');
       axis normal;
       hold off;
       ylabel('width ~mm')
       zlabel('depth ~mm');


       drawnow
       pause(0.25);
   end
end
```

THIS PAGE INTENTIONALLY LEFT BLANK

APPENDIX I. VENTURI CALCULATIONS

These are the venturi calculations to determine the conditions necessary in the loop for proper function.

$\Delta P_{available} := 20\ psi$ $\rho := 1000\ \frac{kg}{m^3}$ $\mu := 1.0016 \cdot \frac{Pa \cdot s}{1000}$

$\Delta P_{low} := 0.1\ \Delta P_{available}$ $\Delta P_{high} := 0.9\ \Delta P_{available}$

$d_o := 4\ in$ $d_i := 1.0\ in$

$A_o := \frac{\pi}{4} \cdot d_o^{\,2}$ $A_i := \frac{\pi}{4} \cdot d_i^{\,2}$

$$Q_{low} := A_o \cdot \sqrt{\frac{2}{\rho} \cdot \frac{\Delta P_{low}}{\left(\frac{A_o}{A_i}\right)^2 - 1}} = 42.261\ gpm \qquad Re_{low} := \frac{\frac{Q_{low}}{A_o} \cdot d_o \cdot \rho}{\mu} = 3.336 \cdot 10^4$$

$$Q_{high} := A_o \cdot \sqrt{\frac{2}{\rho} \cdot \frac{\Delta P_{high}}{\left(\frac{A_o}{A_i}\right)^2 - 1}} = 126.782\ gpm \qquad Re_{hi} := \frac{\frac{Q_{high}}{A_o} \cdot d_o \cdot \rho}{\mu} = 1.001 \cdot 10^5$$

$\Delta P_{low} = 2\ psi$ $\Delta P_{high} = 18\ psi$

$Q_{low} = 42.261\ gpm$ $Q_{high} = 126.782\ gpm$

$Re_{low} = 3.336 \cdot 10^4$ $Re_{hi} = 1.001 \cdot 10^5$

THIS PAGE INTENTIONALLY LEFT BLANK

APPENDIX J. LOOP PRESSURE RATINGS

	A	B	C	D	E	F	G	H
1	**Component**	Size	Quantity	Pressure Rating (psi)	(kPa)	Notes		
2	PVC Pipe for water (Size 4)	10 ft	3	220	1516.85			
3	Female Size 4 Flange		14	220	1516.85			
4	Flow Throttle Valve		1	220	1516.85			
5	Isolation valve		2	220	1516.85			
6	Acrylic Tube (Size 4)	5ft	1	171.43	1181.96	Factor of Safety 10 Required		
7	Acrylic Sheet		1	Not Subject				
8	Acrylic Sheet # 2		1	Not Subject				
9	45* Females		8	220	1516.85			
10	Pressure Relief Valve		1	300	2068.43			
11	Male to Female Connectors		2	220	1516.85			
12	Wall fitting female to female		4	220	1516.85			
13	PVC Pipe for water (Size 2)	5ft	2	280	1930.53			
14	Male to Female 1 1/2" to 1 1/4 "		1	220	1516.85			
15	PVC Pipe (Size 1 1/2)	5ft	1	330	2275.27			
16	3 Size 4 Tee adapter		3	220	1516.85			
17								
18	Outlet/Inlet Isolations		2	150	1034.21			
19								
20								
21								
22								
23								
24								
25								
26								
27								
28								
29								

THIS PAGE INTENTIONALLY LEFT BLANK

APPENDIX K. CFD NUMERIC RESULTS

These are the overall mesh sizes and results of the computational models compared with their analytical counterparts.

Packed Bed	Mesh Size (mm)	Nodes	Elements	Inflation Layers	Y+	Expected C_v	C_v Results	Error
Unit Cell	0.5	600,574	1,667,922	8.0 E-7 m	<5	10.24	12.2	19.10%
Whole Body	1	18,500,000	44,000,000	8.0 E-7 m	< 30	14.91	10.12	28.80%
Helical	Model							
	Mesh Size (mm)	Nodes	Elements	Inflation layers	Y+	Expected C_v	C_v Results	Error
Nodes	1	8,500,000	20,000,000	8.0 E-7 m	<30	8.66	10.12	6.20%

THIS PAGE INTENTIONALLY LEFT BLANK

APPENDIX L. PRODUCTION DIMENSIONS AND BUILD TIMES

These are the final dimensions of the models and their respective times for production.

Model	Packed Bed 1st Print (Elem-X)	Packed Bed 2nd Print (Elem-X)	Helical (Ultimaker 3)
Length (cm)	6.42	7.32	12.95
Diameter (cm)	3.325	3.325	3.325
Mass (kg)	0.772	0.872	0.897
Volume (cm^3)	281.86	324.96	334.13
Print Time	<12 hr	<12 hr	5 days 13 hours

THIS PAGE INTENTIONALLY LEFT BLANK

LIST OF REFERENCES

[1] Frazier, William E. 2014. “Metal Additive Manufacturing: A Review.” *Journal of Materials Engineering and Performance,* 23 (6): 1917–28. https://doi.org/10.1007/s11665-014-0958-z.

[2] Schmelzle, John, Eric V. Kline, Corey J. Dickman, Edward W. Reutzel, Griffin Jones, and Timothy W. Simpson. 2015. “(Re)Designing for Part Consolidation: Understanding the Challenges of Metal Additive Manufacturing.” Journal of Mechanical Design 137 (111404). https://doi.org/10.1115/1.4031156.

[3] Volk, Michael. 2013. *Pump Characteristics and Applications.* Boca Raton: CRC Press. https://doi.org/10.1201/b15559.

[4] Walski, Thomas, Wayne Hartell, and Zheng Wu. 2010. “Developing System Head Curves for Closed Systems.” *Journal (American Water Works Association),* 102 (9): 84–89.

[5] Motaman, S. Amir H., Fabian Kies, Patrick Kohnen, Maike Letang, Mingxuan Lin, Andrey Molotnikov, and Christian Haase. 2020. “Optimal Design for Metal Additive Manufacturing: An Integrated Computational Materials Engineering (ICME) Approach.” *JOM*, 72 (3): 1092–1104. http://dx.doi.org/10.1007/s11837-020-04028-4..

[6] Smith, Walter C., and Richard Dean 2013. “Structural Characteristics of Fused Deposition Modeling Polycarbonate Material.” *Polymer Testing*. 32 (8): 1306–12. https://doi.org/10.1016/j.polymertesting.2013.07.014.

[7] Rupal, Baltej Singh, Nabil Anwer, Marc Secanell, and Ahmed Jawad Qureshi. 2020. “Geometric Tolerance and Manufacturing Assemblability Estimation of Metal Additive Manufacturing (AM) Processes.” *Materials & Design*, 194 (September): 108842. https://doi.org/10.1016/j.matdes.2020.108842.

[8] Karode, Sandeep K, and Ashwani Kumar. 2001. “Flow Visualization through Spacer Filled Channels by Computational Fluid Dynamics I.: Pressure Drop and Shear Rate Calculations for Flat Sheet Geometry.” *Journal of Membrane Science,* 193 (1): 69–84. https://doi.org/10.1016/S0376-7388(01)00494-X.

[9] Casey, William Emerson. n.d. “Thermal-Hydraulic Transient Analysis of a Packed Particle Bed Reactor Fuel Element,” master’s thesis, MIT, 305.

[10] Hudson, Douglas Rennie. 1949. “Density and Packing in an Aggregate of Mixed Spheres.” *Journal of Applied Physics,* 20 (2): 154–62. https://doi.org/10.1063/1.1698327.

[11] Susskind, Herbert, and Walter Becker. 1967. “Pressure Drop in Geometrically Ordered Packed Beds of Spheres.” *AIChE Journal*, 13 (6): 1155–59. https://doi.org/10.1002/aic.690130622.

[12] Idel'chik, I.E., Ed., 1966, *Handbook of Hydraulic Resistance*, National Technical Information Service, Springfield, VA.

[13] "Additive Manufacturing Innovation with 3D Printing - Xerox." n.d. Accessed June 8, 2021. https://www.xerox.com/en-us/innovation/insights/additive-manufacturing-3d-printing.

[14] Islam, M S, Avizit Basak, M A R Sarkar, and M Q Islam. 2016. "Study of Minor Loss Coefficient of Flexible Pipes for Different Bend Angles and Different Bend Radius by Experiment and Simulation," 7.

[15] Liu, Shijie, Artin Afacan, Hisham Nasr-El-Din, and Jacob Masliyah. 1994. "An Experimental Study of Pressure Drop in Helical Pipes." *Proceedings of The Royal Society A: Mathematical, Physical and Engineering Sciences* 444 (February): 307–16. https://doi.org/10.1098/rspa.1994.0020.

[16] "Ultimaker 3 PDF Manuals." n.d. Ultimaker Support. Accessed May 7, 2021. https://support.ultimaker.com/hc/en-us/articles/360013053880-Ultimaker-3-PDF-manuals.

[17] "Mcmaster-Carr Circulation Pump for Water and Oil, 120/208-240V AC, 3/4 hp." n.d. Accessed May 5, 2021 https://www.mcmaster.com/8249K82/?session=uLN4hMtXkOcPalNirjkrkcV08A.

[18] "FRENIC-Mini (C2)." n.d. Fuji Electric Corp. of America (blog). Accessed May 7, 2021. https://americas.fujielectric.com/products/vfd-inverters-ac-drives/frenic-mini-c2/.

[19] "Pipe Flow Measurement - Venturi Flowmeters - Bernoulli's Equation." n.d. Accessed May 5, 2021. http://www.wermac.org/specials/venturiflowmeter.html.

[20] Smith, Walter C., 2021, Research Associate Professor at The Naval Postgraduate School, Monterey, CA. Private Communication.

[21] "CDAQ-9181." n.d. Accessed May 21, 2021. https://www.ni.com/en-us/support/model.cdaq-9181.html.

[22] "Wet/Wet Differential Pressure Transmitters for Industrial Media." n.d. Accessed May 21, 2021. https://www.omega.com/en-us/pressure-measurement/pressure-transducers/p/PX273.

[23] Ahmad, T, S L Plee, and J P Myers. "Fluent User's Guide," 2019, 2692.

[24] Adrian, Ronald J. "Particle-Imaging Techniques for Experimental Fluid Mechanics." *Annual Review of Fluid Mechanics* 23, no. 1 (1991): 261–304. https://doi.org/10.1146/annurev.fl.23.010191.001401.

INITIAL DISTRIBUTION LIST

1. Defense Technical Information Center
   Ft. Belvoir, Virginia

2. Dudley Knox Library
   Naval Postgraduate School
   Monterey, California